EXPERIMENTAL STUDY OF PRESSURE AND HEATING RATE ON A SWEPT CYLINDRICAL LEADING EDGE RESULTING FROM SWEPT SHOCK WAVE INTERFERENCE

by

Christopher E. Glass
B. S. May 1983, Old Dominion University

A Thesis Submitted to the Faculty of
Old Dominion University in Partial Fulfillment of the
Requirements for the Degree of

MASTER OF SCIENCE
MECHANICAL ENGINEERING

OLD DOMINION UNIVERSITY
April 1989

Approved by:

Robert L. Ash

Dr. Robert L. Ash (Director)

Oktay Baysal

Dr. Oktay Baysal

Sushil K. Chaturvedi

Dr. Sushil K. Chaturvedi

ABSTRACT

EXPERIMENTAL STUDY OF PRESSURE AND HEATING RATE ON A SWEPT CYLINDRICAL LEADING EDGE RESULTING FROM SWEPT SHOCK WAVE INTERFERENCE

Christopher E. Glass
Old Dominion University
Director: Dr. Robert L. Ash

An experimental study of the effects of leading edge sweep on surface pressure and heat transfer rate for swept shock wave interference is presented. This study was conducted as a cooperative agreement between NASA Langley Research Center and Calspan-University of Buffalo Research Center. Experimental tests were conducted in the Calspan 48-inch Hypersonic Shock Tunnel at a nominal Mach number of 8, nominal unit Reynolds number of 1.5×10^6 per foot, leading edge and incident shock generator sweep angles of 0°, 15°, and 30°, and incident shock generator angle-of-attack fixed at 12.5°. Detailed surface pressure and heat transfer rate on the cylindrical leading edge of a swept shock wave interference model were measured at the region of the maximum surface pressure and heat transfer rate.

The experimental study has shown that pressure and heat transfer rate on the cylindrical leading edge of the shock wave interference model were reduced as the sweep was increased over the range of tested parameters.

Peak surface pressure and heat transfer rate on the cylinder were about 10 and 30 times the undisturbed flow stagnation point value, respectively, for the 0° sweep test. A comparison of the 15° and 30° swept results with the 0° swept results showed that peak pressure was reduced about 13 percent and 44 percent, respectively, and peak heat transfer rate was reduced about 7 percent and 27 percent, respectively.

DEDICATION

This thesis is dedicated to my wife. May her academic career be as rich and rewarding as I have found mine.

ACKNOWLEDGMENTS

As with all experimental studies, production of a meaningful experiment with lasting results is not a singular effort but a group effort. To acknowledge all participants would be prohibitive, but I would like to acknowledge the key principals.

I appreciate the guidance of Dr. Robert L. Ash, who served as the chairman of my Thesis Advisory Committee, for his many useful suggestions during the preparation of this thesis. Thanks also to Dr. Oktay Baysal and Dr. Sushil Chaturvedi for serving on my graduate committee.

I thank Dr. Charles E. Treanor, Vice President of Calspan Corporation and Director of Calspan-UB Research Center, for contractual oversight which allowed the use of the Calspan facilities. I appreciate the guidance and useful suggestions of Dr. Michael S. Holden of Calspan Corporation during the testing phase of this study. The efforts of the Calspan technical staff, especially those of Mr. Viking Todd, are greatly appreciated. I am grateful to Dr. Allan R. Wieting and Mr. L. Roane Hunt of NASA Langley Research Center for their guidance with this research program. Also, thanks to Laura L. Eure for handling my travel orders to Buffalo, New York during the four months of tunnel tests.

This research was performed as a member of the Aerothermal Loads Branch, Structural Mechanics Division at NASA Langley Research Center. I must thank them for their generous graduate studies program and financial support.

TABLE OF CONTENTS

LIST OF TABLES

LIST OF FIGURES

LIST OF SYMBOLS

c_p	specific heat at a constant pressure, Btu/lb_m-°R
H	enthalpy, ft^2/sec^2
k	thermal conductivity, Btu/ft-sec-°R
L	length, inches
M	Mach number
p	pressure, psia
q	heat transfer rate, Btu/ft^2-sec
R	radius, inches
Re	unit Reynolds number, 1/ft
t	thickness, inches
T	temperature, °R
u	velocity, ft/sec
U	freestream velocity, ft/sec
X,Y	cylinder position with respect to the shock generator trailing edge
x,y,z	cartesian coordinates of the reference plane (See Fig. 12.)
Y_{inv}	vertical distance between the cylinder centerline and the calculated incident shock wave, inches
w	width, inches
1,2,3,...	flow region (See Figs. 2-7.)
α	angle-of-attack with respect to the freestream direction, deg
ε	small turning angle of the wedge flow from sweep, deg

λ	characteristic velocity, ft/sec (See equation (7).)
Λ	sweep angle, deg
θ	flow deflection angle, deg
Θ	circumferential position on the instrumented cylinder, deg
μ	angle of local wedge Mach number characteristic line, deg; also absolute viscosity, lb_f-sec/ft^2
ρ	density, lb_m/ft^3

SUBSCRIPTS

aw	adiabatic wall
bj	equivalent jet body
cw	cold wall
hw	hot wall
j	supersonic jet
o	stagnation line value
p	peak value
s	bow shock standoff distance
s-bj	equivalent jet body bow shock wave
sl	shear layer
t	shear layer transition
T	total conditions of the freestream flow
ts	transmitted shock
w	shock generator wedge; also wall
1,2,3,...	flow region (See Figs. 2-7.)

$\delta_{5,abs}$ shear layer turning angle at the wall with respect to the freestream direction

SUPERSCRIPTS

$'$ with respect to the sweep angle

Chapter 1

INTRODUCTION

1.1 Background

At hypersonic speeds, shock waves can interact with a vehicle's surface and cause intense local surface heating and mechanical loads with attendant structural damage. The first in-flight example of the severity of shock wave interference loads on structural components was observed during a test flight of the X-15 research airplane [1-2]*. The purpose of the flight was to evaluate handling characteristics for upcoming flight tests of the Hypersonic Research Engine (HRE), an axisymmetric ram-scramjet. A "dummy" ramjet replica of the HRE was suspended from the X-15 ventral fin. During the Mach 6.7 flight, the shock wave from the conical engine inlet spike intersected the pylon and engine cowl bow shock waves. The resulting shock wave interference patterns produced high speed flow which impinged on the pylon support and engine cowl causing structural damage to both. The damage to the pylon support caused premature separation of the dummy ramjet from the X-15 during its landing approach. Fortunately, the X-15 research airplane was not damaged.

---

* Numbers in [ ] indicate references

Originally, damage was attributed to increased pressure and heating rates caused by vortex sheet impingement on the leading edges of the pylon support and cowl [2]. However, Edney [3] theorized the increased loads resulted from shock impingement heating which caused large temperature gradients in the narrow impingement regions. The attendant thermal stresses from these gradients and high temperatures probably caused the structural failure [4]. His explanations have been supported by more recent work.

Shock interference is also an important design consideration for space transportation systems such as the space shuttle. During the supersonic-hypersonic assent phase of a shuttle mission, shock wave interference occurs in the channel between the shuttle vehicle and external fuel tank, and between the solid rocket booster motors and external fuel tank [5-7]. Supporting struts, which are usually swept to the flow, are exposed to shock wave interference similar to engine cowl leading edges.

The National Aero-Space Plane (X-30) will encounter shock interference loading in several areas during hypersonic flight at speeds up to Mach 25. During a typical mission, the most severe environment will occur on the scramjet engine cowl leading edge as it is subjected to the combined influences of the inlet ramp shock waves and the vehicle bow shock wave. Although the deleterious effects of some of the shock wave interferences may be avoided, the vehicle bow shock wave, which will pass across the cowl leading edge at approximately Mach 16, cannot be avoided. The resulting shock wave interference from this condition is the so-called "shock-on-lip" [8]. Definition of the interference flowfield and resulting surface loads at hypersonic speeds, when high temperature effects are significant, is a formidable challenge to the aerodynamicist.

The first experimental studies to define these surface loads on the X-30 vehicle were documented by Wieting, et al [9,10] and Holden, et al [11,12]. These studies were conducted on a generic wedge-cylinder configuration in the NASA Langley Research Center (LaRC) 8-foot High Temperature Tunnel (8' HTT) and in the Calspan 48-inch and 96-inch Hypersonic Shock Tunnels as a cooperative research program between NASA LaRC and Calspan-University of Buffalo Research Center (CUBRC). (CUBRC is a nonprofit organization formed by Calspan Corporation and State University of New York at Buffalo.) The generic configuration produced two-dimensional shock wave interference patterns representative of a cowl leading edge parallel to an incoming incident shock wave. The most severe loads were observed at Mach 16 for an interference pattern which produced a supersonic jet that impinged on the cylinder and increased heating levels up to 30 times greater than the local (no shock interference) stagnation point heat transfer rate [12].

Results from the experiments [9-12] were compared with computational predictions of shock wave interference phenomena [8,13-18]. The computational predictions showed good resolution of the pressure; however, the local heating rates were underpredicted. The cause of the underprediction is unresolved, but may be improved with finer meshes, high temperature gas models, and turbulence models. The studies used two-dimensional numerical models with minimum grid spacing, on the order of 10^{-5} inches, to capture shock patterns and wall temperature gradients, and hence predict heat transfer rates. The finite element adaptive unstructured meshes used in references 13, 14, 16, and 17 required approximately 9,000 grid points which was approximately one-third the number of grid points used by other approaches [15]. Three-dimensional techniques may require up to

one-half million grid points [19,20]; hence, experimental results are still required to provide a database both for design and code validation.

The actual shock wave interference pattern which will occur on the X-30 cowl leading edge is unknown at this time because the vehicle and engine configuration have not been selected. The incident shock and the cowl leading edge bow shock intersection probably will not be two-dimensional. Rather, the shock wave interference will be either swept, diagonal, or compound with respect to the cowl leading edge. However, as a first step to define the surface effects from the shock-on-lip condition, two-dimensional shock wave interference patterns were studied recently [8-18]. Results from these studies indicate that stress levels for the cowl leading edge are in excess of the elastic limit for candidate structural concepts [18]. Consequently, the cowl leading edge may need to be swept to reduce heat transfer rates. Heat transfer rates and pressures on a cylindrical leading edge, swept in an undisturbed high velocity flowfield, are reduced [21-25], and the reduction of surface heating is a function of the cosine of the sweep angle [24]. However, swept shock wave interference effects which are applicable to a swept cowl leading edge have not been studied. Therefore, surface pressure and heat transfer rates from swept shock wave interference need to be defined.

The present work is an extension of the earlier two-dimensional studies [9-12] in that a swept or three-dimensional configuration has been studied. Since a swept cowl leading edge may be required on the X-30 to reduce the high heating rates, the present experiments are timely. Glass, et al [26] have presented a summary of experimental results for swept shock wave interference tests which have been compared with computational results

[19,20]. However, complete documentation of swept shock wave interference experiments is lacking and is the motivation behind the present study.

1.1 Relevant Shock Wave Interference Research

The six types of interference patterns that can occur from the shock-shock interactions were categorized by Edney [3] in 1968. Edney studied shock wave interference on a hemisphere/cylinder, flat-faced cylinder, and blunted cone/cylinder. His study provided surface pressure and heat transfer rate measurements, high quality schlieren photographs, and an eloquent discussion of the six interference patterns. Also, Edney showed that the location and magnitude of the pressure and heat transfer rate peaks are dependent on the Mach number, freestream flow conditions, incident shock strength, and high enthalpy effects. The most severe shock wave interference pattern was identified as a "Type IV" shock interference. The Type IV interference pattern produced a supersonic jet which impinged on the surface creating a highly localized stagnation region resulting in significantly increased local pressure and heat transfer rates.

Additional studies of shock wave interference have been reviewed in survey papers by Ryan [27] and Korkegi [28]. Early investigations defined the pressure and heat transfer rates on models that represented wings, fins, and other structures which are attached to a high-velocity vehicle and might interfere with the forebody shock [29-36]. However, the observed flowfields and surface effects were not explained completely. These earlier studies [29-36] were on models that consisted of a blunt cylindrical leading edge mounted transversely with respect to a flat plate incident shock generator at 0° yaw. The blunt leading edge was swept at various angles with respect to the flat

plate, and an incident shock intersected a bow shock transverse to the incident shock plane. These experimental studies reported significant increases in local surface pressure and heat transfer rates on a 0° swept cylinder [29,35,36]. The high surface loads on the cylinder were reduced as the cylinder was swept back relative to vertical. When the cylinder was highly swept, surface pressure and heat transfer rates on the cylinder were affected minimally downstream of the shock wave interference because the interference patterns that cause high pressure and heating were not present or dissipated prior to intersecting the surface.

Spurred by the work of Edney and others, experimental studies and prediction techniques of shock wave interference were numerous from the early to mid 1970's. (For example, see references 37-47.) Most of the experimental studies were conducted in hypersonic wind tunnels at NASA LaRC [38-41,46,47] on hemispherical configurations similar to those used by Edney [3]. For these tests, the shock wave interference pattern was produced by the interaction of a planar incident shock with the bow shock from an axisymmetric blunt body. The experimental data were compared with correlations [38-40] and numerical predictions of peak pressure and heat transfer rate using oblique shock theory [42]. Results from the computer program were in good agreement with the experimental results. Unfortunately, the procedure relied on experimental data to calculate the surface pressure and heat transfer rate peaks and most of the data were for a calorically perfect gas.

The first two-dimensional shock wave interference study was reported by Craig and Ortwerth [37] in 1971. The study was conducted at Mach 15 on a six-inch diameter semi-cylindrical blunt leading edge with a 20° wedge as the incident shock generator. The shock generator and cylindrical leading edges

were parallel and produced a two-dimensional interference pattern which impinged on the cylindrical leading edge parallel to its axis. The experiment simulated shock wave interference which occurs from centerbody and cowl shock interaction on a hypersonic ramjet during flight. This was the first interference study where the incident shock plane intersected a two-dimensional bow shock. The experimental results were limited because instrumentation spacing in the shock impingement region was too coarse to capture the leading edge interference effects. However, their experiment was significant because it was the first published two-dimensional shock wave interference study.

A two-dimensional numerical study of shock wave interference was reported by Tannehill, et al [45,46] in 1976. Two-dimensional computational results from a time-dependent, finite difference computer program were compared with experimental results. The computer program solved the complete Navier-Stokes equations. Numerical results [45] were compared initially with the axisymmetric experimental data given by Edney [3] because no acceptable two-dimensional experimental results were available. However, Keyes [47] conducted a series of two-dimensional interference tests in 1975 in the NASA LaRC 20-Inch Mach 6 Tunnel. Though his results were not released in completed form, parts of the data were used in comparison with the computational results of Tannehill, et al [46]. The computational and experimental pressure and heat transfer rate results were in good agreement.

Shock wave interference studies continued through the mid 1970's, but then suffered a hiatus of about 10 years. Recently, renewed interest in shock wave interference has been stimulated by the X-30 vehicle, where high loads occur on various regions of the vehicle. Shock wave interference heating

occurs when the vehicle bow shock or engine inlet ramp shocks intersect the cowl leading edge bow shock.

The earlier studies [1-3,5-7,27-47] produced an insight into the problem of increased pressure loads and heat transfer rates from shock wave interference. However, several factors limited the applicability of the earlier studies in relation to the current X-30 shock-on-lip research. Low enthalpy freestream wind tunnel tests did not address the effect of a high temperature real gas on the shock wave interference. High temperature effects will surely occur at X-30 flight conditions. Coarse spacing of model instrumentation also did not define adequately the peak pressure and heat transfer rates due to shock wave interference impingement. Also, most of the earlier studies were for axisymmetric model configurations, and the cowl leading edge on the X-30 research vehicle will be cylindrical.

1.2 Purpose of the Present Shock Wave Interference Research

The present shock wave interference experiments have attempted to measure the increased pressure and heat transfer rates produced by a swept interference pattern. The test configuration produced a swept incident shock which intersected with a swept bow shock parallel to the axis of the cylindrical leading edge. The resulting quasi two-dimensional shock interaction occurs along the cylinder axis at the same circumferential position. The configuration simulates shock wave interference on a swept inlet cowl or swept splitter plate of a scramjet engine. The present study provides the most complete documentation of experimental results of this type to date. It is hoped that they can be used to verify three-dimensional computational results for swept shock wave interference.

The present tests were conducted in the Calspan 48-inch Hypersonic Shock Tunnel (48" HST) as a cooperative research program between NASA LaRC and CUBRC. The experimental interference model was swept at 0°, 15°, and 30°. The nominal test conditions of Mach 8, unit Reynolds number of 1.5×10^6 per foot, dynamic pressure of 800 psf, and total temperature of 2800°R were used. These test conditions were the same as the previous Mach 8 tests performed by Wieting, et al [9,10] and Holden, et al [11,12] in order to obtain a direct comparison of the effect of sweep on the surface loads.

This thesis is arranged in the following manner: First, the background and motivation for the present shock wave interference research is given. Then, a brief discussion is presented of inviscid features and surface effects produced by the six interference patterns categorized by Edney [3]. Next, a description of the experiment, including the hypersonic shock tunnel and swept interference model, is presented. Finally, results from the swept shock wave interference experiment are presented and discussed.

Chapter 2

DESCRIPTION OF SHOCK WAVE INTERFERENCE

Edney [3] categorized six interference patterns and the resulting surface pressures and heat transfer rates that occur when a weak oblique shock wave intersects a bow shock at various locations. Features of the inviscid flowfield show the physical mechanisms that cause these interference patterns. Although Edney discussed each interference pattern in detail [3], a brief description of the inviscid features of each pattern is given in section 2.1 to acquaint the reader with the basic flow features and define the conditions which have been observed. Because several of these patterns result in similar surface interactions (such as shock wave-boundary layer), the effect of the interference pattern on the local surface heat transfer rate is discussed in section 2.2.

2.1 Shock Wave Interference Patterns

Using Edney's method of interference categorization [3], the shock wave interference pattern is determined by the location where the incident and bow shock waves intersect and by the leading edge slope at the impingement point as shown in Fig. 1. Type I, II, and V shock wave interference patterns result in a shock wave-boundary layer interaction at the blunt leading edge surface. Those interactions increase the pressure and heat transfer rates at the

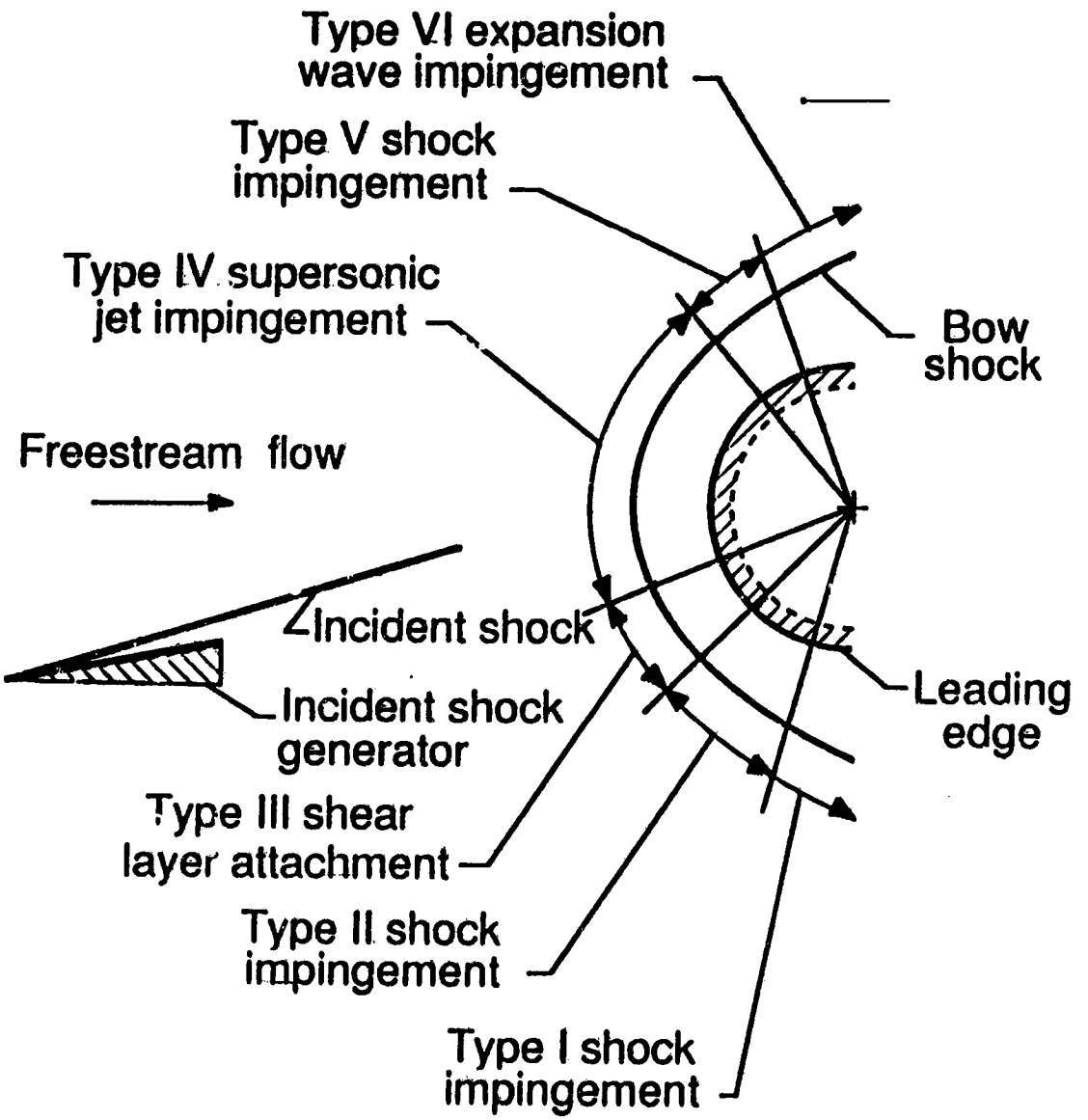

Fig. 1. Location of the six shock wave interference patterns on a leading edge.

surface. The Type VI interference pattern results in an expansion fan-boundary layer interaction that reduces the surface pressure and heat transfer rates. The Type III interference pattern produces a shear layer that attaches to the boundary layer and increases surface pressure and heat transfer rates. If the shear layer is turbulent when it attaches to the boundary layer, heating can increase to levels above those caused by shock wave-boundary layer interaction. The greatest increase in pressure and heat transfer rates is caused by the Type IV supersonic jet impingement on the leading edge.

In general, all two-dimensional interference patterns can be grouped as either the intersection of shocks of opposite families or the intersection of shocks of the same family [48]. Intersection of shocks of opposite families occurs when a left-running and a right-running shock wave intersect. This causes either Type I, Type II, Type III, or Type IV interference depending on the relative shock strengths of the two shock waves [3]. Intersection of shocks of the same family occurs when either two left- or right-running waves intersect and result in either the Type IV, Type V, or Type VI interference patterns. Notice that the Type IV interference pattern can occur from the intersection of shocks of opposite families or of the same family. This depends on whether the incident shock intersects above or below the normal shock portion of the bow shock. The reader is referred to Edney [3] for a complete discussion of the difference. The common convention used to describe a left-running wave is that it turns a supersonic flow to the left from an observer positioned on the flow streamline. A left-running wave turns the flow through a positive deflection angle. The opposite is true for the right-running wave. This convention is used for the present discussion.

Inviscid flow features of each interference pattern are presented in the following sections. Schematic and pressure-deflection diagrams of six

flowfield examples are used in the discussion. The pressure-deflection diagram is the locus of points describing all possible flow deflection angles and static pressures behind both weak and strong oblique shock waves for a given Mach number. The diagram is commonly called a "Mach number heart curve" because its shape resembles a heart. Five of the six shock wave interference examples discussed were taken from reference 42. The exception being the Type IV interference example which is a calculation of an interference test reported by Wieting [9].

2.1.1 Type I Interference Pattern

The Type I interference pattern occurs when two weak oblique shock waves of opposite families intersect as shown schematically in Fig. 2(a). The weak shocks are generated by either two sharp leading edges or by a sharp leading edge and a bow shock sufficiently downstream of the sonic point on the bow shock wave. The freestream flowfield (region 1) is turned by the two weak shock waves and results in the flow in regions 2 and 3. The two shock waves intersect and continue as refracted shock waves downstream of the intersection point [48]. The flowfields for regions 4 and 5 are behind the two refracted shock waves. The flow direction and pressure in regions 4 and 5 are the same and are separated by a shear layer because the velocities in regions 4 and 5 differ. The refracted shock wave separating regions 2 and 4 intersects the surface resulting in a shock wave-boundary layer interaction. Then, the flowfield in region 4 is turned through an oblique shock wave to match the angle of the upper wall boundary in region 6. Pressure and heating amplification at the shock wave-boundary layer interaction are dependent on the impinging shock strength and boundary layer state [35,36,38,40-42,49-58].

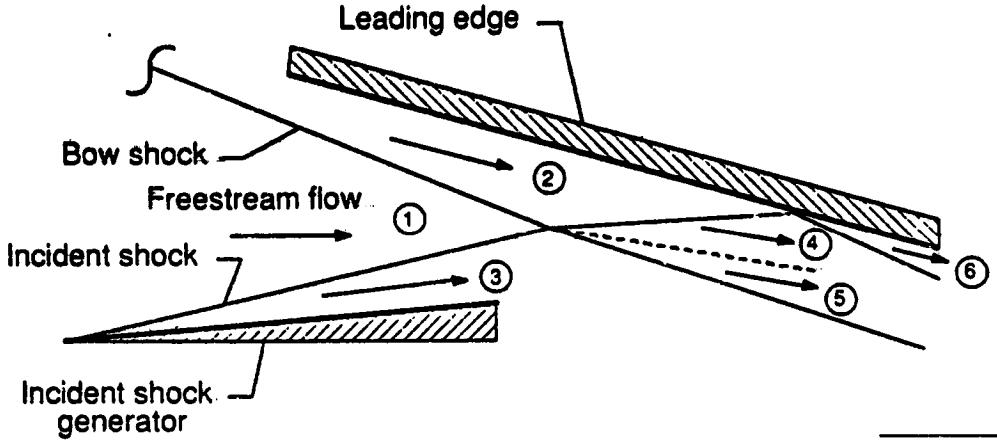

a) Schematic diagram

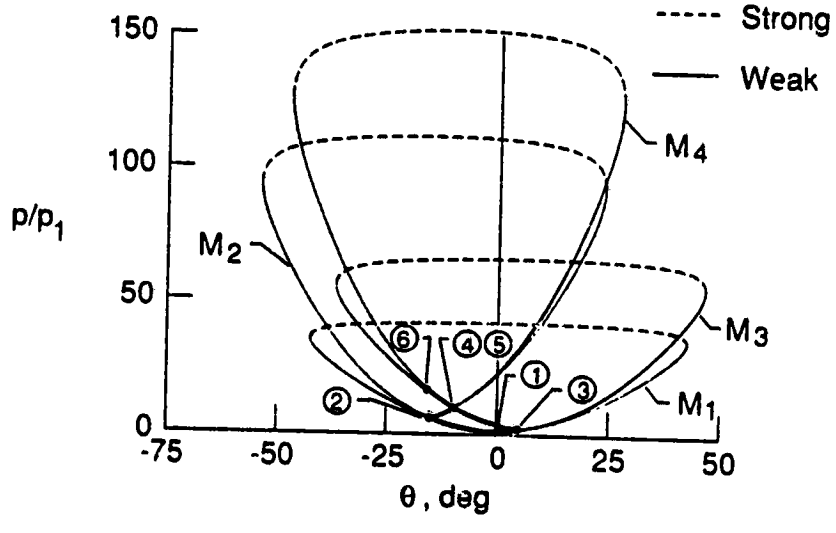

b) Pressure-deflection diagram

Fig. 2. Type I shock wave interference pattern.

This shock interference can be shown graphically on the pressure-deflection diagram shown in Fig. 2(b). The freestream flow, region 1, is turned downward through a right-running wave to region 2 and upward through a left-running wave to region 3. The intersection of the pressure-deflection curve of region 2 with the curve of region 3 defines the equal pressure and flow direction requirement of the resulting flow in regions 4 and 5. Note that the region 2 and 3 curves also intersect the freestream flow curve, but at a pressure above the intersection with each other. When this situation exists, the resulting interference flowfield will always occur at the lower pressure, i. e., at the intersection of the region 2 and 3 pressure-deflection curves.

2.1.2 Type II Interference Pattern

The Type II interference pattern, shown schematically as Fig. 3(a), is similar to the Type I pattern because both result from the intersection of shocks of opposite families and result in a shock wave-boundary layer interaction. However, with the Type II interference, the right-running wave is stronger than the one for the Type I, but still results in supersonic flow in region 2. For the case of incident shock intersection with a bow shock, the intersection point on the bow shock is just downstream of the sonic point. The pressure-deflection diagram for the Type II interference is shown in Fig. 3(b). The freestream flow (region 1) is turned through two weak shocks to regions 2 and 3. Unlike the Type I interference, the intersection of the pressure-deflection curves for regions 2 and 3 is above their intersection with the strong shock solution of the freestream flow (region 1). The transition point between the Type I and Type II interference is characterized by the movement of the the region 2 to region 3 intersection point to a pressure above the strong shock solution of the region 1 curve. Because all three regions must be linked, the only valid solution is one

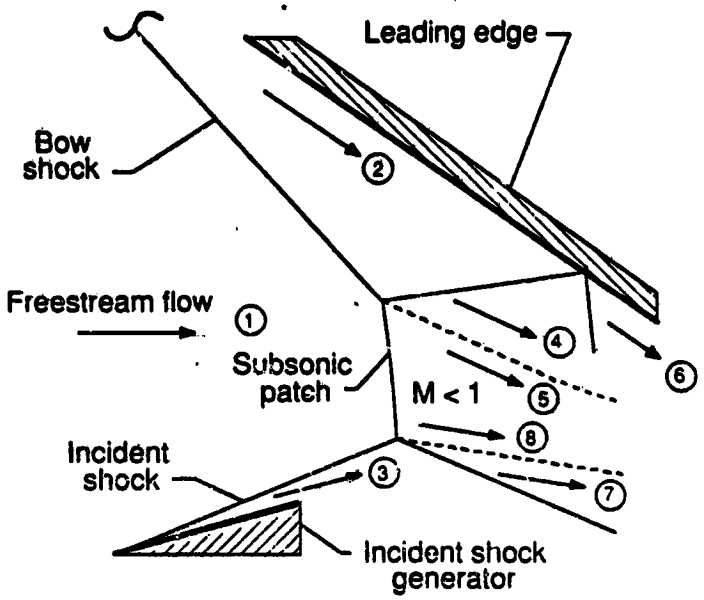

a) Schematic diagram

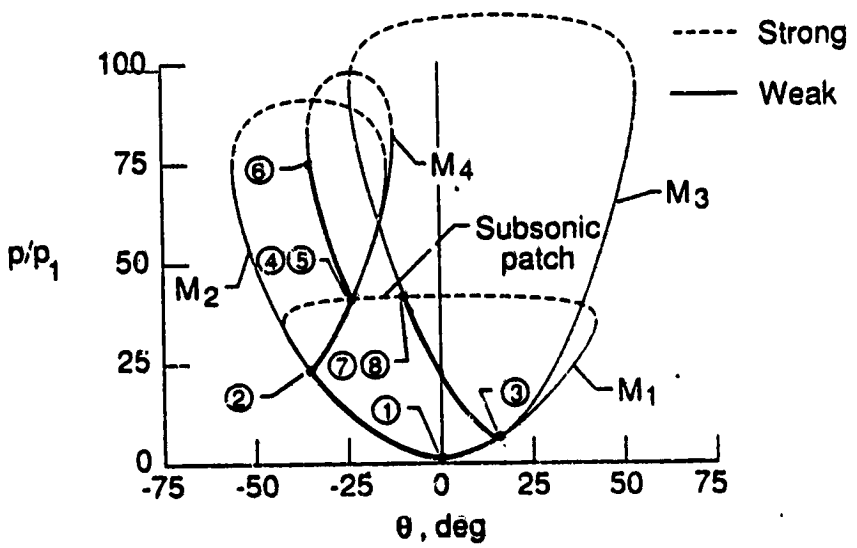

b) Pressure-defléction diagram

Fig. 3. Type II shock wave interference pattern.

in which regions 2 and 3 are linked to region 1 through the subsonic patch as shown in the figure.

The pressure and flow angle in region 4 and 5 is determined by the intersection point of the region 2 pressure-deflection curve with the region 1 curve. Flow in region 4 is supersonic because it results from a weak compression of flow from region 2. However, region 5 flow is subsonic because it results from compression of the freestream flow through a strong shock wave. Likewise, the pressure and flow angle in regions 7 and 8 is determined by the intersection of the region 3 and region 1 curves. Region 7 flow is supersonic, and region 8 flow is subsonic. The two supersonic flow regions (regions 4 and 7) are separated by shear layers from the subsonic flow. Note that the extent of the subsonic region is not given. Both pressure and velocity variations occur between the shear layers separating regions 4 and 7.

The surface effects from the Type II interference are similar to those of the Type I. The flowfield in region 4 is turned to match the angle of the upper wall boundary. The shock wave upstream of region 4 impinges on the wall boundary layer and results in shock wave-boundary layer interaction at the wall, therefore, affecting the wall boundary layer similar to the Type I interference.

2.1.3 Type III Interference Pattern

The Type III interference is caused by the intersection of shocks of opposite families when a weak incident shock intersects a bow shock inside the lower subsonic region. The schematic diagram for this interference pattern is shown in Fig. 4(a). The left-running incident shock wave turns the freestream flow upward to region 3 and intersects the bow shock. Behind the intersection

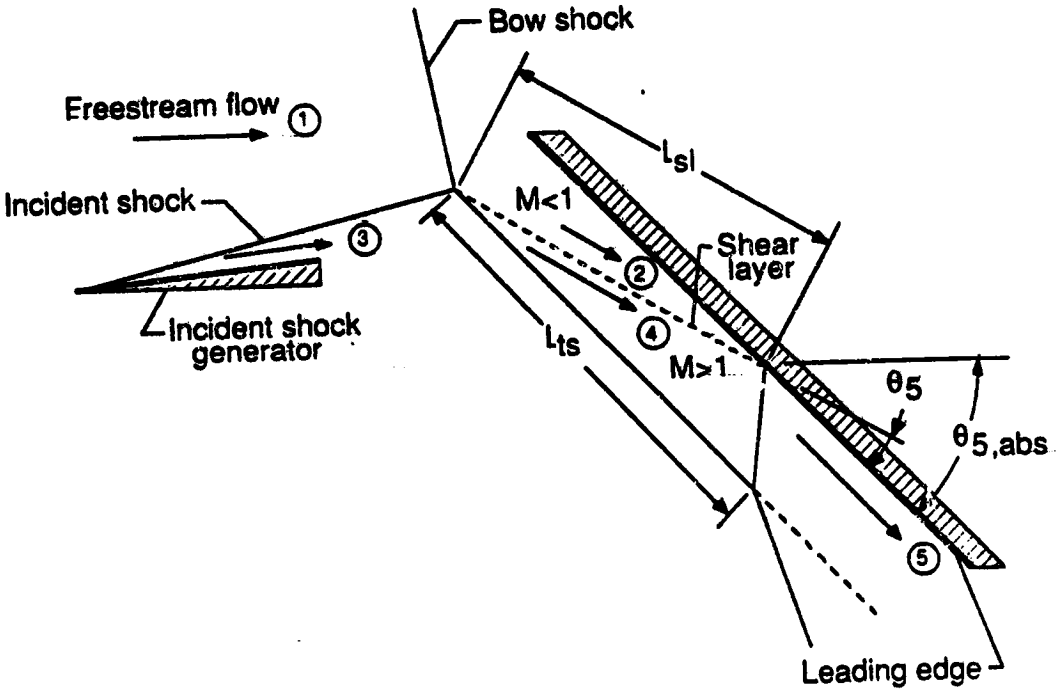

a) Schematic diagram

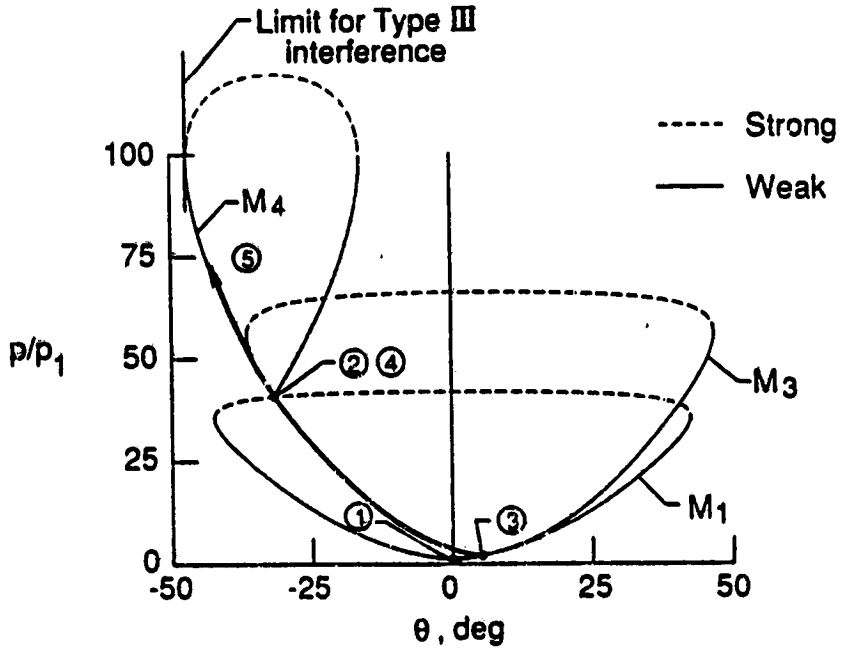

b) Pressure-deflection diagram

Fig. 4. Type III shock wave interference pattern.

point, the flow in regions 2 and 4 are at the same pressure and are turned to the same flow angle. The flow is subsonic in region 2 and supersonic in region 4, and these two regions are separated by a shear layer.

The pressure-deflection diagram for the Type III interference is shown as Fig. 4(b). Pressure in region 3 is located on the region 1 pressure-deflection curve at the appropriate turning angle. The turning angle and pressure of the flow in regions 2 and 4 are determined by the intersection of the region 1 and 3 pressure-deflection curves. The shear layer that separates region 2 from region 4 will attach to the wall boundary layer and cause a shear layer-boundary layer interaction. The effect of the interaction depends on the impingement angle (θ_S) between the shear layer and the wall boundary layer, pressure rise between regions 4 and 5, and if the shear layer is laminar or turbulent.

The transition from Type II to Type III interference occurs when the flow turning angle to region 2 is greater than the maximum turning angle for a supersonic flow solution to exist in region 2. The transition is determined by the intersection point of the incident shock with the bow shock sonic point. An intersection below the sonic point in the supersonic region behind the bow shock produces a Type II interference pattern. Above the sonic point, a Type III interference pattern is produced. This transition is also seen by comparing the Type II and Type III pressure-deflection diagrams shown in Figs. 3(a) and 4(a), respectively. The pressure and turning angle of region 2 flow are uniquely defined by the wall (or shock wave) turning angle for a Type II interference. (See Fig. 3(a).) However, for the Type III interference, the pressure and turning angle in region 2 are dependent and defined by the intersection of the region 3 curve with the region 1 curve as shown in Fig. 4(b). Note that the shear layer length, L_{sl}, and the transmitted shock length, L_{ts}, are

dependent on body shape and intersection conditions, and hence are undefined.

A more subtle transition is present for the change from Type III to Type IV interference. The transition occurs as the incident shock intersects closer to the normal shock portion of the bow shock. The region 4 curve shown in Fig. 4(b) defines the pressure increase to region 5 for various wall turning angles. If the wall turning angle is greater than the maximum turning angle given by the pressure-deflection curve for region 4, the Type III interference will transition to a Type IV interference.

2.1.4 Type IV Interference Pattern

The Type IV interference pattern is caused by the intersection of either shocks of opposite families or shocks of the same family. The intersection point of the incident shock with the bow shock can be above or below the normal shock portion of the bow shock as shown in Fig. 1. However, both result in a Type IV interference pattern as shown schematically in Fig. 5(a).

When the wall turning angle is greater than the maximum turning angle of the region 4 curve shown in Fig. 4(b), the Type III interference will transition to a Type IV as discussed in section 2.1.3. The onset of the Type IV interference becomes apparent with the formation of a well defined supersonic jet embedded within the subsonic regions between the bow shock wave and the surface. The supersonic jet is separated by shear layers from the subsonic flow in regions 2 and 5 as shown in Fig. 5(a), and may impinge on the blunt leading edge.

A pressure-deflection diagram for Type IV interference is shown in Fig. 5(b). Up to region 4 the flow process is identical to the Type III interference. Supersonic flow in region 4 is turned through a weak left-running wave to

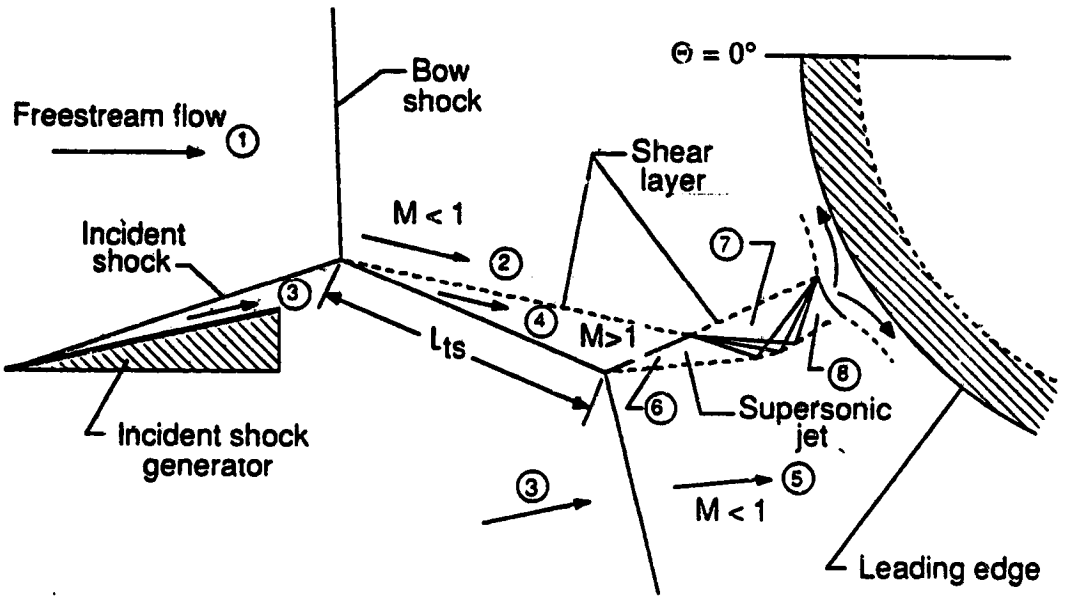

a) Schematic diagram

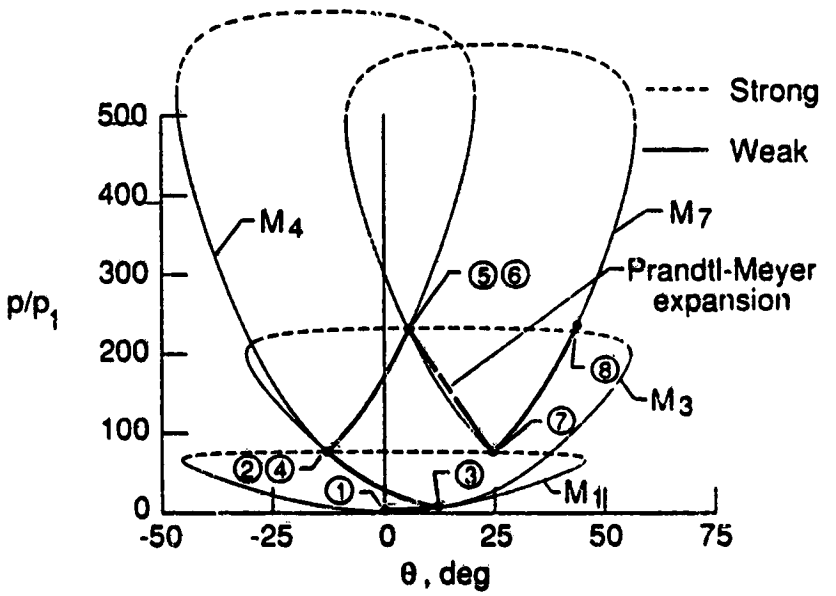

b) Pressure-deflection diagram

Fig. 5. Type IV shock wave interference pattern.

region 6. Flow in region 6 matches flow direction and pressure with the subsonic flow in region 5. Supersonic flow from region 6 to region 7 is expanded through a Prandtl-Meyer expansion fan to match the pressure in region 2 shown as a dot-dash line in Fig. 5(b). Supersonic jet flow is recompressed from region 7 to region 8 through a series of left-running waves to again match the pressure in region 5. The jet is terminated at the surface by a jet bow shock because the wall turning angle is greater than the maximum turning angle of the supersonic flow in the jet. Keyes and Hains [41] have shown that the supersonic jet terminates in either region 7 or 8 for freestream Mach number between 6 and 20 when the jet impinges on the surface. Weak compression of the flow in the jet and then compression through the jet bow shock results in high localized pressure and heating at the wall.

Note that the supersonic jet is turned upward for the example shown schematically in Fig. 5(a) because the pressure in region 5 is greater than in region 2. The supersonic jet is turned by the higher pressure in region 5 to the lower pressure in region 2. Impingement of the jet above $\Theta = 0°$ gives a Type IV interference which grazes the surface or dissipates prior to impinging on the surface.

2.1.5 Type V Interference Pattern

The Type V interference pattern occurs when the incident shock intersects the bow shock just above the upper sonic point. Both shocks are of the same family. A schematic of the Type V interference is shown in Fig. 6(a). A supersonic jet is present for the Type V interference; however, the jet is much thinner than the Type IV supersonic jet. The Type V jet turns away from the surface, dissipates, and does not impinge on the surface.

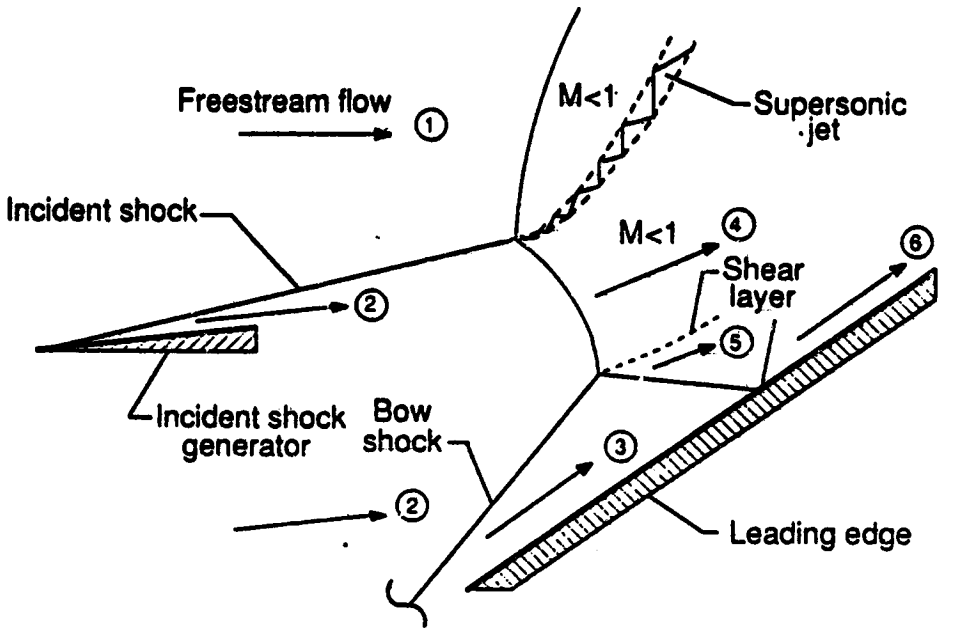

a) Schematic diagram

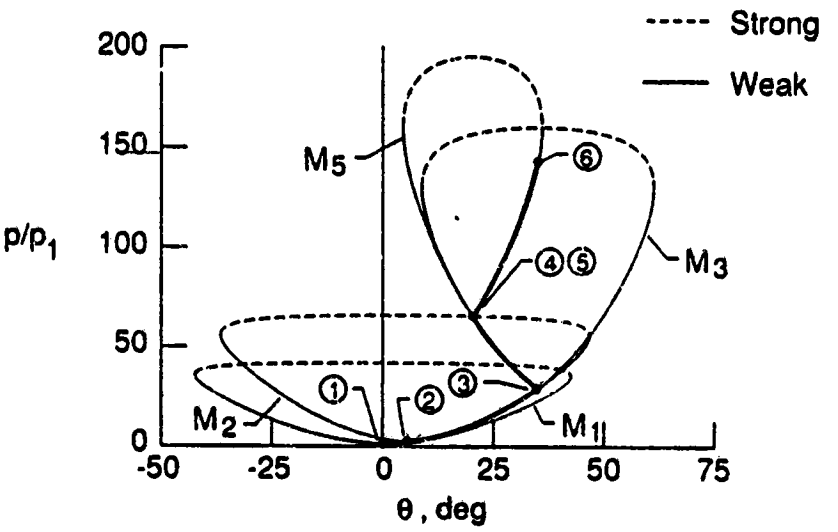

b) Pressure-deflection diagram

Fig. 6. Type V shock wave interference pattern.

A pressure-deflection diagram for Type V interference is shown in Fig. 6(b). The flow that affects the surface is initially compressed to region 2 through the weak, left-running incident shock wave. Then, flow in region 2 is compressed to region 3 by flow deflection to match the wall turning angle. A requirement of the flow in regions 4 and 5 is that the pressure and flow turning angles must match at the shear layer which separates them. The intersection of the pressure-deflection curves of regions 2 and 3 shown in Fig. 6(b) satisfies this set of conditions. Therefore, region 3 flow is compressed to region 5 through a right-running wave to match the pressure and flow direction in region 4. The right-running shock wave that impinges on the wall boundary layer results in the shock-boundary layer interaction at the wall. The increased pressure and heat transfer rate at the surface caused by a shock-boundary layer interaction is similar to the surface effects of the Type I and Type II interference.

2.1.6 Type VI Interference Pattern

Type VI interference results from the intersection of shocks of the same family similar to Type V interference. However, the incident shock must intersect the bow shock sufficiently downstream of the upper sonic point so that supersonic flow exists in all regions for a Type VI interference to be present.

A schematic and pressure-deflection diagram of Type VI interference are shown in Figs. 7(a) and 7(b), respectively. The freestream flow (region 1) is initially compressed through the weak left-running incident shock wave to region 3. Then, flow is compressed from region 3 to region 4 by another left-running wave to the local turning angle at the wall. These two left-running shock waves coalesce, and the resulting shock wave compresses the flow from region 1 to region 2. Pressure and flow direction are matched in regions

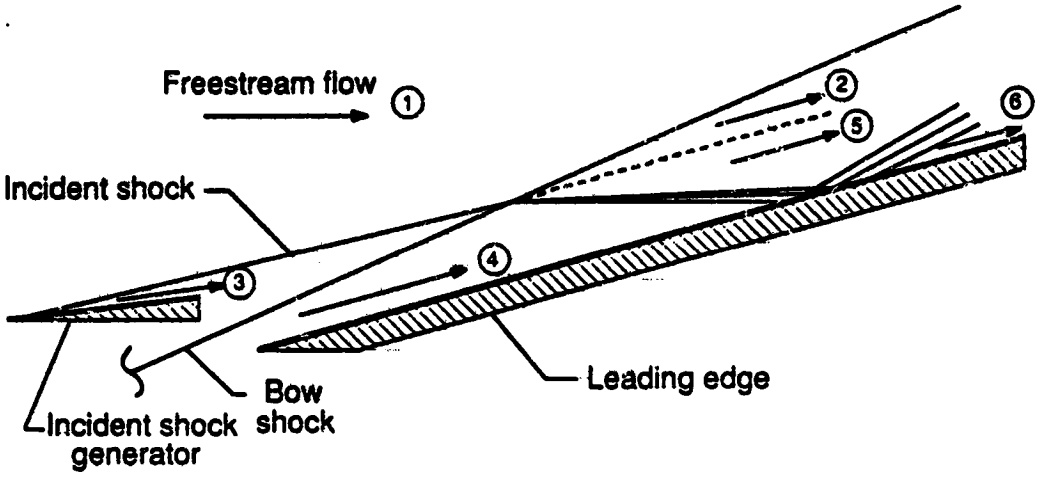

a) Schematic diagram

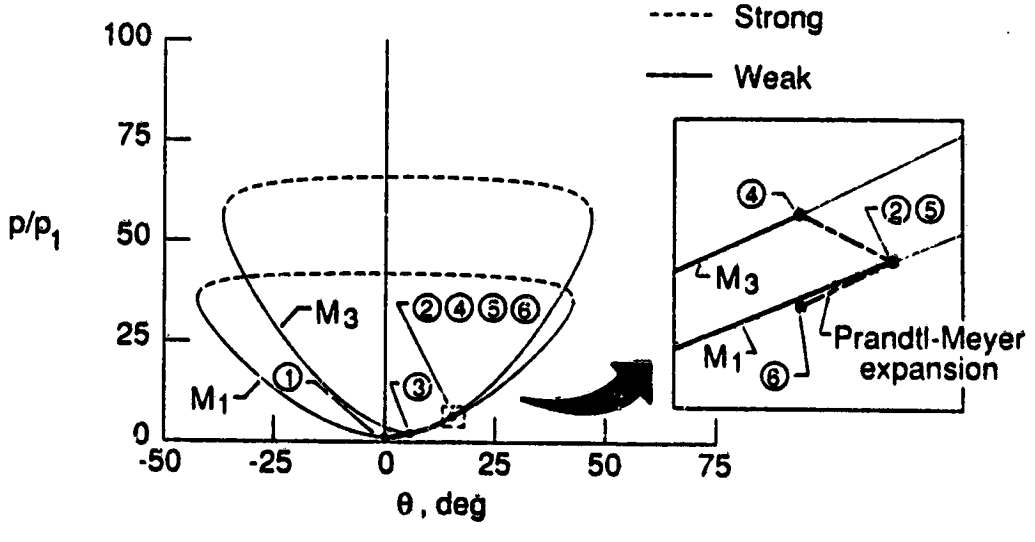

b) Pressure-deflection diagram

Fig. 7. Type VI shock wave interference pattern.

2 and 5, and the match point will be located on the region 1 pressure-deflection curve. The match is found by expanding isentropically from the flow conditions in region 4 to its intersection with the region 1 pressure-deflection curve as shown on the inset of Fig. 7(b). Therefore, region 4 flow must expand through a Prandtl-Meyer expansion fan to match the pressure in region 2. The expansion fan impinges on the wall boundary layer and results in the expansion fan-boundary layer interaction surface effect associated with Type VI interference. Region 5 flow expands to region 6 because the expansion fan reflects from a solid boundary in a like manner [48]. This interaction decreases the local pressure and heat transfer rate at the surface.

2.2 Surface Heating From Shock Wave Interference

The discussion given in section 2.1 is useful to determine the inviscid shock wave and flowfield features of the various interference patterns. Peak surface pressure can be determined from the pressure-deflection diagram for the given type of interference pattern. However, the viscous effects that affect heating on the blunt leading edge surface have not been addressed. The purpose of this section is to discuss these viscous effects. To this end, a brief discussion of some empirical correlations used to determine the peak surface heat transfer rates that result from shock wave interference is given.

Shock wave-boundary layer interaction increases pressure and heat transfer rates and results from Type I, Type II, and Type V interference. Pressure and heat transfer rates are reduced from the expansion fan-boundary layer interaction of the Type VI interference. The Type III interference affects the heat transfer rate at the surface by a shear layer attachment to the boundary layer. Shear layer-boundary layer attachment can

increase heat transfer rates above the level for the shock wave-boundary layer interaction if the shear layer is turbulent. The greatest increase in heat transfer rates is caused by the Type IV supersonic jet impingement on the blunt leading edge.

2.2.1 Shock Wave-Boundary Layer Interaction

Surface pressure and heat transfer rate augmentation caused by the Type I, Type II, and Type V interference patterns is a result of shock wave-boundary layer interaction. The flow physics of the shock wave-boundary layer interaction are covered in great detail in many of the classic compressible fluids text books. The reader is referred to those by Schlichting [49], Shapiro [50], Cox and Crabtree [51], and, most recently, Anderson [52]. The list of articles on shock wave-boundary layer interaction is extensive [35,36,38,40-42,53-58] and only a few have been included.

The condition of the boundary layer prior to shock wave interaction is important in the determination of heat transfer augmentation. A shock wave-laminar boundary layer interaction may cause boundary layer separation just upstream of the interaction point. Pressure waves are propagated upstream through the subsonic region of the boundary layer and cause the boundary layer to adjust before the shock interaction region. However, the turbulent boundary layer has a much thinner subsonic region, and therefore, results in less flow adjustment and less separation prior to the shock wave interaction region.

A simple empirical relationship has been used to estimate the shock wave-boundary layer interaction heating [53]:

$$\frac{q_2}{q_1} = \left(\frac{p_2}{p_1}\right)^n \qquad (1)$$

where subscript 1 refers to the pressure and heat transfer rate upstream of the refracted shock and subscript 2 refers to the peak pressure and heat transfer rate downstream of the reflected shock wave. The experimentally determined value of the exponent, n, in equation (1), for the shock wave-laminar boundary layer interaction varies from 1.29 [35,38,40-42,53,56] to 0.5 [35,52,56]. Kaufman and Johnson [57] suggested that the shock wave interaction disturbance in the laminar boundary layer caused boundary layer transition that strongly affected the local heating. The laminar data they present [57] do not support the simple correlation of peak pressure to peak heat transfer rate given by equation (1). However, for shock wave-turbulent boundary layer interaction, n = 0.85 appears to give the best empirical curve fit for most turbulent experimental data [35,40-42,52-56].

2.2.2 Expansion Fan-Boundary Layer Interaction

An expansion fan-boundary layer interaction at the leading edge surface results from a Type VI interference. The empirical relationship given as equation (1) has been shown to apply to the reduction of heating from the expansion fan-boundary layer interaction [41,42,54]. Morris and Keyes [42] suggest using n = 1.29 for the laminar boundary layer interaction and n = 0.85 for the turbulent boundary layer interaction. Experimental data presented by Keyes and Hains [41] and Back and Cuffel [54] support this approach. The subscripts of equation (1) are defined as 1 for the upstream undisturbed value and 2 for the reduced value downstream of the expansion fan-boundary layer interaction.

2.2.3 Shear Layer-Boundary Layer Interaction

Shear layer attachment to the boundary layer increases heating for the Type III interference. Peak heating at the shear layer attachment point is analogous to the attachment of a separated boundary layer [38,40-42]. Keyes and Morris [38] and Hains and Keyes [40] suggest using a relationship similar to that given by Bushnell and Weinstein [59] to calculate the increased heat transfer rate. This relationship is given as:

$$q_p = A\rho_{w,5}\, u_5\, c_p\, (T_{aw} - T_w) \left(\frac{\mu_w \sin\theta_5}{\rho_w u_5 t_{sl}}\right)^n \qquad (2)$$

where the constants A and n for a laminar shear layer attachment are 0.19 and 0.5, respectively. For a turbulent shear layer attachment, the constants are 0.021 and 0.2, respectively. These values for the constants A and n are taken from reference 59. The subscript 5 refers to region 5 shown in Fig. 4(a).

The state of the shear layer will determine if it is laminar or turbulent [39]. The shear layer thickness, t_{sl}, is calculated by the following relationships taken from reference 59. The thickness for a laminar shear layer is given as:

$$t_{sl} = 0.5 \left(\frac{L_{sl}\, \mu_4}{\rho_4\, u_4}\right)^{0.5} \qquad (3a)$$

and the thickness for a turbulent shear layer is given as:

$$t_{sl} = 0.123 L_{sl} \qquad (3b)$$

where the shear layer length, L_{sl}, and the wall turning angle, θ_5, are determined from the geometry of the interference pattern shown in Fig. 4(a). Calculation of the increased heating using this method is limited because an experimentally determined shear layer length, L_{sl}, is required. (See Fig. 4(a).)

2.2.4 Supersonic Jet Surface Impingement

A Type IV interference pattern terminates at the blunt leading edge by supersonic jet impingement. This causes a narrow, localized stagnation region of high pressure and heat transfer rates. The supersonic jet terminates through a strong shock in either region 7 or 8 shown in Fig. 8 for freestream Mach number between 6 and 20 [42]. It is assumed that the terminating shock is a normal shock and will have little affect on the jet stagnation pressure because it is strong. However, the jet stagnation heating will vary with the sine of the impingement angle [3], θ_j, shown in Fig. 8. Maximum heat transfer rate will occur when the jet impinges normal to the surface.

The surface pressure at the jet impingement is calculated by assuming stagnation flow downstream of the jet bow shock starting with region 7 and 8 upstream flow conditions. The stagnation heat transfer rate [60] is calculated on an equivalent "jet body" radius, R_{bj}, shown in Fig. 8 for the calculated jet width and normal shock density ratio. The jet width, w_j, is determined by solving the inviscid compressible flow relationships [48] to obtain the jet geometry shown in Fig. 5(a). The jet width is dependent on the freestream flow conditions, incident shock strength, and an experimentally obtained transmitted shock length, L_{ts}. Next, the jet bow shock standoff distance, L_s, is calculated from an empirical formula given in references 41 and 42 as $L_s/w_j=0.45$ which is applicable for jet Mach number from 1.2 to 2.5. Having found the jet bow shock standoff distance, the jet body radius is determined using relationships such as those given by Van Dyke and Gordon [61] or Hayes and Probstein [62].

A calculation of the peak heat transfer rates for supersonic jet impingement using the procedure outlined above is cumbersome, includes many assumptions, and requires knowledge of the transmitted shock length to

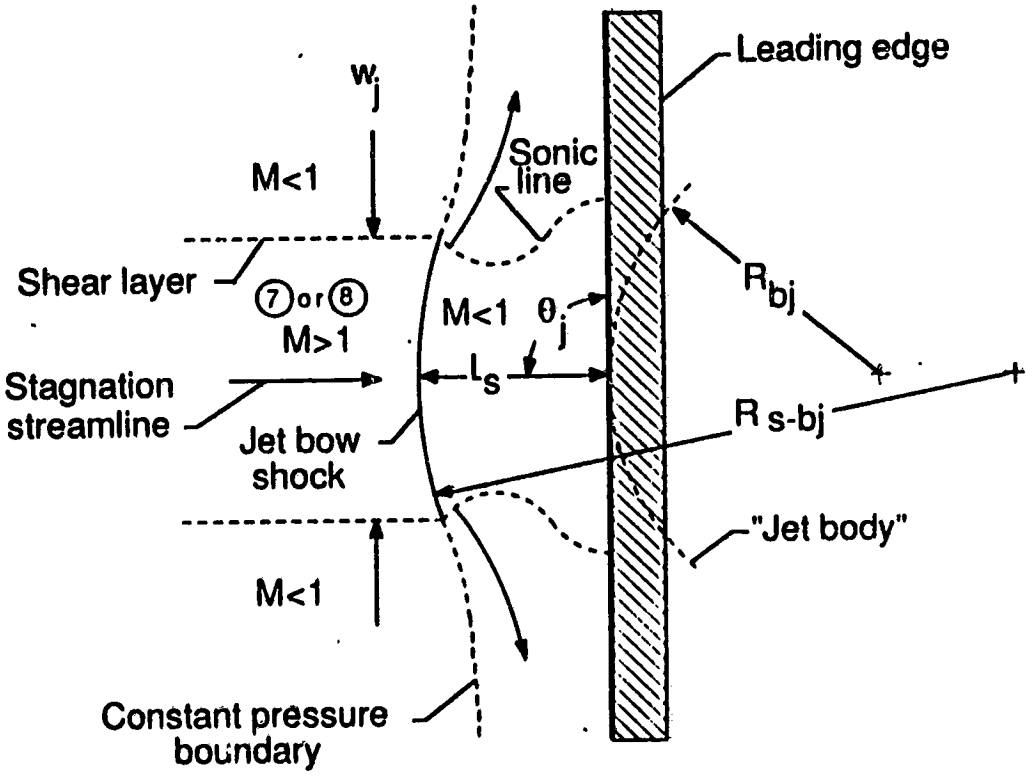

Fig. 8. Schematic diagram of the Type IV supersonic jet impingement region [42].

determine the jet width. However, correlations with experimental data are quite good for both an axisymmetric configuration [40-42] and a two-dimensional body [26] with supersonic jet impingement.

A sketch of the Type IV supersonic jet impingement region and resulting pressure and heat transfer rate distributions are shown in Fig. 9. These details were first postulated by Edney [3] and are included in this study to describe the surface effects from the supersonic jet impingement. The supersonic jet is terminated just before the blunt leading edge by a normal shock wave that causes pressure and heating to increase in a narrow stagnation region between points c and d as shown in Fig. 9. The peak pressure and heat transfer rate will occur at stagnation point o and are a function of the impingement angle that the jet makes with the blunt leading edge surface. The jet splits to flow in both directions and passes through a series of expansion and compression waves from point c to point a and from d to f to match the pressure in regions 5 and 2, respectively. A sketch of the attendant pressure and heat transfer rate variations are shown in Fig. 9. These trends are evident in the data presented in Chapter 4 for the Type IV shock wave interference.

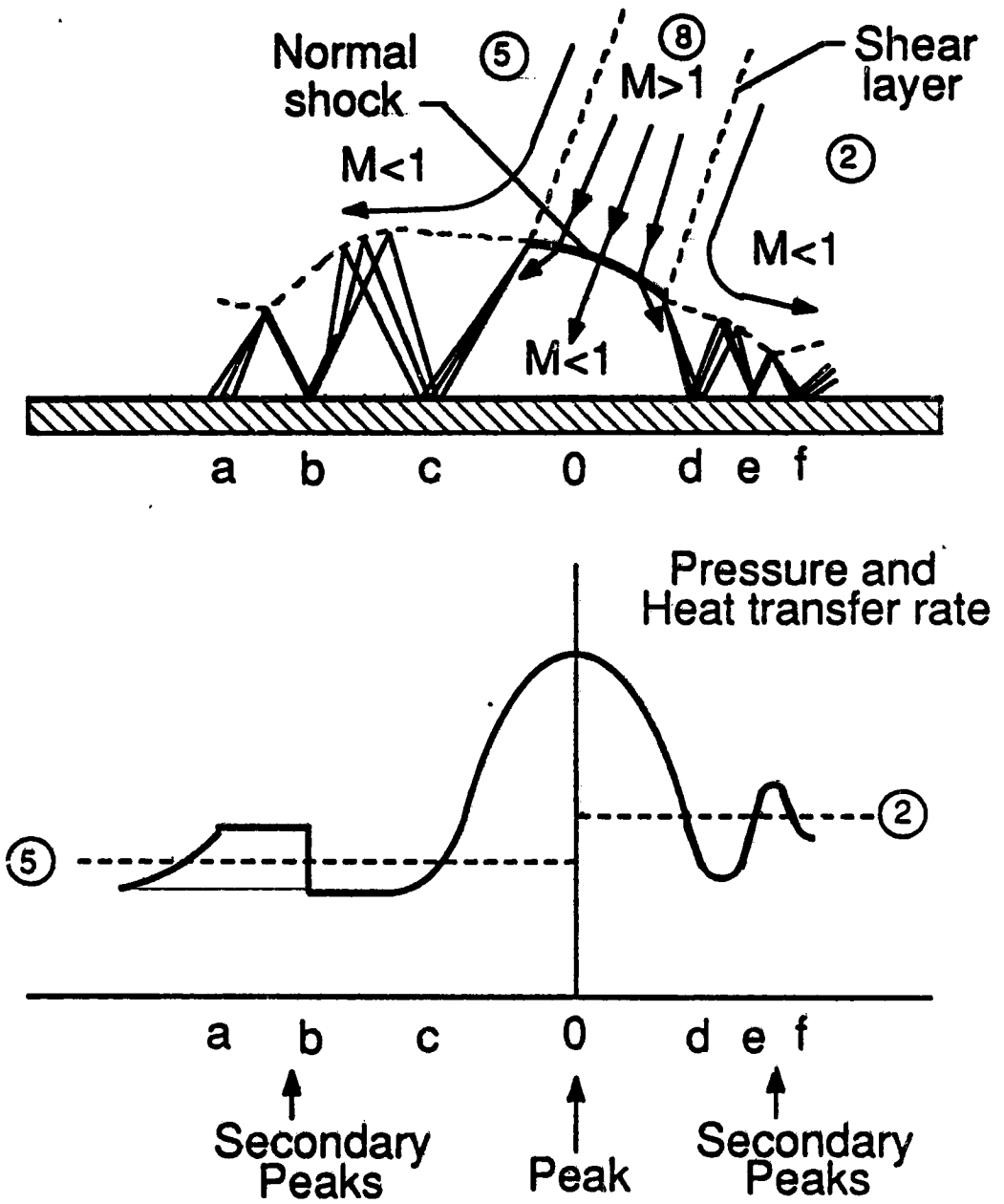

Fig. 9. Sketch of Type IV supersonic jet impingement and resulting pressure and heat transfer rate distributions [3].

Chapter 3

DESCRIPTION OF THE EXPERIMENT

3.1 Calspan 48-inch Hypersonic Shock Tunnel

Experimental tests for this study were conducted in the Calspan 48-inch Hypersonic Shock Tunnel (48" HST) shown schematically in Fig. 10. The 48" HST has a Mach number range from 5.5 to 18, freestream unit Reynolds number per foot from 3.5×10^3 to 5.0×10^7, and total temperature capability up to 5800°R [63]. These tunnel characteristics refer to a range of tunnel operating conditions and the reader is referred to reference 63 for specific details relating to any given test condition.

The tunnel is started by rupturing a double diaphragm. This permits the high pressure mixture of gases in the driver section to expand into the driven section. In so doing, a normal shock wave is generated which propagates through the low pressure air in the driven section. A region of high-temperature, high-pressure air is produced between the normal shock front and the gas interface (often referred to as the contact surface) between the driver and driven gas. When the primary or incident shock strikes the end of the driven section in the shock tube, it is reflected, leaving a region of almost stationary high-pressure heated air. This air is then expanded through a contoured converging-diverging nozzle to the desired freestream conditions in the test section.

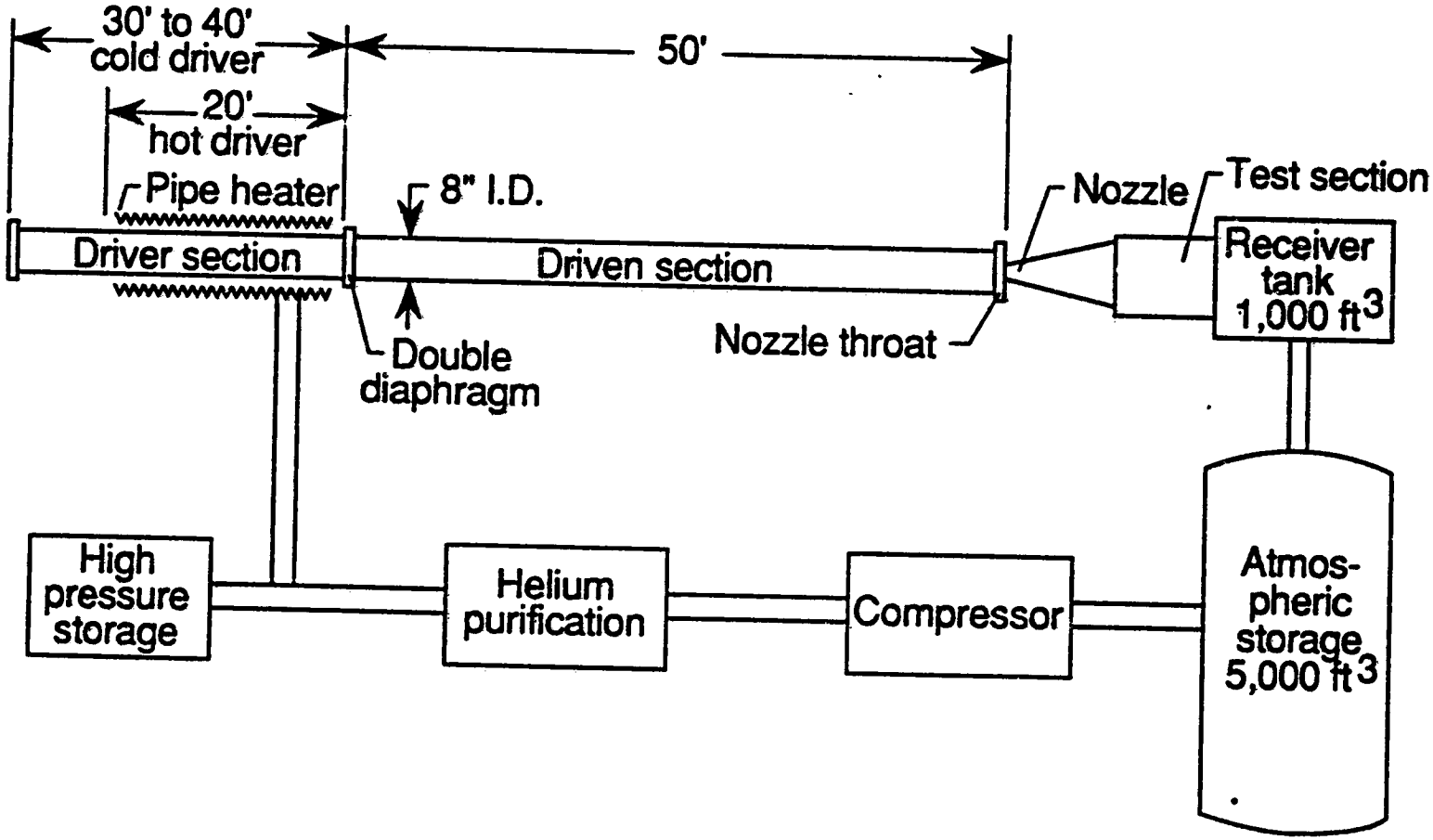

Fig. 10. Basic components of the Calspan 48-inch Hypersonic Shock Tunnel.

Test operation time is controlled by the interactions between the reflected shock wave, the gas interface, and the leading expansion wave generated by the non-stationary expansion process in the driver section. The duration of the flow in the test section varies from 5 to 20 milliseconds depending on the operating conditions. Test section Mach number is varied by changing either the nozzle throat diameter or nozzle, or both.

Two driver configurations were used for the tests presented in this study. Wieting and Holden [10] used a heated driver section in their earlier study, and some of these tests (test runs 21, 25, 26, and 31) are included in this study as baseline 0° swept results to evaluate the effect of sweep. However, the majority of the tests presented in this study were made with a longer, but unheated, driver section to increase the tunnel run time to about 20 milliseconds.

3.2 Tunnel Freestream Test Conditions

Air was used as the test medium for this experimental study. Nominal conditions of the freestream flow in the test section were at a Mach number of 8, unit Reynolds number of 1.5×10^6 per foot, dynamic pressure of 800 psf, and total temperature of 2800°R for most test runs. However, several tests were conducted at off nominal conditions to evaluate the effect of variable Reynolds number on shock wave interference. Tunnel test conditions for the test runs of this study are given in Table 1.

The freestream flow conditions presented in Table 1 were derived from the measured temperature and pressure of the driver and driven gases assuming an equilibrium isentropic flow through the nozzle. The pressure ratio of the primary shock that propagates through the shock tube was taken as the initial

Table 1 Tunnel test conditions

Run	M_1	p_1 psia	ρ_1 lb_m/ft^3 x103	T_1 °R	U_1 ft/sec	Re_1 1/ft x10-6	H_T $(ft/sec)^2$ x10-6	p_T psia	T_T °R
21	8.035	.1274	1.566	219.8	5841	1.564	18.36	1446	2790
25	8.049	.1249	1.536	219.6	5849	1.538	18.41	1435	2799
26	8.034	.1251	1.500	225.1	5911	1.482	18.81	1430	2853
31	8.033	.1260	1.513	224.8	5907	1.497	18.78	1440	2849
59	8.036	.1185	1.441	222.0	5872	1.433	18.55	1352	2819
60	8.039	.1172	1.446	218.9	5832	1.448	18.31	1335	2785
61	8.049	.1169	1.449	217.8	5826	1.456	18.26	1341	2780
66	7.943	.0645	0.735	237.1	5998	0.702	19.39	702	2941
67	8.027	.1264	1.506	226.5	5924	1.484	18.89	1440	2864
68	8.049	.1156	1.452	214.8	5785	1.469	18.01	1320	2744
69	8.041	.1248	1.511	223.0	5888	1.501	18.66	1432	2833
70	8.043	.1221	1.480	222.8	5887	1.471	18.65	1403	2833
71	8.050	.1118	1.374	219.6	5850	1.376	18.41	1288	2803
72	8.063	.1607	1.900	228.3	5975	1.874	19.21	1875	2905
73	7.965	.0602	0.725	224.3	5850	0.712	18.44	656	2809
74	8.045	.1166	1.433	219.6	5847	1.434	18.40	1337	2799
75	8.041	.1233	1.491	223.4	5894	1.480	18.69	1416	2839
76	8.034	.1211	1.465	223.2	5886	1.454	18.65	1382	2831
77	8.040	.1237	1.526	218.9	5834	1.528	18.32	1410	2785
78	8.033	.1227	1.493	222.0	5870	1.484	18.54	1396	2816
79	8.049	.1564	1.856	227.5	5954	1.830	19.07	1802	2885
80	7.991	.0561	0.710	213.4	5725	0.715	17.65	616	2702
81	8.041	.1231	1.488	223.4	5894	1.477	18.69	1413	2839
98	8.031	.1195	1.468	219.7	5838	1.467	18.34	1353	2788

pressure ratio of driver to driven gas. The total enthalpy of the reservoir or stagnation condition was calculated from the primary shock pressure ratio and initial gas temperature in the driver and driven sections. An isentropic expansion from the reservoir, through the contoured nozzle, to thermodynamic equilibrium in the tunnel test section was assumed. The freestream conditions were obtained by matching the air reservoir total enthalpy with the total enthalpy of the freestream air. The total pressure of the reservoir was also measured by four 6000 psi pressure transducers in the reservoir region prior to flow expansion through the nozzle. The pressure transducers were Calspan designed four-arm active bridge gauges [63]. A complete discussion of the assumptions used to determine the freestream test conditions in the Calspan Hypersonic Shock Tunnels are given in reference 63.

3.3 Test Model Configuration

The model used in this interference study was sting mounted in the tunnel test section and consisted of a three-inch diameter, 18-inch long cylinder and three interchangeable incident shock generators swept at 0°, 15°, and 30°. The shock generators were 18 inches wide and about 26 inches long. The cylinder used in the present study was used by Wieting and Holden for two-dimensional interference studies [9-12]. However, the cylinder support arms and shock generator were redesigned, allowing the cylinder and incident shock generator to be swept at the appropriate angles. A photograph of the 0° swept model is shown in Fig. 11; and a schematic of the model in the swept condition is shown in Fig. 12. The dashed line in Fig. 12 represents a reference plane in which the tunnel freestream flow is in the z direction. The shock generator leading edge lies in the reference plane and has a sweep

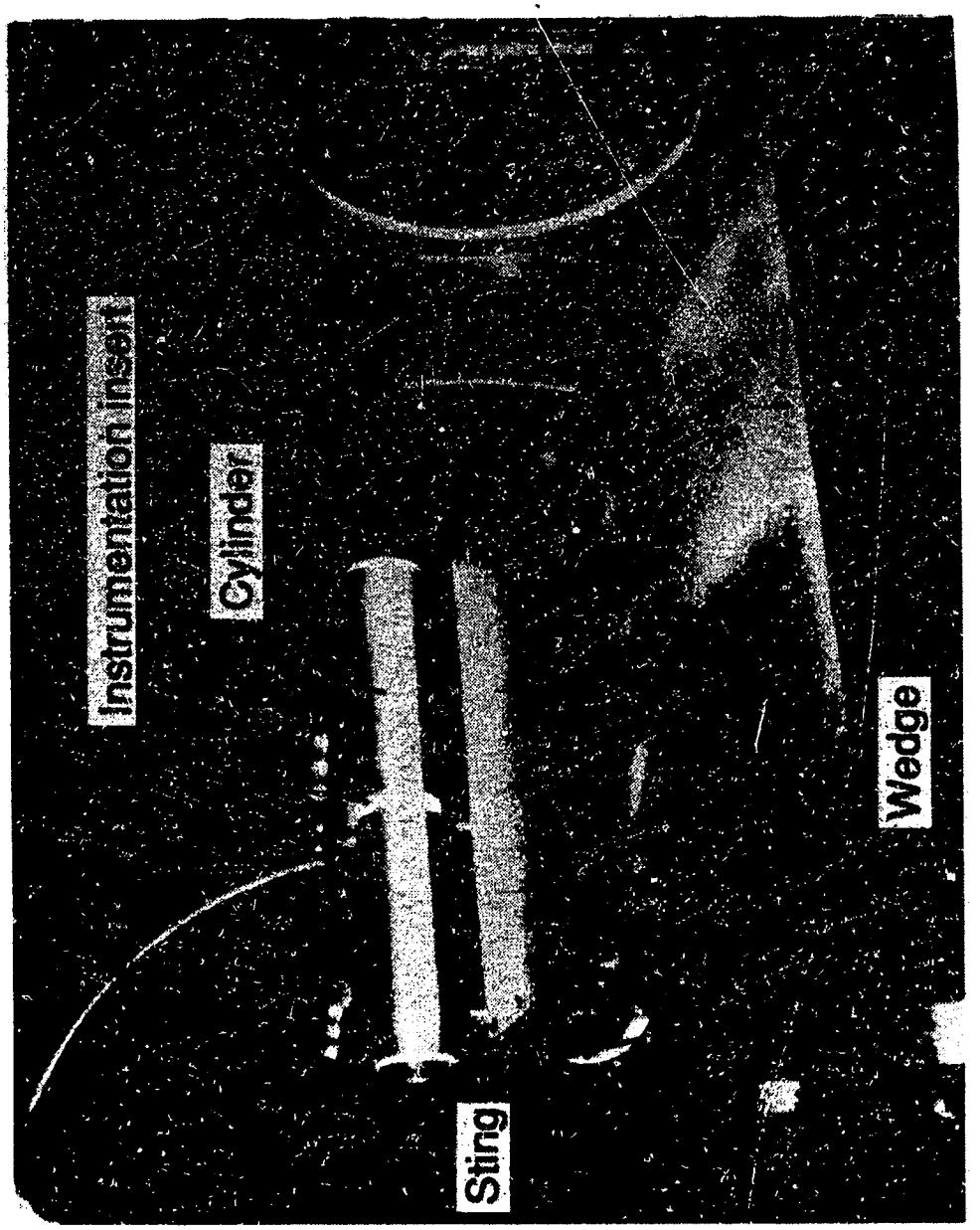

Fig. 11. The 0° swept shock wave interference model in the Calspan 48-inch Hypersonic Shock Tunnel.

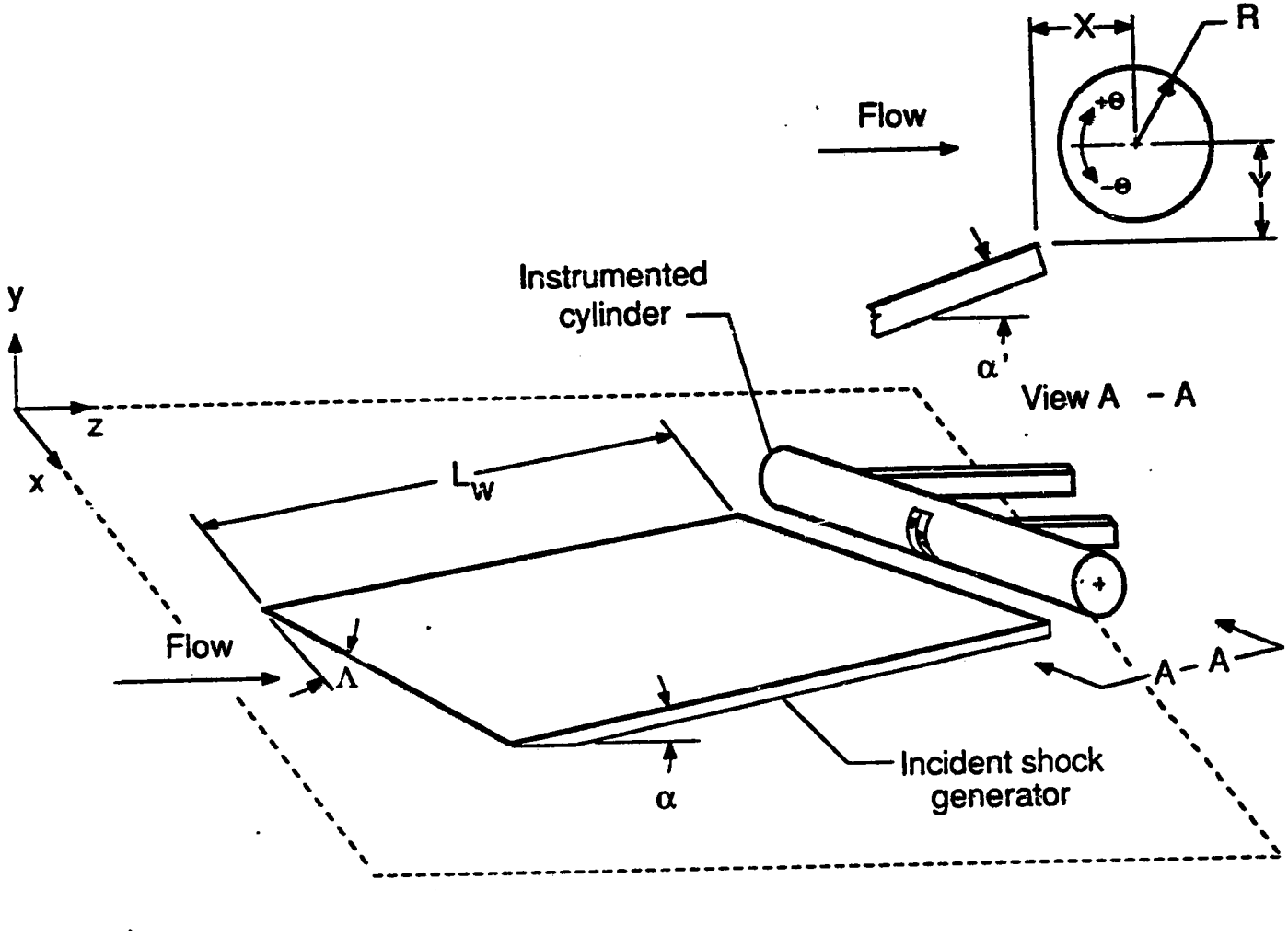

Fig. 12. Schematic diagram of the swept shock wave interference model.

angle, designated as Λ, relative to the x direction on the reference plane. The generator sides are aligned with the direction of flow and are inclined at an angle, α, relative to the z coordinate direction. The cylinder is parallel to the trailing edge of the shock wave generator which is parallel to its leading edge, hence the cylinder is also swept at the angle Λ.

The model design allowed horizontal and vertical positioning of the cylinder with respect to the shock generator. This allowed vertical movement of the incident shock on the cylinder bow shock so that various shock wave interference patterns could be investigated. Coordinates for the cylinder position for each test run are given in Table 2. Cylinder position (X,Y) was measured with respect to the trailing edge of the shock generator as shown in View A-A in the upper right of Fig. 12. Also, shock generator angle-of-attack, α; sweep angle, Λ; and shock generator wedge length for each test run are given in Table 2. The cylinder was heavily instrumented and was rotated about its axis to place densely spaced instrumentation in the interference impingement zone, corresponding to the location of highest pressure and heat transfer rates. A planform schematic of the cylinder instrumentation insert is shown in Fig. 13.

3.4 Test Model Instrumentation and Data Reduction

The interference model cylinder was instrumented with 24 high frequency quartz pressure transducers (Kulite model XCQ- and XCW-062 series differential gauges) and 32 thin-film platinum thermometers. Instrumentation was densely spaced in the surface interaction region. The natural frequency of the pressure transducers was at least 150KHz. A calibration of the gauges showed a maximum deviation of less than ± 0.5 percent of the full scale

Table 2 Model dimensions

Run	X in	Y in	α deg	Λ deg	Lw in
21	2.09	2.89	12.5	0	26.5
25	2.13	3.36	12.5	0	26.5
26	2.13	3.36	12.5	0	26.5
31	----	----	----	0	----
59	1.91	2.83	12.5	0	26.5
60	3.31	3.19	12.5	0	26.5
61	1.85	3.08	12.5	0	26.5
66	3.31	3.19	12.5	15	26.5
67	3.31	3.19	12.5	15	26.5
68	2.93	3.43	12.5	15	26.5
69	2.93	3.63	12.5	15	26.5
70	1.17	3.63	12.5	15	26.5
71	1.17	3.31	12.5	15	26.5
72	1.17	3.31	12.5	15	26.5
73	1.17	3.31	12.5	15	26.5
74	----	----	----	15	----
75	2.84	3.44	12.5	30	26.0
76	2.84	3.09	12.5	30	26.0
77	1.25	3.44	12.5	30	26.0
78	2.84	3.24	12.5	30	26.0
79	2.84	3.44	12.5	30	26.0
80	2.84	3.44	12.5	30	26.0
81	----	----	----	30	----
98	2.72	3.41	12.5	30	26.0

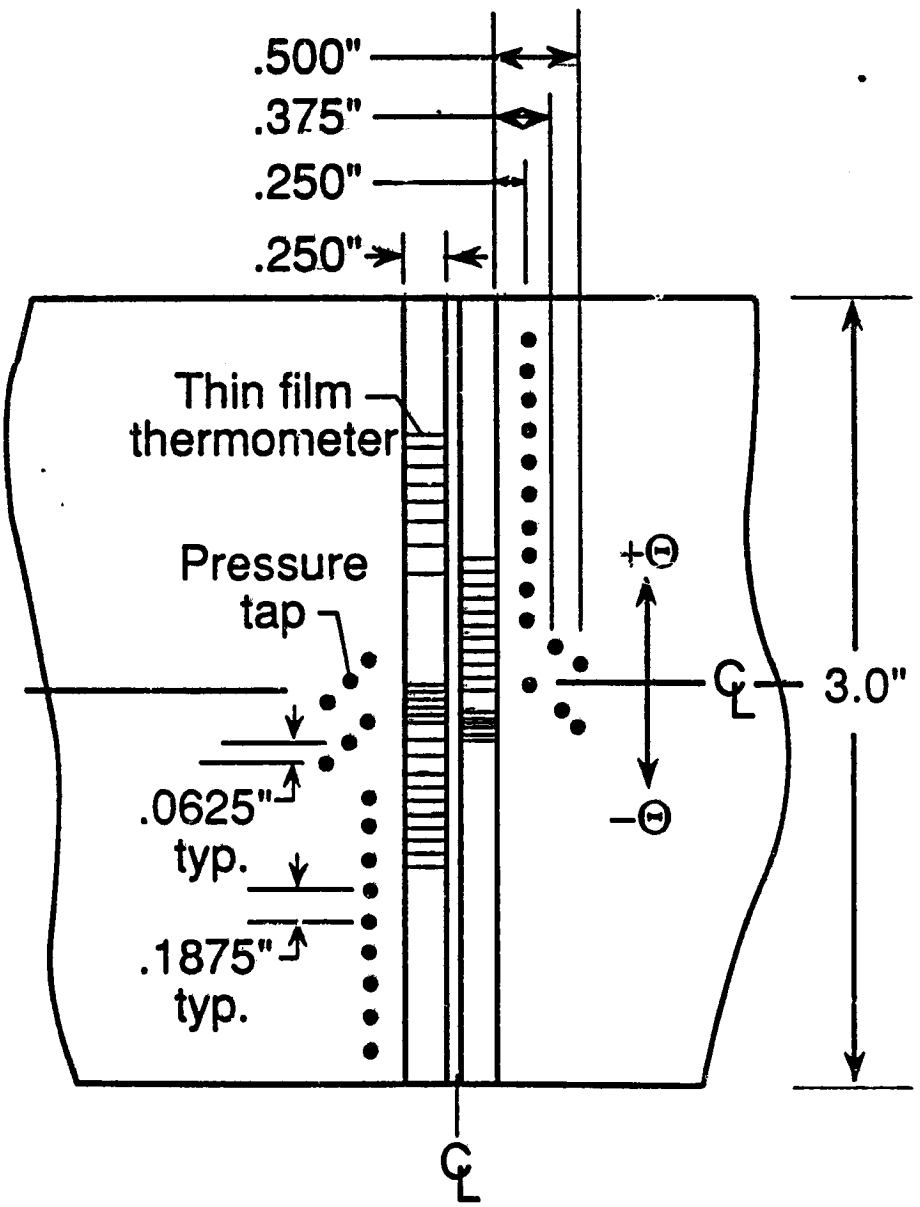

Fig. 13. Planform schematic of the instrumentation layout for the cylinder.

reading. The thin-film platinum thermometers were custom designed and built by Calspan and had a response time on the order of 10^{-7} seconds [64]. The resistance of the thin-film thermometers was linear to ± 0.1 percent over the range of temperature measurements. Although the cylinder was the same one used by Wieting and Holden [9-12], cylinder thin-film thermometer instrumentation was replaced after their experiments.

The pressure transducers were flush mounted on the cylinder surface and had orifices which were 0.0625 inches in diameter with a thin screen to protect the sensors. Circumferential spacing of the pressure transducers varied from 0.0625 inches (2.39°) in the "interaction region" to 0.1875 inches (7.16°) on either side of this region. Pressure transducer spacing was limited by the physical size of the gauges and by the internal volume of the test cylinder.

The 0.010-inch wide thin-film platinum thermometers were spaced 0.021 inches (0.80°) in the "interaction region" and 0.080 inches (3.06°) elsewhere. The thin-film thermometers were painted (≈ 1000 Å thick) on the surface of a cylindrical shaped pyrex substrate that was flush-mounted to the cylinder surface. A coating of magnesium fluoride (≈ 1200 Å thick) was vapor deposited over the gauge to protect the platinum element against abrasion [64]. The number of surface temperature sensors was limited by the available input channels to the data acquisition system.

Voltage outputs from the pressure transducers and thin-film thermometers were recorded in digital form during the 15 millisecond test time of the 48" HST with a 50 microsecond sampling interval. The overall data recording system accuracy has been shown to be within one percent. These digital data were reduced to engineering units using normal conversion methods. Heat transfer rates were reduced from the temperature-time history of the thin-film thermometers using Calspan data reduction software that accounted for

variable thermal properties of the pyrex substrate [65]. This numerical heat transfer rate data reduction technique employed a Crank-Nicolson method of solution [66] for a semi-infinite slab with temperature dependent properties [64,67]. The surface heat transfer rates were treated as a series of step impulses rather than a constant. During Type IV supersonic jet impingement tests this was important because some of the measured surface temperatures in the impingement region increased to over 1000°R. However, the thin-film gauge substrate was made from a very low conductivity pyrex glass which reduced circumferential heat conduction. Wieting showed that the thermal properties of the pyrex limited heat conduction in the circumferential direction to less than five percent of the peak in the high temperature gradient region [9]. Details of the method used to calculate the heat transfer rates are developed in Appendix A.

Also, the experimental heat transfer rates presented in this study have been adjusted to a cold wall temperature (530°R) since the heat transfer rates were calculated at the hot wall temperature by the Calspan data reduction methods. This adjustment of the heat transfer rates was made using :

$$q = \frac{T_{aw} - T_{cw}}{T_{aw} - T_{hw}} q_{hw} \qquad (4)$$

which assumes a constant heat transfer coefficient from the hot wall to the cold wall temperature.

Oscillation in the pressure and heat transfer rate peaks occurred during the tests of the Type iV supersonic jet impingement. Close inspection of the time history data indicated a slight motion of the supersonic jet on the cylinder surface. The shape of the pressure and heat transfer rate distributions on the cylinder surface remained essentially unchanged, but the location of the peak

changed slightly (less than 2°). Therefore, the present results were taken over a time interval where the peak of the pressure and heat transfer rate distributions had reached a maximum value and was well established.

All experimental data presented in this study were normalized by calculated stagnation line values at the appropriate freestream conditions and sweep angle of the corresponding tunnel test. This allowed the experimental data to be evaluated with an undisturbed theoretical level at the same sweep angle. Therefore, sweep angle dependence is separated from the presented results which would be present if all experimental data were normalized by a 0° undisturbed stagnation point level. The stagnation pressures were calculated using an equilibrium chemically reacting gas model for air [68] from the freestream test conditions and freestream velocity component normal to the cylinder axis. The stagnation heat transfer rates were calculated using the method of Fay and Riddell [60] for two-dimensional stagnation point heating at the cold wall temperature. Two-dimensional heat transfer rates were adjusted to the tested sweep angle using the empirical $\cos^{1.1}\Lambda$ function that is given by Beckwith and Gallagher [24]. The thermodynamic properties for the heat transfer rate calculations were computed by the equilibrium gas model of Prabhu and Erickson [68].

3.5 Flowfield Uniformity on the Cylinder

Flow on the incident shock generator is uniform inside the regions enclosed by the characteristic lines [9] shown by dashed lines in Fig. 14 for the three sweep angles. Nonuniform flow outside these regions is caused by disturbances from the sides of the shock generator. The disturbances start propagating from the ends of the shock generator leading edge at the local

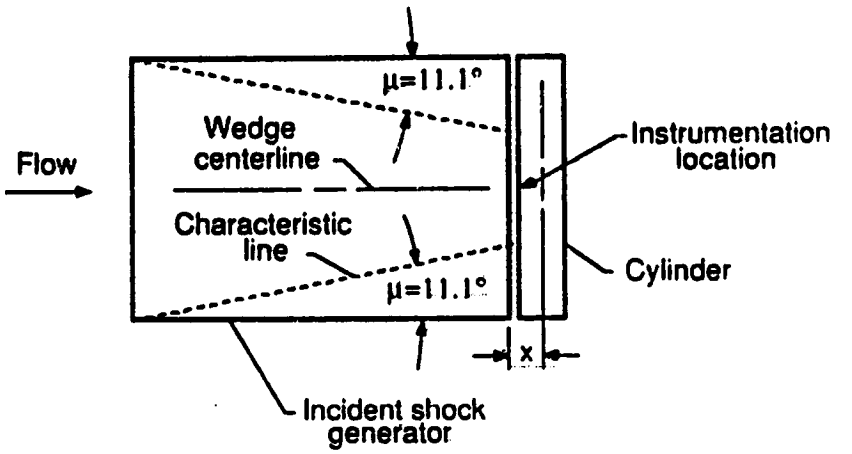

a) Sweep angle, Λ=0°

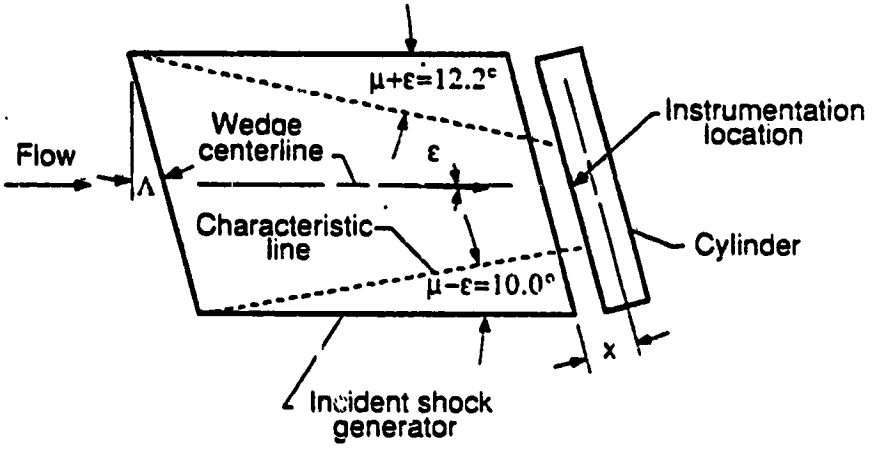

b) Sweep angle, Λ=15°

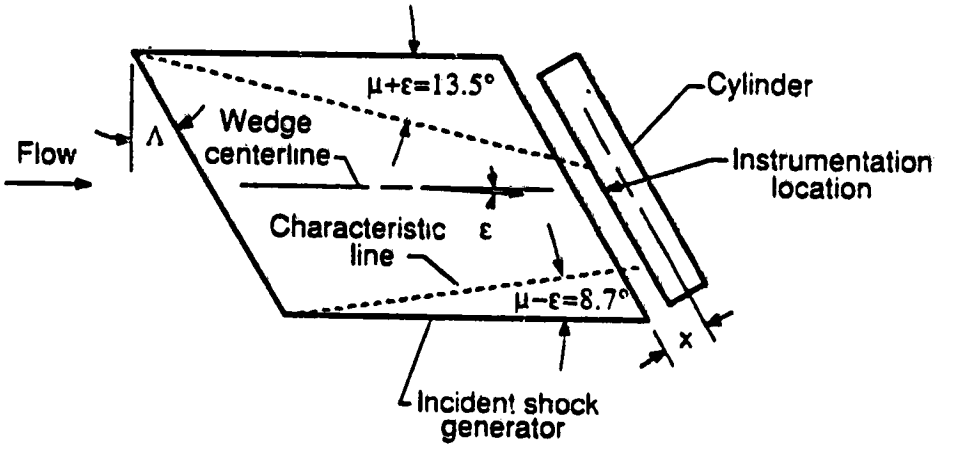

c) Sweep angle, Λ=30°

Fig. 14. Planform schematic of the shock wave interference model showing the region of uniform flow.

wedge Mach number wave angle, $\mu = \arcsin(1/M)$. The wedge Mach number is approximately 5.2 for all three sweep angles; therefore, the angle of the characteristic line on the wedge is 11.1° with respect to the local flow direction on the wedge.

For the 0° swept wedge, the characteristic lines are at 11.1° as shown in Fig. 14(a). However, for the 15° and 30° swept tests, the freestream flow passes through a swept oblique shock wave and is turned a small angle, ε, from the freestream flow direction as shown in Figs. 14(b) and 14(c). For the test freestream flow condition, wedge deflection angle, and sweep angles of 15° and 30°, ε equals 1.1° and 2.4°, respectively. The characteristic lines shown in Figs. 14(b) and 14(c) include the additional turning from this effect.

Flow between the cylinder ends and the cylinder intersection with the characteristic lines was influenced by nonuniform wedge flow. However, the middle region of the cylinder (area bounded by the characteristic lines) was exposed to about 7.5 inches of uniform wedge flow. The cylinder instrumentation was located along the wedge centerline in this region as shown in Fig. 14, and the instrumentation was at least about two inches from the intersecting characteristic line. Therefore, the wedge flowfield involved in the shock wave interference is assumed to be uniform in the instrumentation region on the cylinder for the three sweep angles.

End effects from the most forward end of the swept cylinder cause the bow shock to curve with respect to the cylinder axis which affects the local spanwise flow on the cylinder. Lamb and Stallings [69] presented schlieren photographs of a 0.013 scale model of the shuttle solid rocket booster at Mach number 3.7 and 30° sweep which showed this bow shock curvature end effect. The bow shock was nearly parallel with the booster axis about two diameters downstream from the booster rocket nose. Uniform spanwise flow occurs

downstream of the point where the bow shock is parallel with the cylindrical body axis because the local cylinder flow is affected by a uniform bow shock. Extending these observations [69] to the present Mach 8 study, spanwise flow on the 30° swept cylinder should be uniform about two cylinder diameters or six inches downstream from the forward most end of the cylinder. As the sweep angle is decreased, the flow should become uniform sooner.

Cylinder end effects were shown by Thareja, et al [19] in a numerical study of a 15° swept Type III interference flowfield, using the present data for comparison. The flowfield was calculated using an inviscid, three-dimensional finite element computer program [19]. Their results showed that the cylinder bow shock was nearly parallel with the cylinder axis about two diameters downstream of the cylinder forward end [19]. These results are similar to the undisturbed 30° swept results presented by Lamb and Stallings [68]. Therefore, it is assumed the interference flowfield for the present 15° and 30° swept tests was free from cylinder end effects about three inches upstream of the instrumentation location. At 0° sweep, the cylinder is perpendicular to the incoming flow, therefore, no cylinder end effects were present at the instrumentation location as shown by Wieting [9].

Chapter 4

SWEPT SHOCK WAVE INTERFERENCE TEST RESULTS AND DISCUSSION

Experimental results for the shock wave interference model at the three sweep angles with an undisturbed flowfield are given in section 4.1. Results for the 0°, 15° and 30° swept tests with an interference flowfield are presented in sections 4.2, 4.3 and 4.4, respectively. The experimental data were normalized with respect to calculated stagnation line values for the corresponding test freestream conditions (and sweep angle). The reference data are given in Table 1. The method used to calculate the stagnation line values was discussed previously in section 3.4. Experimental results and stagnation line values for each test run are tabulated in Appendix B. The experimental results include pressures, heat transfer rates, and their angular positions around the instrumented cylinder as shown in View A-A in the upper right of Fig. 12. Also, the thin-film gauge temperatures that correspond to the calculated hot-wall heat transfer rates are tabulated in Appendix B.

Schlieren photographs of the shock wave interference pattern and the pressure and heat transfer rate distributions on the instrumented cylinder are given for the 0° swept model tests. The 15° and 30° swept model results do not include the schlieren photographs because facility window limitations of the 48" HST prevented schlieren line of sight along the cylinder axis. Theoretical undisturbed pressure and heat transfer rate distributions are

included on all distribution plots presented in this chapter. The experimental pressure distributions are compared with the modified Newtonian distribution [24]; and experimental heat transfer rates are compared with laminar and turbulent heat transfer rate distributions given by Beckwith and Gallagher [24]. The modified Newtonian pressure distribution was used in the calculation of the theoretical heat transfer rate distributions. Turbulent heat transfer rate distributions are not given for the 0° swept results because the theoretical distribution requires a spanwise velocity component in the calculation [24] which was not present for 0° sweep angle.

Previously published results from an experimental shock wave interference study [10] are included in this study as 0° swept model results (test runs 21, 25, 26, and 31). The experimental heat transfer rates [10] were normalized previously by the experimental undisturbed stagnation point value. However, in this study, these heat transfer rates have been normalized by the two-dimensional theoretical Fay and Riddell [60] stagnation point heat transfer rates. Also, these data have since been corrected by Wieting and Holden to account for temperature dependency of the pyrex substrate material properties by the procedure discussed in Appendix A. The 0° swept model results are important because they provide a baseline condition to compare with model results at 15° and 30° sweep.

4.1 Undisturbed Flowfield for 0°, 15°, and 30° Swept Cylinder

To access the effects of the various shock wave interference patterns, baseline data were obtained on the cylinder for flow without an impinging oblique shock wave. The baseline or "undisturbed flow" data were obtained at the same freestream flow conditions as the shock interference tests and at

sweep angles of 0°, 15°, and 30°. A schlieren photograph of the undisturbed flowfield for the 0° swept model is shown in Fig. 15(a). Pressure and heat transfer rate distributions for the 0°, 15°, and 30° swept model configurations with an undisturbed flowfield are shown in Figs. 15, 16, and 17, respectively.

The experimental surface pressure distributions are compared with the modified Newtonian pressure distribution in Figs. 15(b), 16(a), and 17(a) for the 0°, 15°, and 30° swept model tests, respectively. These figures show a good agreement between the experimental and theoretical pressure distributions at the three sweep angles.

The experimental heat transfer rate distribution for the 0° swept model in an undisturbed flowfield is shown in Fig. 15(c) and compared with a theoretical laminar heat transfer rate distribution [24]. The experimental heat transfer rate at the stagnation point is almost 50 percent higher than that predicted by Fay and Riddell [60] for the stagnation point. The cause of this discrepancy has not been determined fully. However, the increased heat transfer rate may be attributed to either an unclean freestream flowfield that allowed particle impingement on the cylinder surface or on freestream turbulence effects, or a combination of both effects.

A comparison of the experimental heat transfer rate distribution with the theoretical laminar and turbulent distributions [24] for the 15° swept test is shown in Fig. 16(b). The experimental and laminar distributions are in good agreement. Therefore, the 15° swept heat transfer rate data in an undisturbed flowfield provide a firm basis for assessing the effect of shock wave interference heating.

Heat transfer rate distributions for the 30° swept model test are shown in Fig. 17(b). For this test, the experimental heat transfer rates are between the laminar and turbulent theory over a major portion of the windward surface of

a) Schlieren photograph

Fig. 15. Experimental results for 0° swept undisturbed flowfield (run 31).

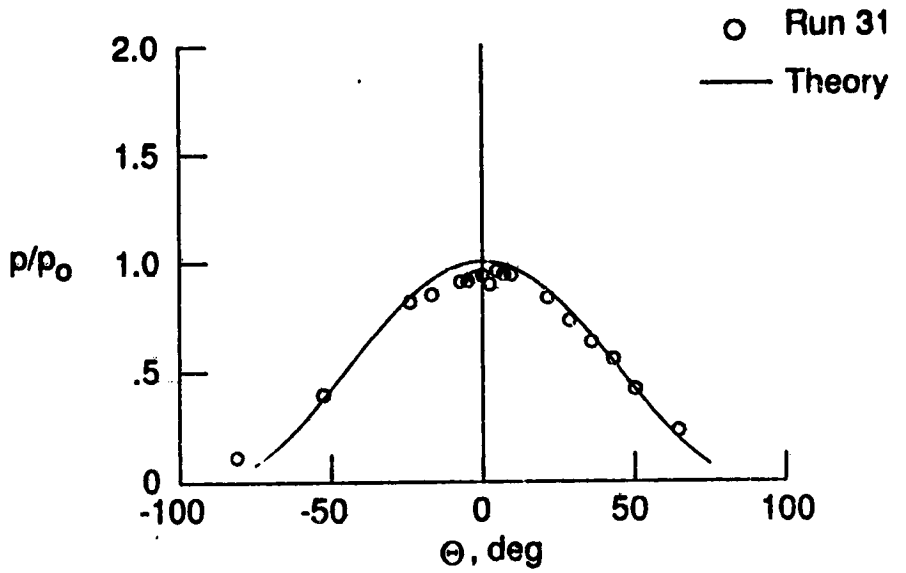

b) Pressure distribution

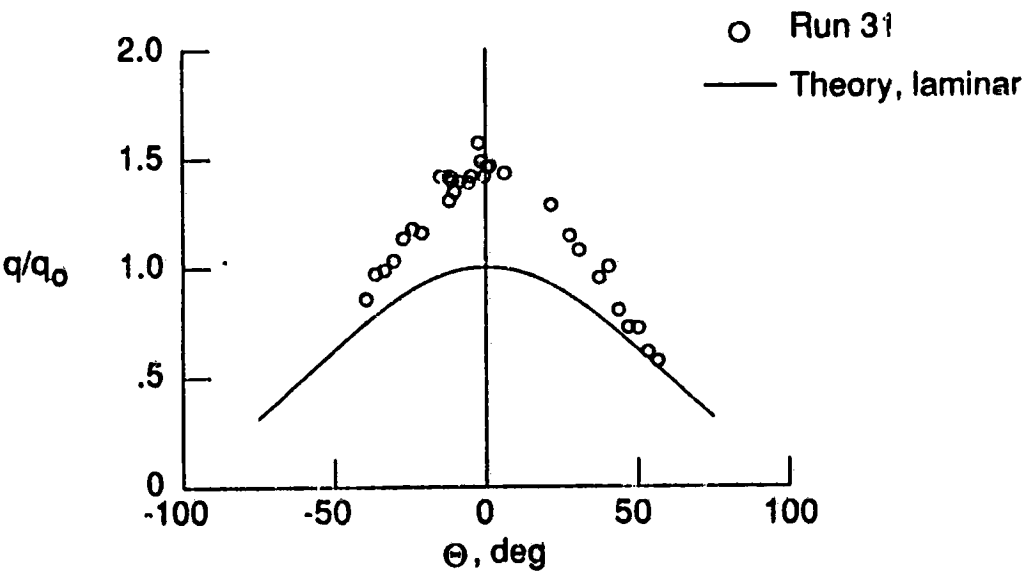

c) Heat transfer rate distribution

Fig. 15. Concluded.

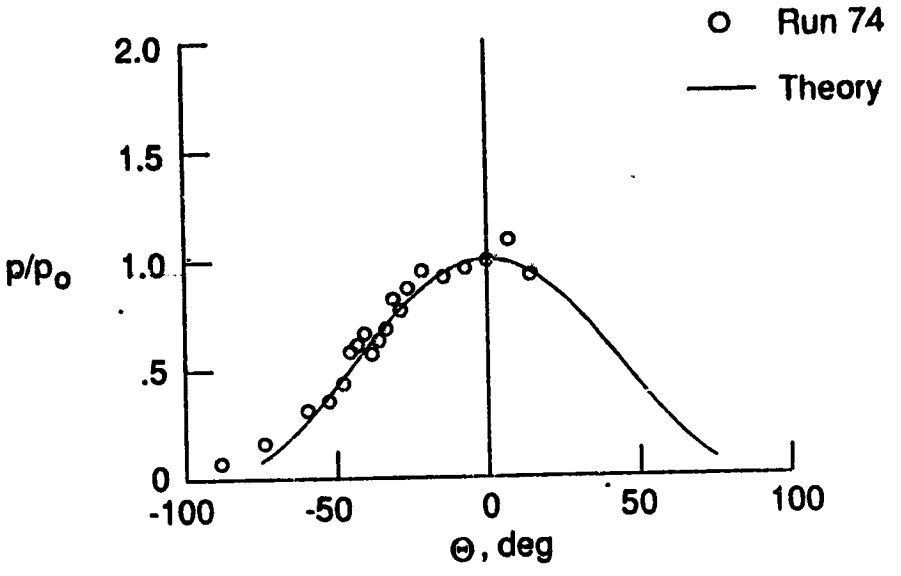

a) Pressure distribution

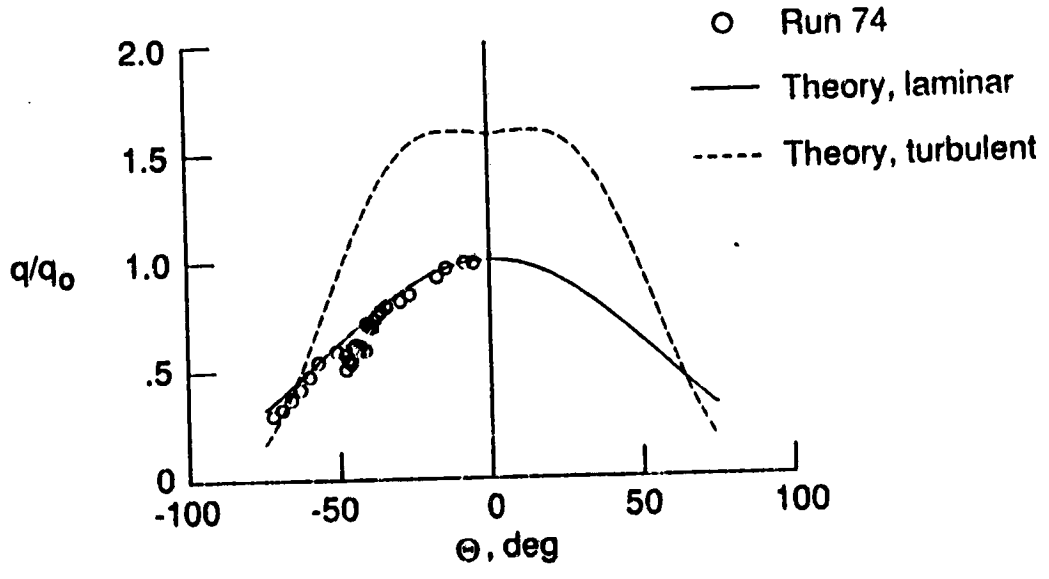

b) Heat transfer rate distribution

Fig. 16. Experimental results for 15° swept undisturbed flowfield (run 74).

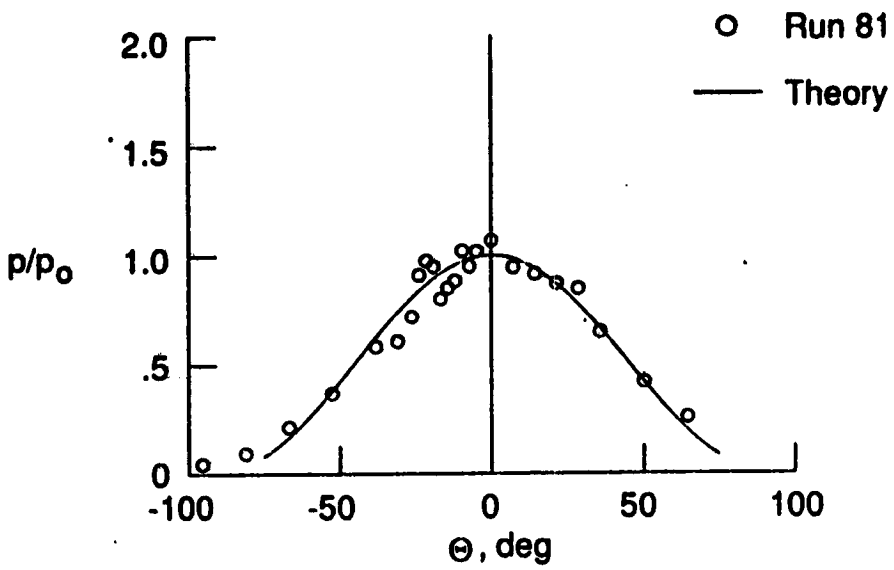

a) Pressure distribution

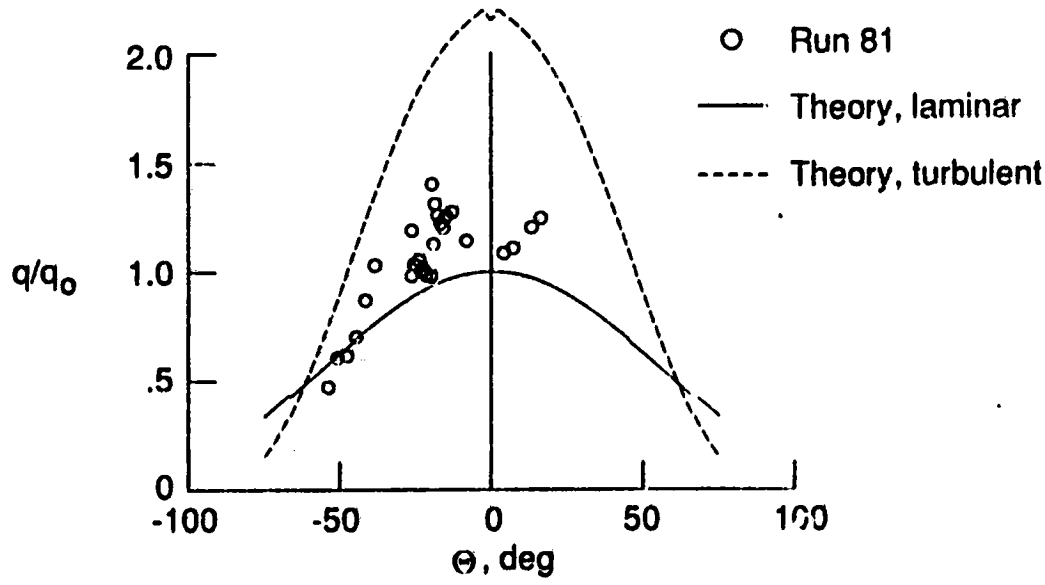

b) Heat transfer rate distribution

Fig. 17. Experimental results for 30° swept undisturbed flowfield (run 81).

the instrumented cylinder. The heat transfer rate is close to the laminar level at the stagnation line ($\Theta = 0°$). However, the heat transfer rate distribution increases to a maximum at $\Theta \approx \pm 25°$. Then, the local heat transfer rate distribution decreases and follows the trend of the theoretical turbulent distribution. Therefore, heating at the stagnation line on the cylinder is laminar and becomes turbulent as the flow moves around the cylinder.

In general, pressure distributions agree with the modified Newtonian theory for the tests in the undisturbed flowfield. Therefore, all experimental pressures were normalized by the calculated stagnation line pressure of the corresponding sweep angle and freestream flow test condition.

Heating on the 15° swept model agrees with the laminar theory; and for the 30° swept test, heating is laminar at the stagnation line. The experimental heat transfer rate distributions for the 15° and 30° swept tests are consistent with results given by Beckwith and Gallagher [24]. However, the 0° swept heat transfer rate distribution is inconsistent and may be caused by freestream flow contamination or freestream turbulence as explained above. Because of this inconsistency and the agreement with the laminar prediction at the stagnation line for the 15° and 30° swept tests, the shock wave interference heat transfer rates were normalized with the theoretical laminar undisturbed stagnation line values.

4.2 0° Swept Interference Results

Experimental results for the 0° swept model tests with Type III and Type IV shock wave interference flowfields are presented in this section. Theoretical peak pressures and heat transfer rates were predicted by a computer program

for these model tests and are shown on the pressure and heat transfer rate distribution plots.

The computer program that was used is similar to a program developed by Morris and Keyes [42]. However, the present program has the option to assume air behaves as a calorically perfect gas or to assume air is a mixture of 11 chemically reacting species (O_2, N_2, O, NO, N, NO^+, e^-, N^+, O^+, Ar, and Ar^+) in thermodynamic equilibrium. A chemically reacting mixture accounts for the temperature and pressure dependence of the translational, rotational, and vibrational internal energy modes, and at high temperatures, dissociation and ionization of the constituents of air. For chemically reacting air, specific heats are a function of temperature and pressure. Therefore, all air calculations in the program were made with an 11-species equilibrium chemically reacting gas model for air [68] that is applicable to temperatures up to 15 000 K. The computer program is called "EASI" which is an acronym for Equilibrium Air Shock Interference.

The required variable inputs to the EASI program for the Type III shock wave interference predictions were freestream flow conditions, transmitted shock length, L_{ts}, shown in Fig. 4(a), and the flow turning angle of region 5 with respect to the freestream direction. For the Type IV predictions, the required inputs were freestream flow conditions and transmitted shock length, L_{ts}, as shown in Fig. 5(a). The freestream conditions were taken from Table 1, and the transmitted shock lengths which were measured from the schlieren photographs and are presented in Table 3.

4.2.1 Type III Shock Wave Interference

Heating from shear layer attachment to the wall for the Type III shock wave interference pattern is dependent on whether the shear layer is laminar or

Table 3 Geometric aspects of the 0° swept shock wave interference patterns

Run	Type	L_{ts} in	$\theta_{5,abs}$ deg	Y_{inv} in	w_j in
26	III	2.06	33.0	----	-----
25	III	1.93	33.0	----	-----
61	IV	1.35	----	0.24	0.140
21	IV	0.71	----	0.52	0.074
59	IV	0.75	----	0.52	0.077
60	IV	0.78	----	0.62	0.081

turbulent at the wall attachment point. Also, heating and pressure are dependent on the shear layer attachment angle, $\theta_{5,abs}$, at the wall. (See Fig. 4(a).) Therefore, these two effects are discussed in this section.

Edney [3] and Birch and Keyes [39] gave a transition shear layer Reynolds number criteria to determine the state of the shear layer at the wall attachment point. The criteria is based on local flow conditions in regions 2 and 4 (See Fig. 4(a).) and shear layer length at transition. Edney [3] defined the shear layer transition Reynolds number as:

$$Re_t = \frac{\rho_4 (u_4 - u_2) L_{sl}}{\mu_4} \tag{5}$$

and Birch and Keyes [39] defined the transition Reynolds number as:

$$Re_t = \frac{\rho_4 \lambda L_{sl}}{\mu_4} \tag{6}$$

where

$$\lambda = u_4 \frac{(1 - \frac{u_4}{u_2})}{(1 + \frac{u_4}{u_2})} \tag{7}$$

The difference between equations (5) and (6) is the velocity term used to calculate the shear layer transition Reynolds number. Edney suggested the transition Reynolds number was based on the velocity difference between region 2 and region 4. However, Birch and Keyes [39] suggested, as a first approximation, the transition Reynolds number was based on an average velocity between the two regions. Both Edney [3] and Birch and Keyes [39] plotted the calculated transition Reynolds number as a function of region 4 Mach number in their respective reports using various experimental results.

The shear layer Reynolds numbers for the present Type III model tests (runs 25 and 26) were calculated using equations (5) and (6) from the shear layer length and local conditions in regions 2 and 4 as determined by EASI. The shear layer Reynolds number from equation (5) is 4.3×10^5 which is greater than Edney's turbulent criteria of $Re_t = 2.7 \times 10^5$; and the shear layer Reynolds number from equation (6) is 3.8×10^5 which is greater than the Birch and Keyes criteria of $Re_t = 5.5 \times 10^4$. Both comparisons show that the present Type III shear layer Reynolds number is greater than the transition Reynolds number. Therefore, this study has concluded that the shear layer was turbulent at the wall attachment point in the present tests.

Having characterized the state of the shear layer, peak pressure and peak heat transfer rate are also dependent on the wall turning angle at the attachment point. The wall turning angle affects the shock strength between regions 4 and 5 as shown in Fig. 4(a). The turning angle at the wall determines the local pressure rise from region 4 to 5 and flow conditions in region 5. (For example, see the M_4 curve in Fig. 4(b).) Knowing the flow conditions in region 5, one can determine the peak heat transfer rate as given by equation (2).

The sensitivity of peak pressure and heat transfer rate to wall turning angle was computed using the EASI computer code and is shown in Fig. 18. The results of this analysis are normalized by the undisturbed stagnation pressure and heat transfer rate. The figure shows that peak pressure and peak heat transfer rate increase as the wall turning angle from region 4 to region 5 increases over the range of possible turning angles in the analysis.

Schlieren photographs and pressure and heat transfer rate distributions for the 0° swept Type III shock wave interference tests are shown in Figs. 19 and 20. Referring to Table 3, these results are presented for decreasing

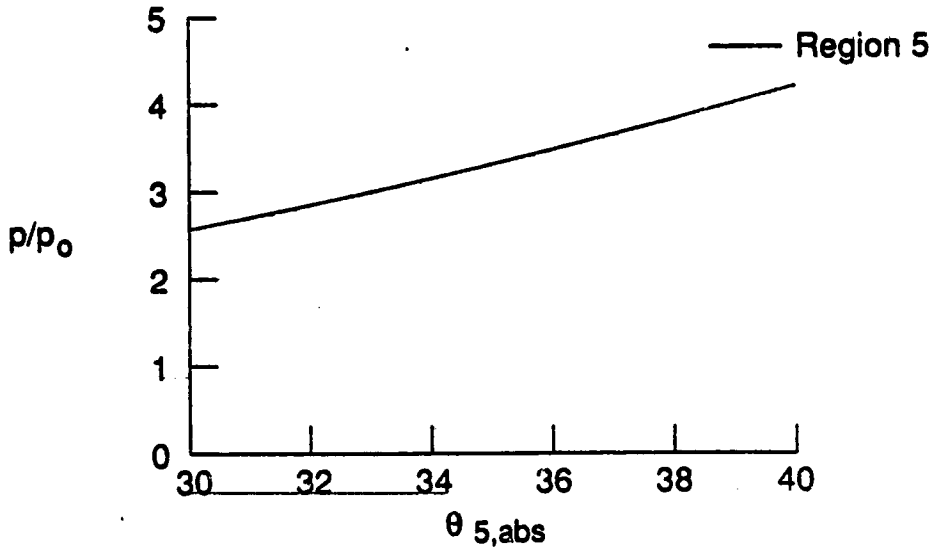

a) Pressure

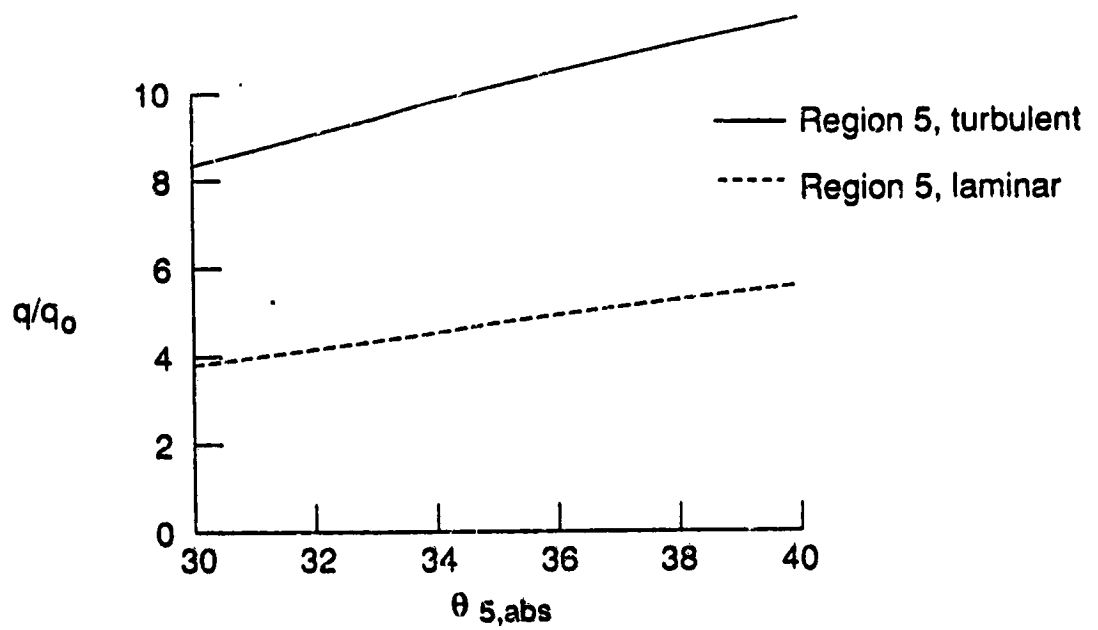

b) Heat transfer rate

Fig. 18. Type III interference peak pressure and heat transfer rate sensitivity to wall turning angle.

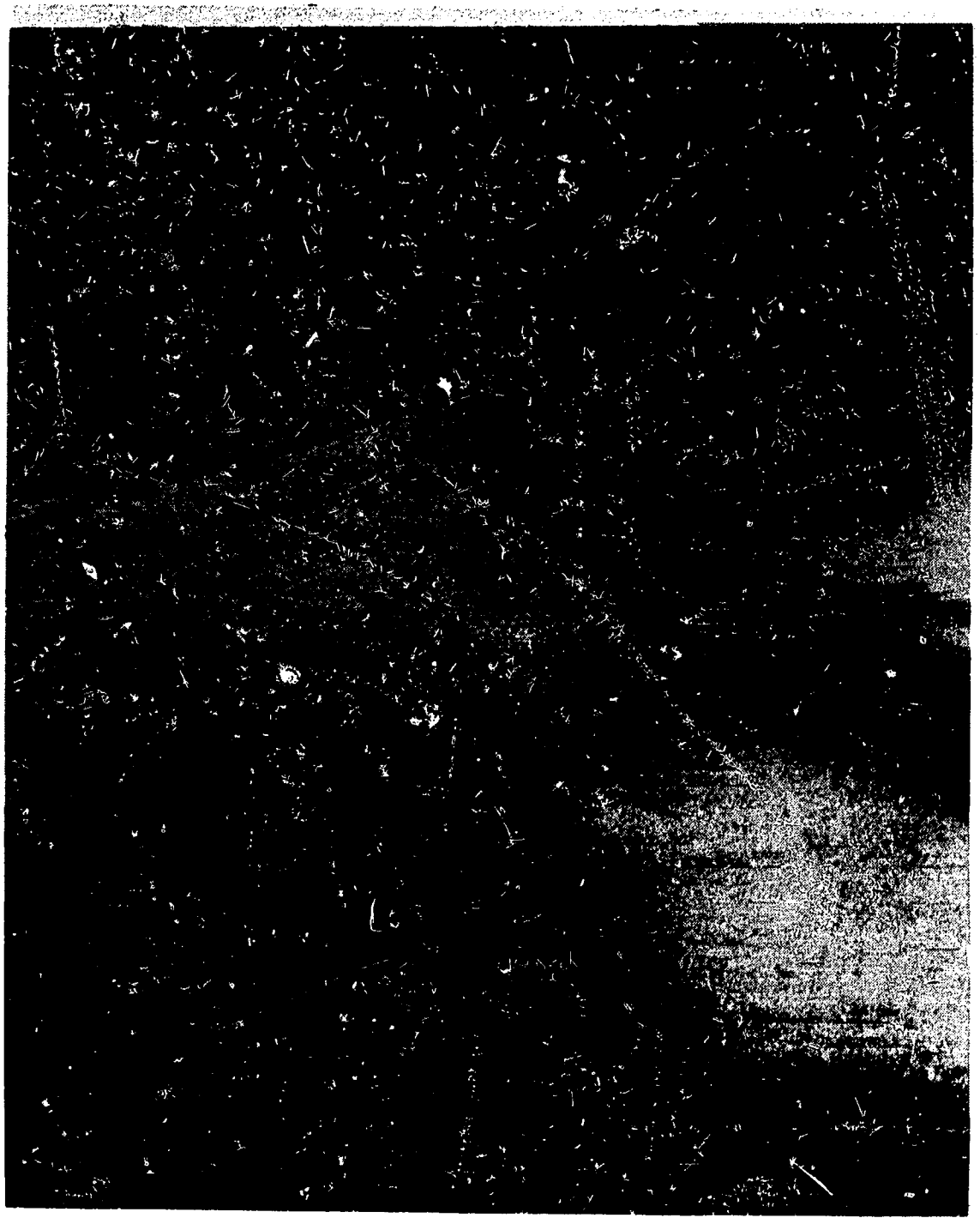

a) Schlieren photograph

Fig. 19. Experimental results for 0° swept, Type III interference flowfield (run 26, L_{ts} = 2.06 in., $Re_1 = 1.482 \times 10^6$ $^1/_{ft}$). Note location of shear layer intersection.

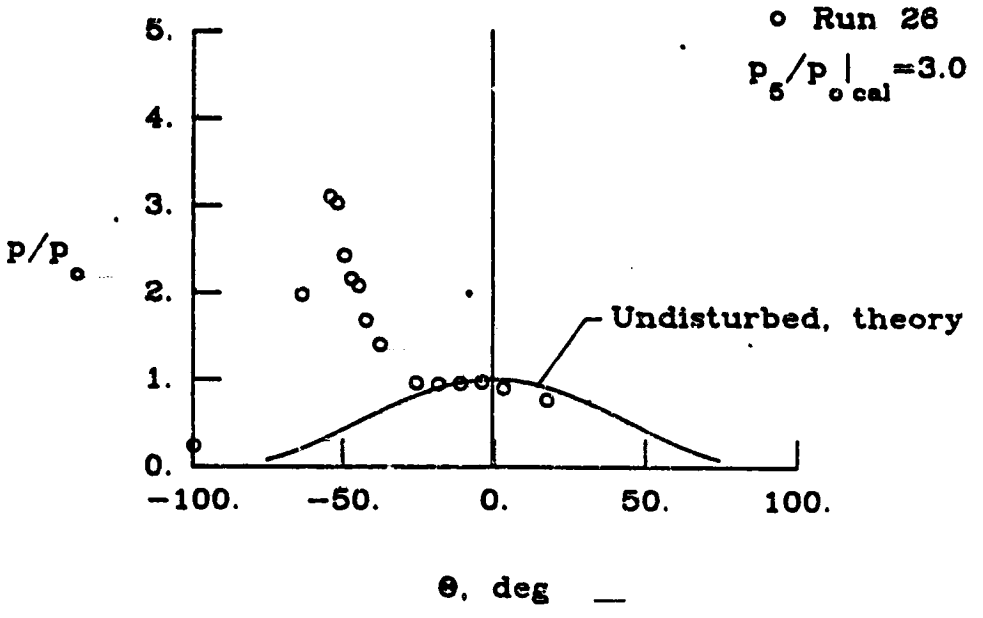

b) Measured pressure distribution compared with undisturbed theory and against maximum predicted pressure rise.

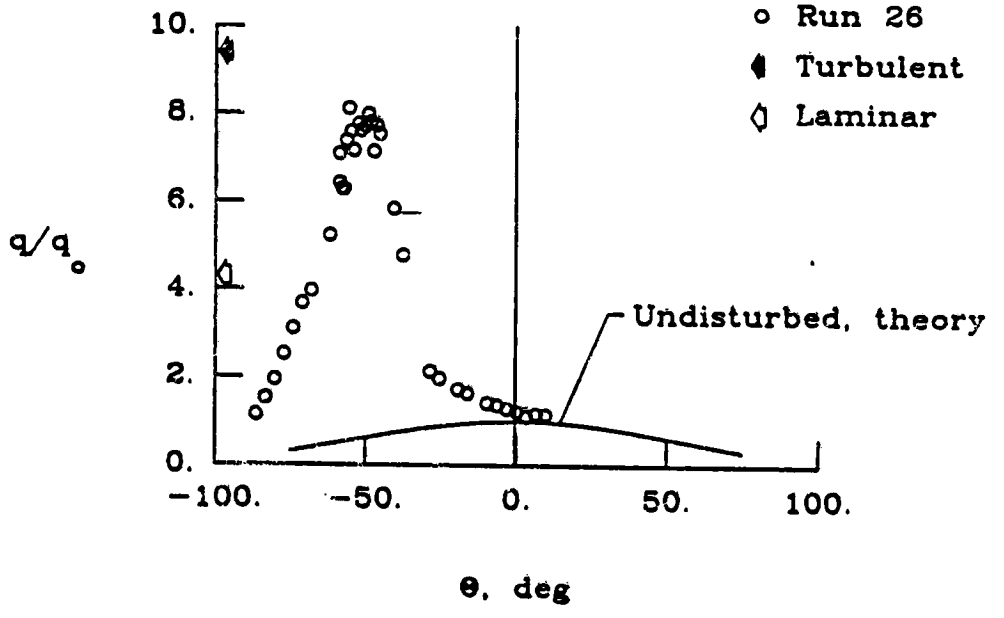

c) Measured heat transfer rate distribution compared with undisturbed theory and with estimated laminar and turbulent shear layer attachment heating levels.

Fig. 19. Concluded.

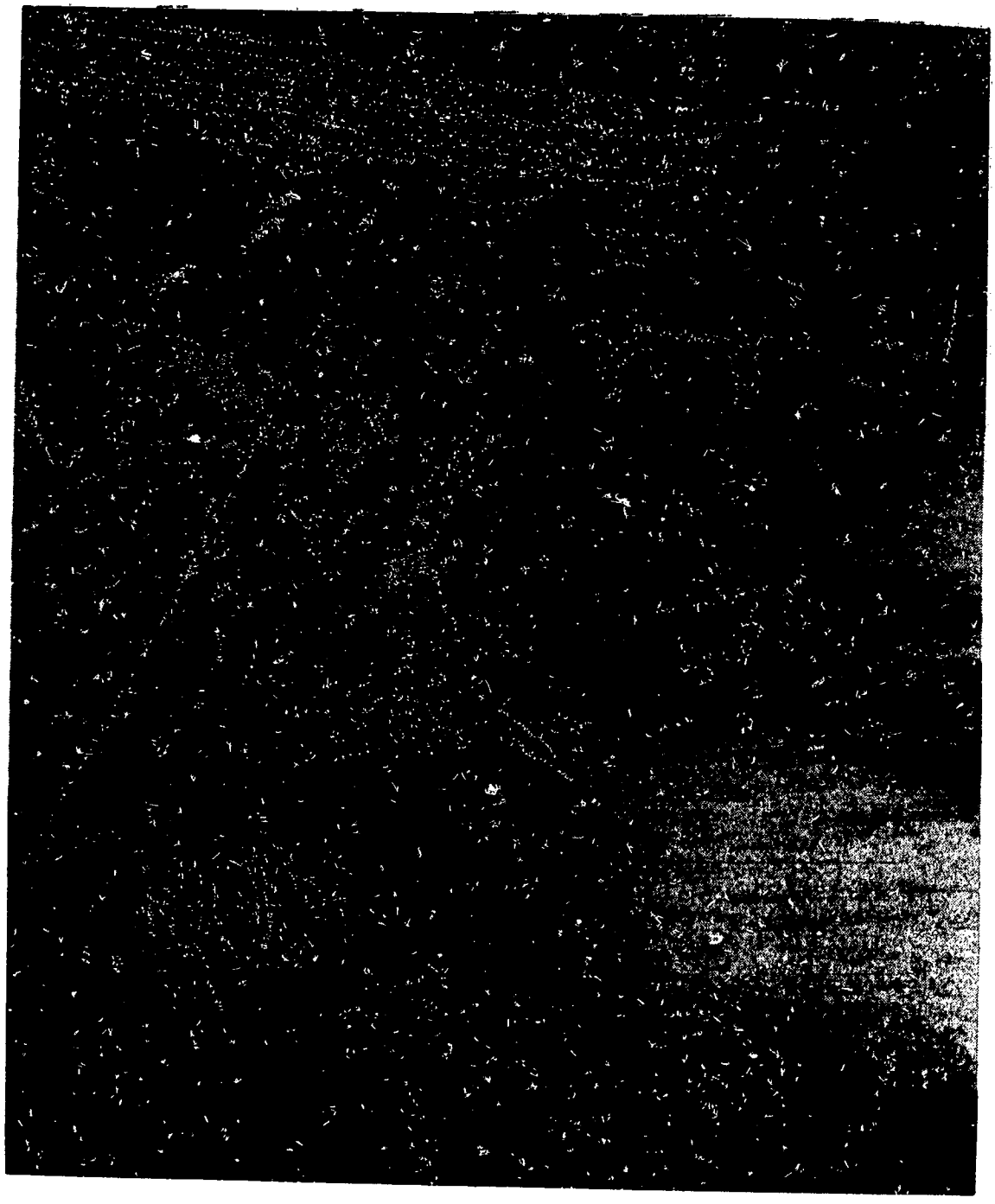

a) Schlieren photograph

Fig. 20. Experimental results for 0° swept, Type III interference flowfield (run 25, L_{ts} = 1.93 in., Re_1 = 1.538 x 10^6 $^1/_{ft}$).

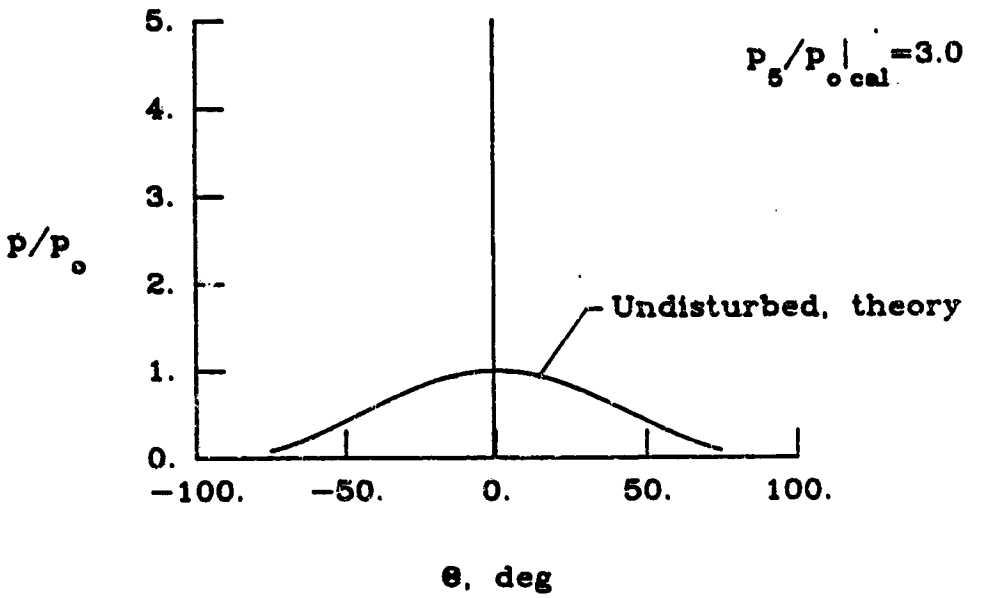

b) Pressure distribution

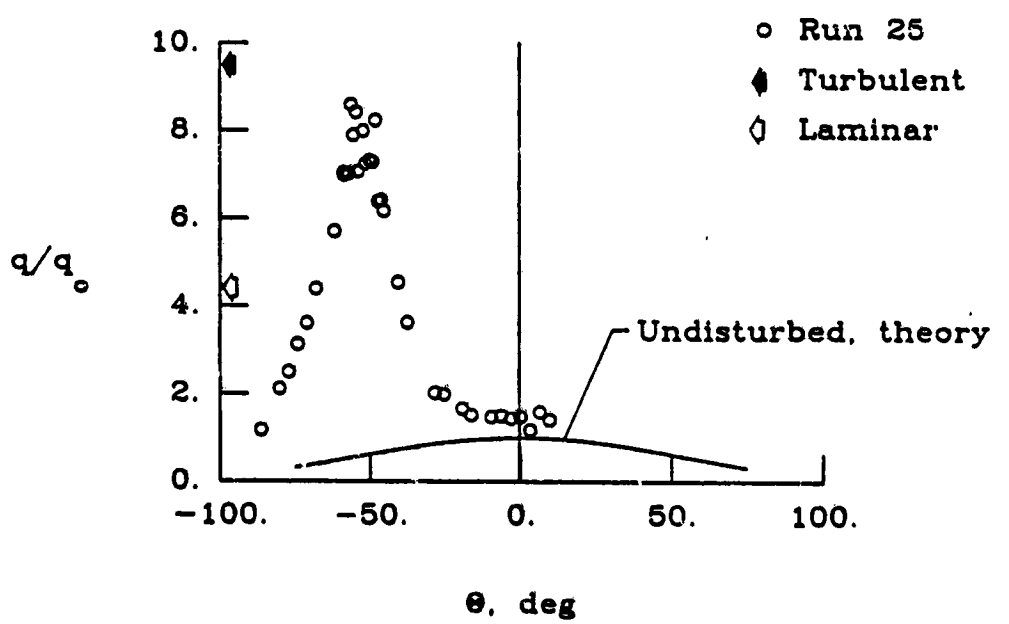

c) Heat transfer rate distribution

Fig. 20. Concluded.

transmitted shock length, L_{ts}, which was measured from the schlieren photographs shown in Figs. 19(a) and 20(a). These Type III interference tests were also presented by Wieting [9].

The prediction of peak pressure and peak heat transfer rate in region 5 (See Fig. 4(a).) was determined from the sensitivity analysis discussed above. The peak experimental pressure from run 26 was matched with the calculated pressure at the wall turning angle of 33° shown in Fig. 18(a). The calculated peak turbulent heat transfer rate is shown on the axis of ordinates in Fig. 19(c). Although the shear layer of the present test was shown to be turbulent, the laminar prediction is also included on the heat transfer rate plot. The experimental peak heat transfer rate is in good agreement with the predicted turbulent value shown in Fig. 19(c).

No pressure data were recorded during test run 25. Therefore, a wall turning angle of 33° was used in the prediction for this model test since the cylinder position was unchanged from run 25 to run 26 as shown in Table 2. Theoretical peak turbulent and laminar heat transfer rates for run 25 are shown in Fig. 20(c). The turbulent prediction is in good agreement with the experimental peak heat transfer rate as shown in Fig. 20(c).

The experimental heat transfer rate data for the Type III interference tend to be turbulent. This is supported by the transition Reynolds number criteria given by Edney [3] and Birch and Keyes [39]. The experimental data agree with the predictions of pressure and heat transfer rate from the EASI computer program; however, the predictions rely on experimental results.

4.2.2 Type IV Shock Wave Interference

The cylinder was translated both vertically and horizontally with respect to the shock generator trailing edge during the Type IV interference tests. (See

Table 2.) Because of this, a method was needed to assess the relative cylinder position with respect to the incoming incident shock wave. This was accomplished by calculating the oblique shock wave angle and extending a shock wave from the shock generator leading edge to the cylinder centerline at this angle. The oblique shock wave location was calculated with the assumptions that flow on the shock generator was inviscid and the oblique shock wave was straight. The distance Y_{inv}, is the calculated vertical distance between the extended oblique shock wave and the cylinder axis as shown in Fig. 21. The Type IV shock wave interference tests presented in this section are ordered by increasing Y_{inv} as tabulated in Table 3. Using this method, a calculation of the incident shock position is not correct because the boundary layer, through the displacement thickness, alters the shock wave above the generator wedge. However, the Y_{inv} distance does provide a good estimate of the relative movements of the cylinder position with respect to the oblique shock wave from one test run to another.

Results from the 0° swept, Type IV shock wave interference model tests are shown in Figs. 2[illegible] for increasing Y_{inv}. This arrangement shows the effect of downward adjustment of the cylinder with respect to the incoming incident shock wave. The experimental results are presented as schlieren photographs of the shock wave interference pattern and as pressure and heat transfer rate distributions on the instrumented cylinder. Also, predictions of the peak pressure and peak heat transfer rate were made by the EASI computer program for each test run using freestream conditions from Table 1 and measured transmitted shock lengths from Table 3. These predictions assumed supersonic jet impingement normal to the cylinder surface in either region 7 or region 8. (See Fig. 5(a).) The heating rate is more sensitive to the resultant deflection angle (either θ_7 or θ_8 on Fig. 5(b)) than the peak pressure

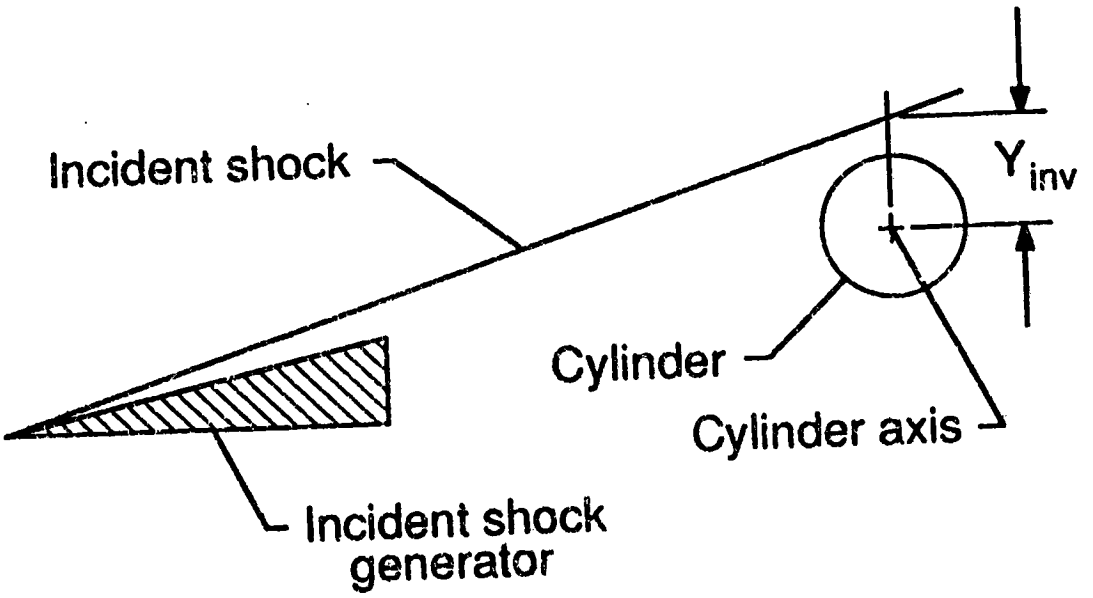

Fig. 21. Location of Y_{inv} with respect to the incident shock generator and instrumented cylinder.

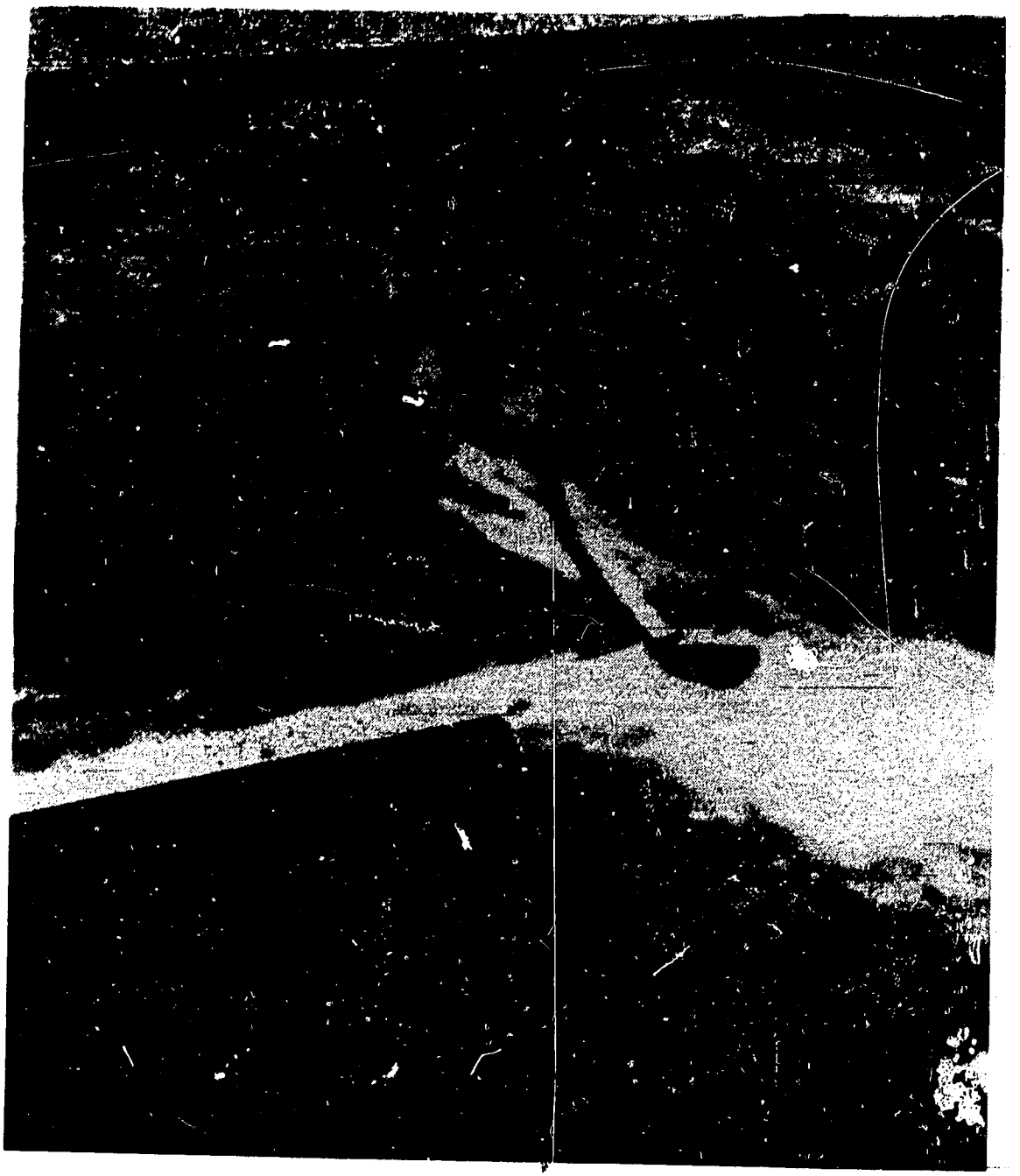

a) Schlieren photograph

Fig. 22. Experimental results for 0° swept, Type IV interference flowfield (run 61, $Re_1 = 1.456 \times 10^6$ $^1/_{ft}$).

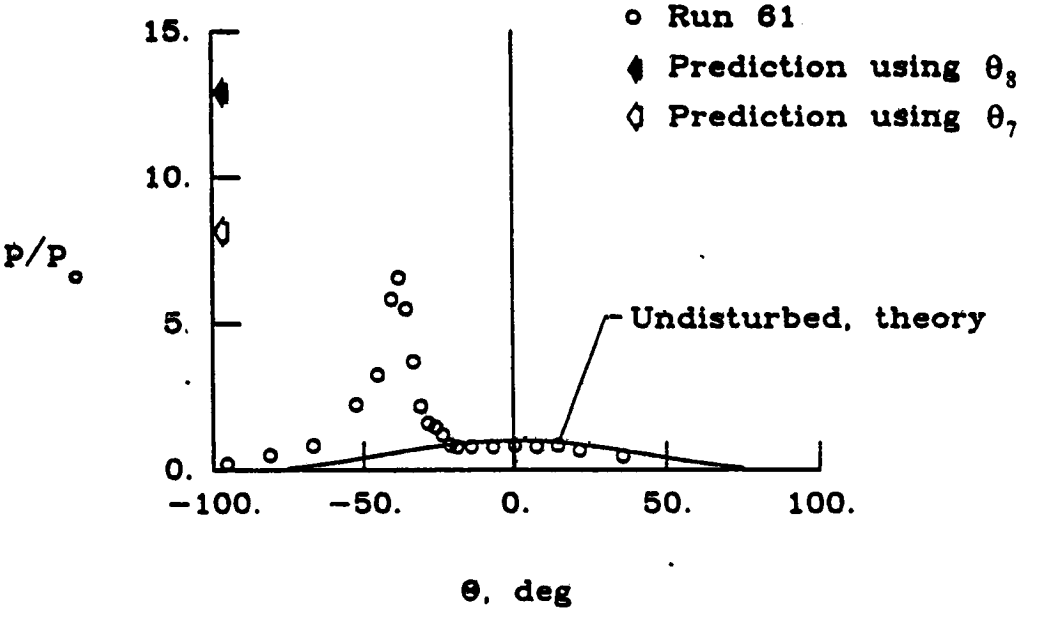

b) Measured pressure distribution compared with undisturbed theory. Also shown are zonal maximum pressure rise estimates corresponding to θ_7 and θ_8 turning angles.

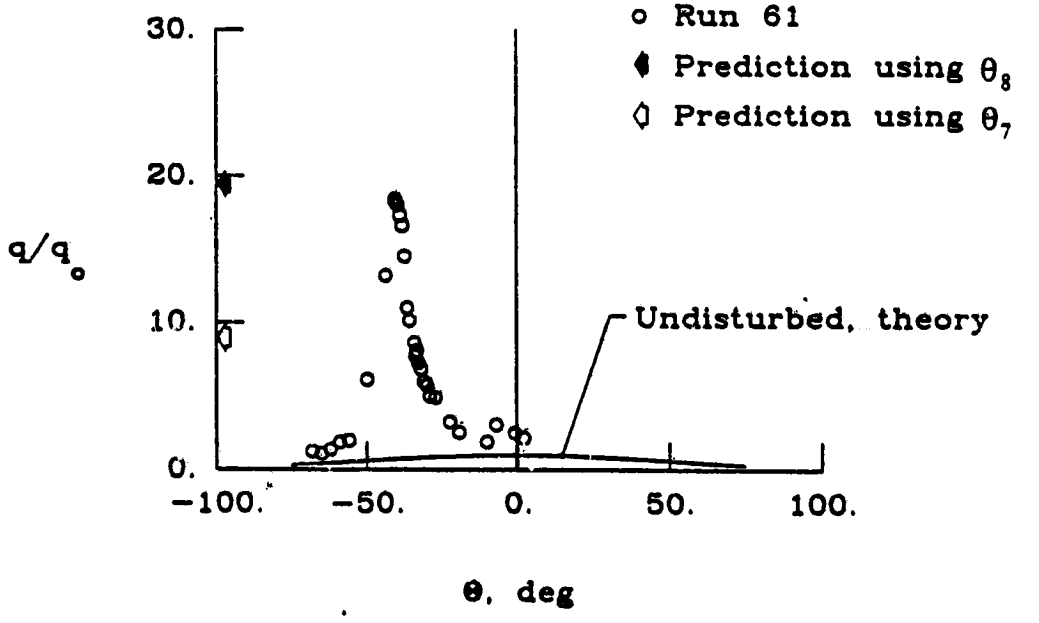

c) Measured heat transfer rate distribution compared with undisturbed theory. Also shown are zonal maximum heat transfer rate estimates corresponding to θ_7 and θ_8 turning angles.

Fig. 22. Concluded.

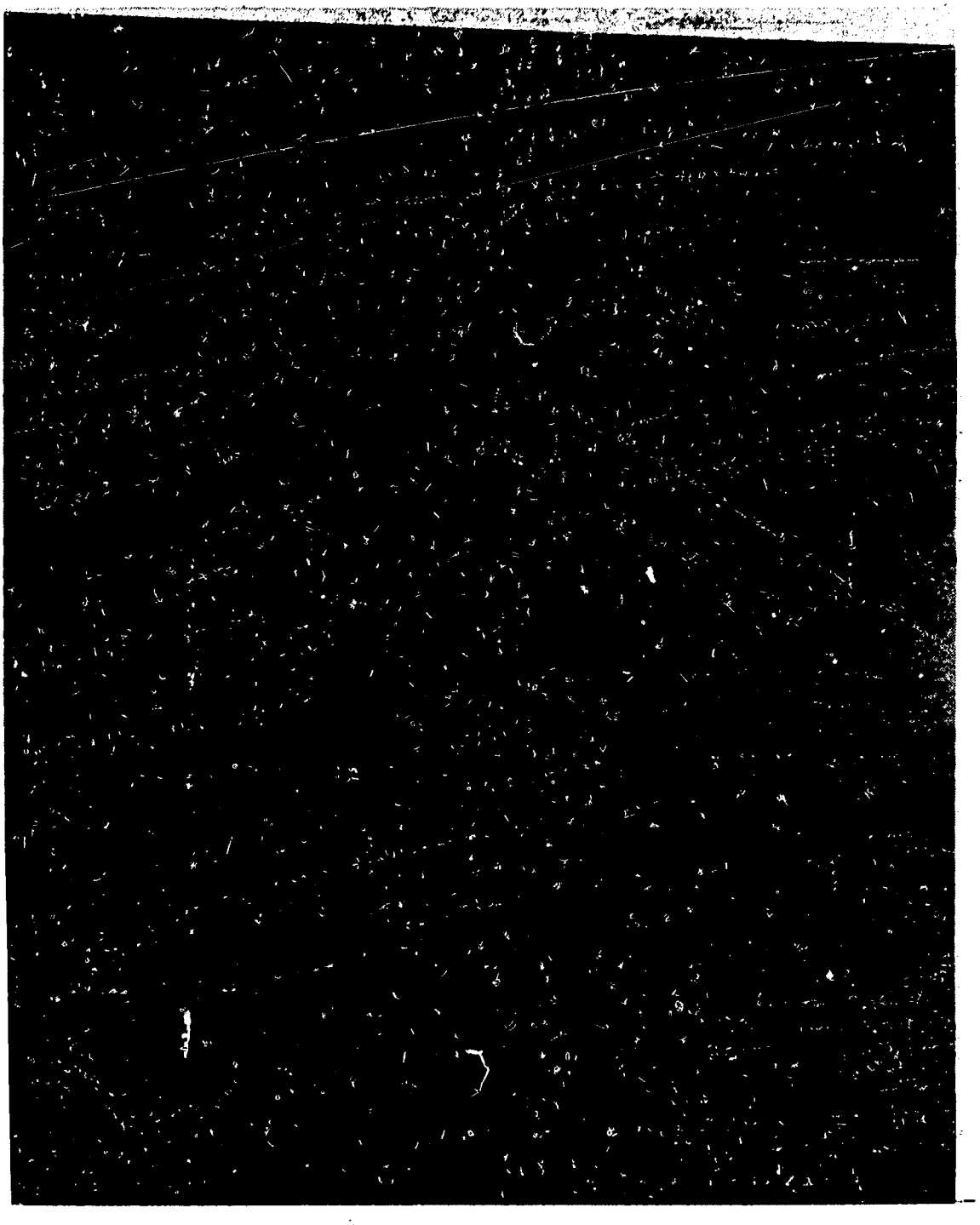

a) Schlieren photograph

Fig. 23. Experimental results for 0° swept, Type IV interference flowfield (run 21, $Re_1 = 1.564 \times 10^6$ $^1/_{ft}$).

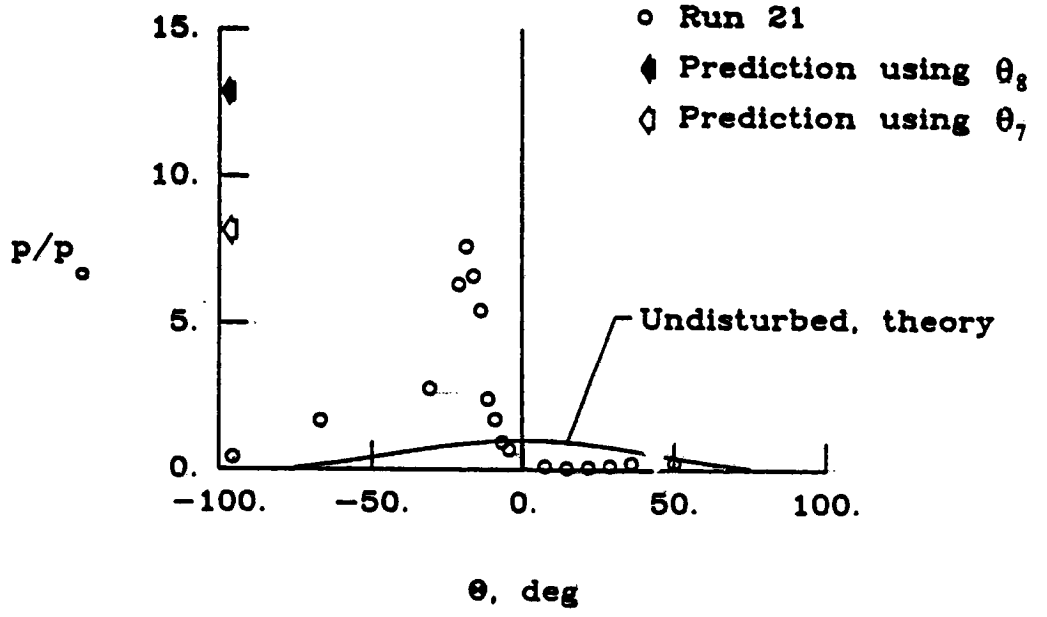

b) Pressure distribution

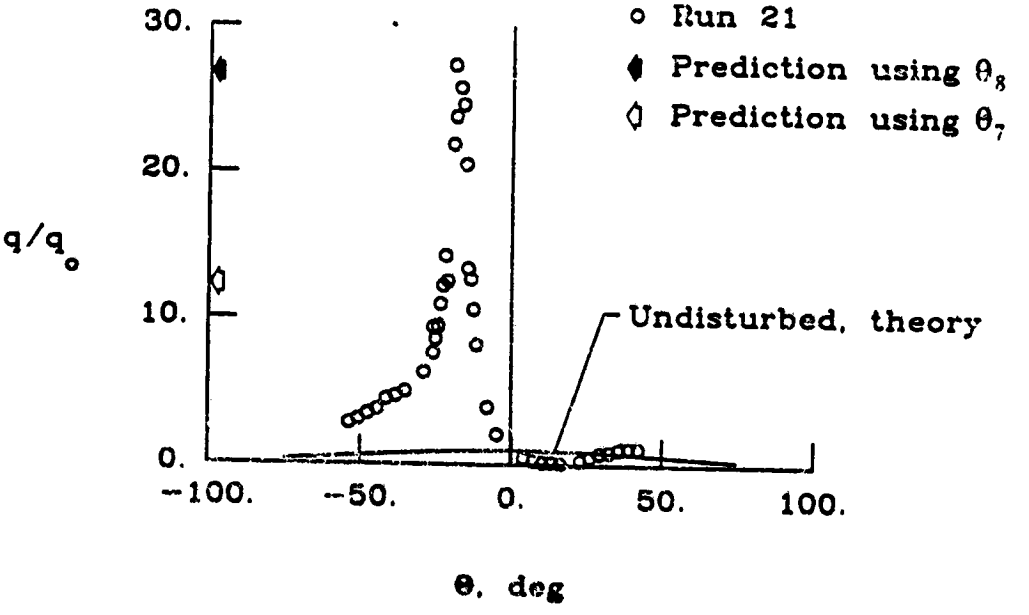

c) Heat transfer rate distribution

Fig. 23. Concluded.

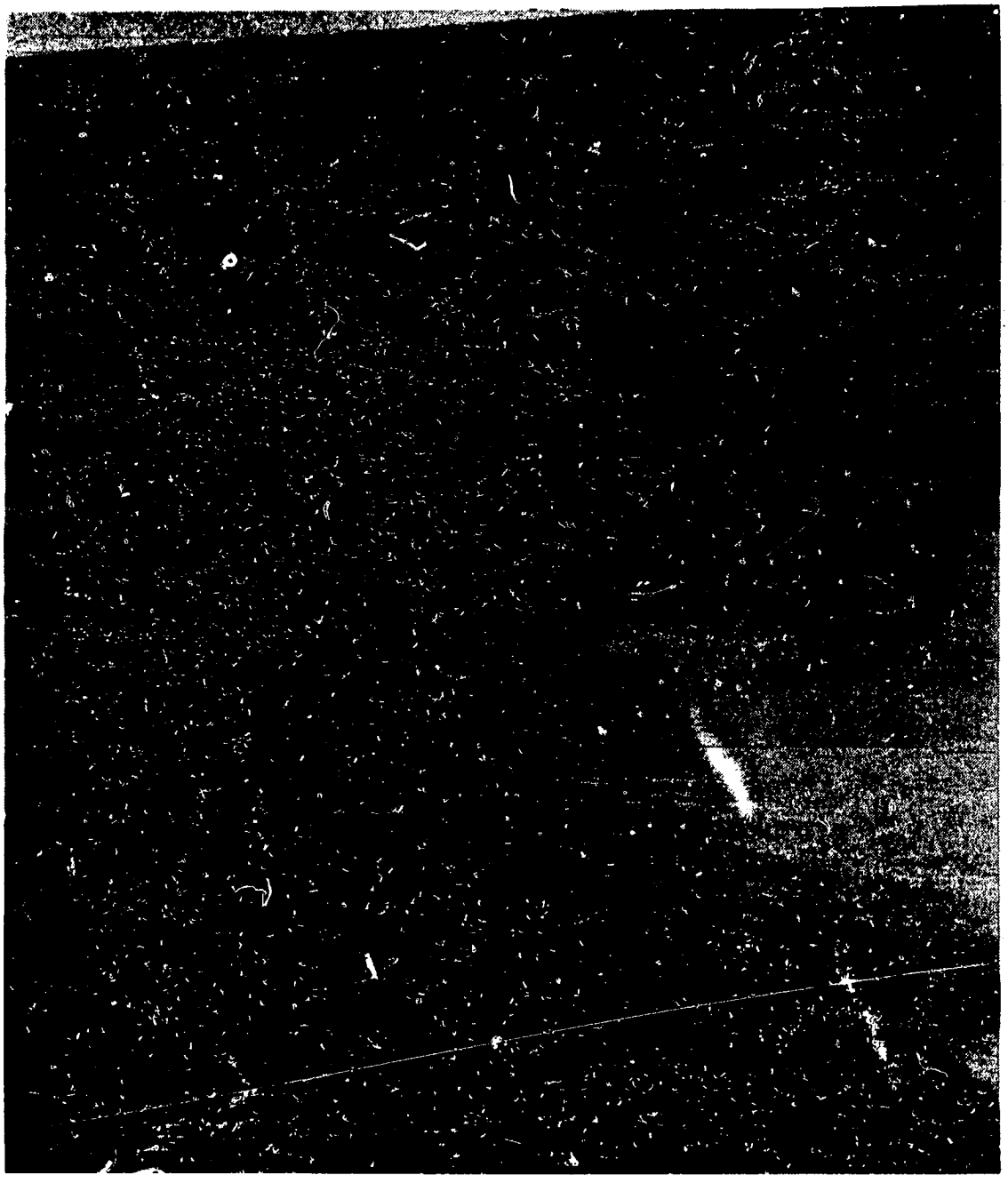

a) Schlieren photograph

Fig. 24. Experimental results for 0° swept, Type IV interference flowfield (run 59, $Re_1 = 1.433 \times 10^6$ $^1/_{ft}$).

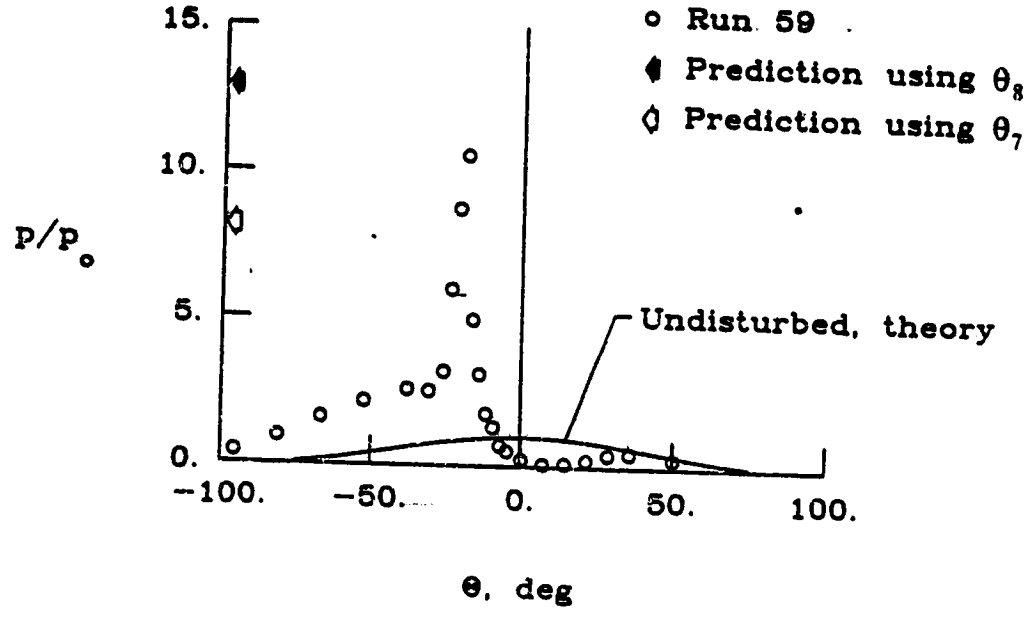

b) Pressure distribution

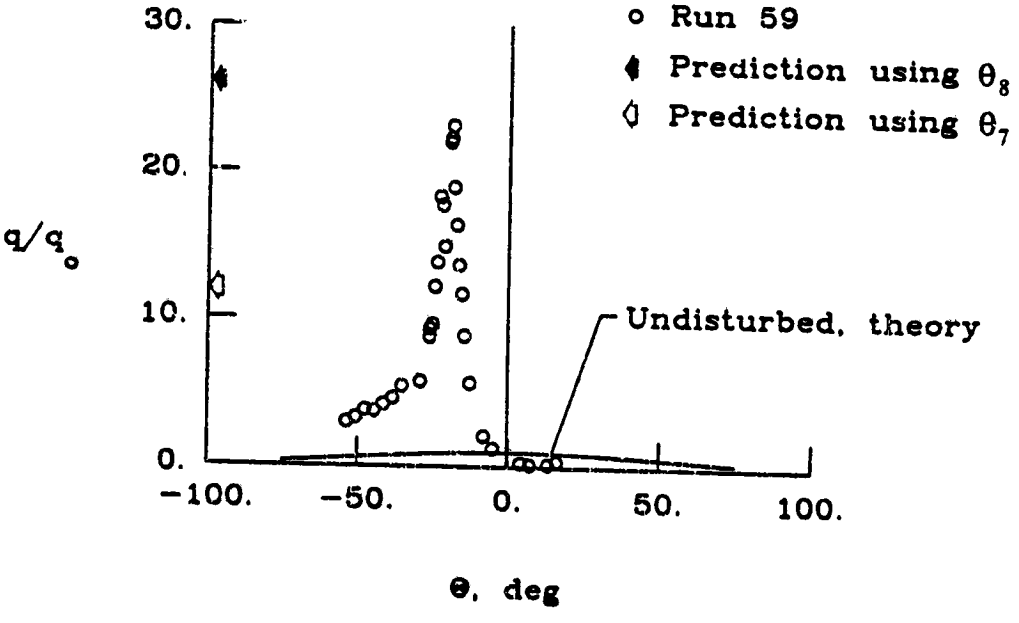

c) Heat transfer rate distribution

Fig. 24. Concluded.

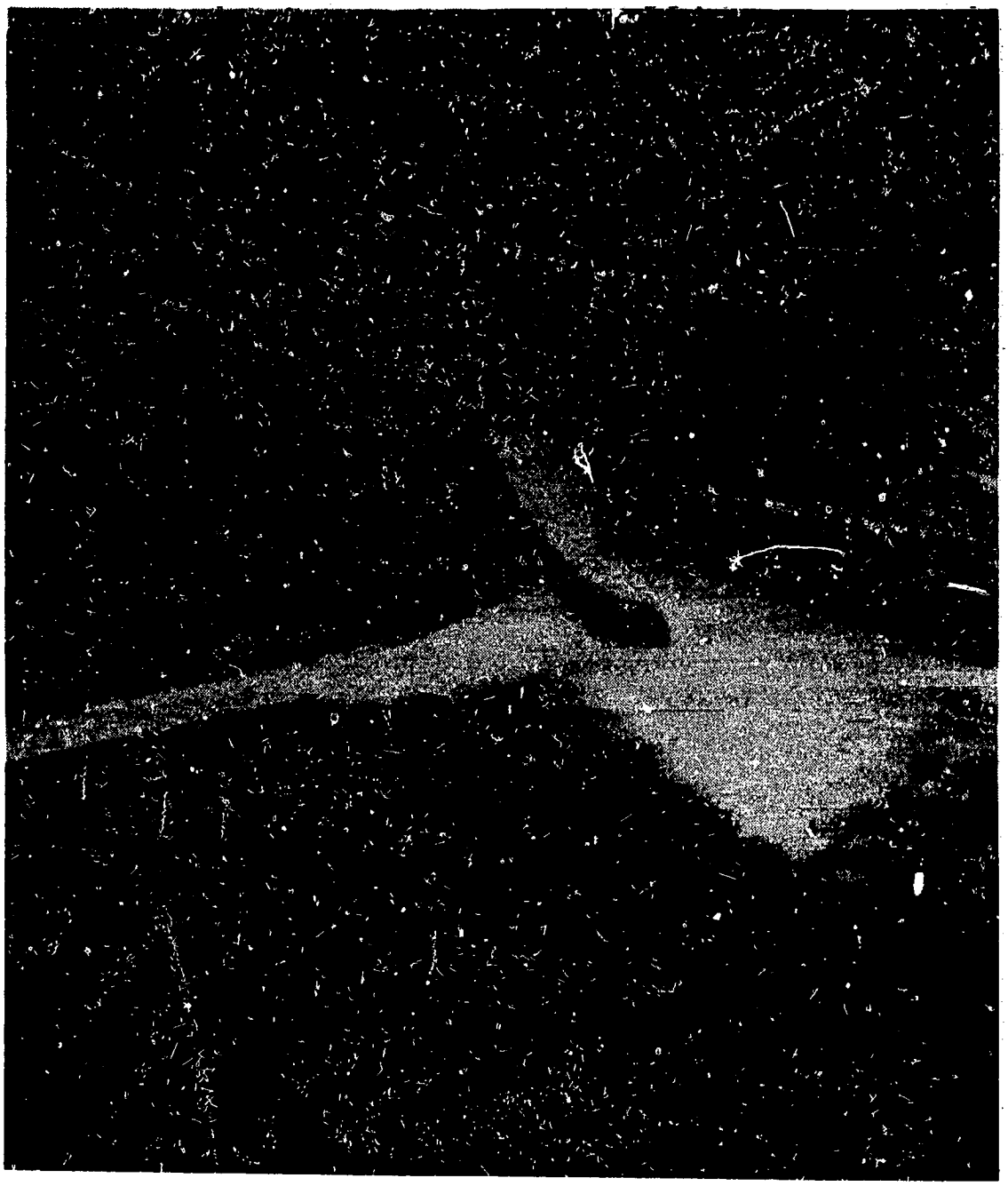

a) Schlieren photograph

Fig. 25. Experimental results for 0° swept, Type IV interference flowfield (run 60, $Re_1 = 1.448 \times 10^6$ $^1/_{ft}$).

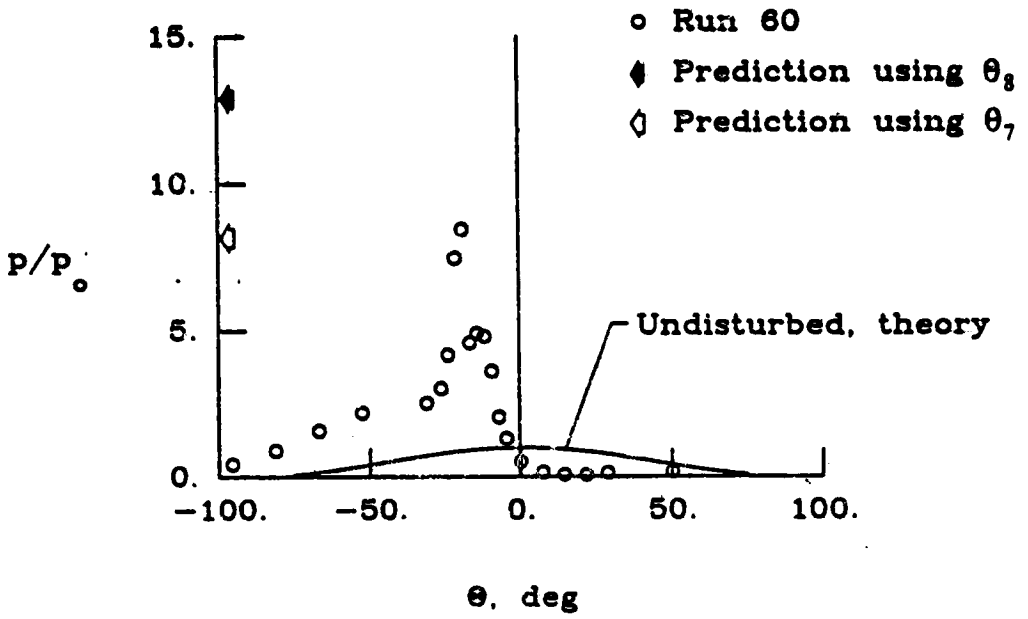

b) Pressure distribution

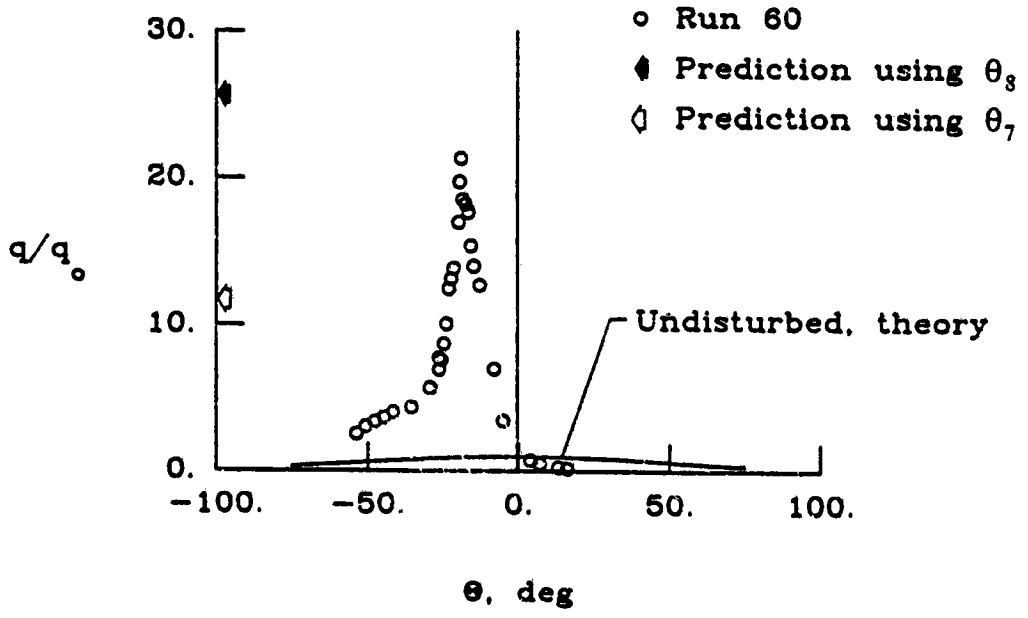

c) Heat transfer rate distribution

Fig. 25. Concluded.

rise. However, both levels are shown on the figures. It is also important to note that since these flows are behind normal shocks, only a laminar heating prediction is relevant. Hence, the estimated peak heating levels assume laminar flow.

The schlieren photographs (See Figs. 22(a)-25(a).) show the details of the Type IV shock wave interference pattern, including the supersonic jet impinging on the cylinder surface. The surface pressure and heat transfer rate distributions shown on Figs. 22(b)-25(b) and Figs. 22(c)-25(c), respectively, are similar to distribution trends postulated by Edney [3] and sketched in Fig. 9 for supersonic jet impingement. The experimental results show very high pressures and heat transfer rates in the narrow impingement region with expansions and compressions on either side of the impinging jet. Calculations of the jet width by the EASI code are given on Table 3 and range from 0.140 inches for run 61 to 0.074 inches for run 21. The calculated jet width is a function of the input transmitted shock length. The region on the cylinder surface affected by the jet appears to be wider than the calculated jet width (which was between 2.8° and 5.3°) for the Type IV shock wave interference model tests shown in this section. Note that the pressure and heat transfer rate distributions shown in Figs. 22-25 are sharp and well defined at the supersonic jet impingement region because of the close gauge spacing. The experimental peak pressures on the cylinder surface tend to be predicted by the region 7 stagnation pressure, and the peak heat transfer rates tend to be predicted by results from region 8.

4.3 15° Swept Interference Results

Experimental pressure and heat transfer rate distributions for the 15° swept model with a shock wave interference flowfield are shown on Figs. 26-33. These results include undisturbed theoretical pressure and heat transfer distributions calculated using the methods given by Beckwith and Gallagher [24]. Schlieren photographs are not included because facility window limitations of the 48" HST prevented a schlieren line of sight along the swept cylinder axis.

The 15° swept shock wave interference test results are presented in the order given in Table 4. The nominal test condition runs are presented first, and then the off nominal condition results are presented. The order at a given test condition is for increasing Y_{inv}, similar to the presentation of the test runs in section 4.2.2. The distance Y_{inv} shows how the relative cylinder positions affect surface pressure and heat transfer rate distributions without the visual evidence of the shock wave interference type shown on a schlieren photograph. This ordering scheme shows the experimental results as the cylinder is moved downward with respect to the incident shock generator. For example, the Type III shock wave interference results are shown first, then the Type IV results, and so on.

The cylinder position variation at the nominal test condition is shown in Figs. 26-30. Results from run 70, shown in Fig. 26, were for the highest relative cylinder position at the nominal test condition. The surface distributions are not similar to the 0° swept, Type III distributions shown in the figure as a dashed line. On the basis of the location of maximum pressure rise, these results are a Type II approaching Type III transition.

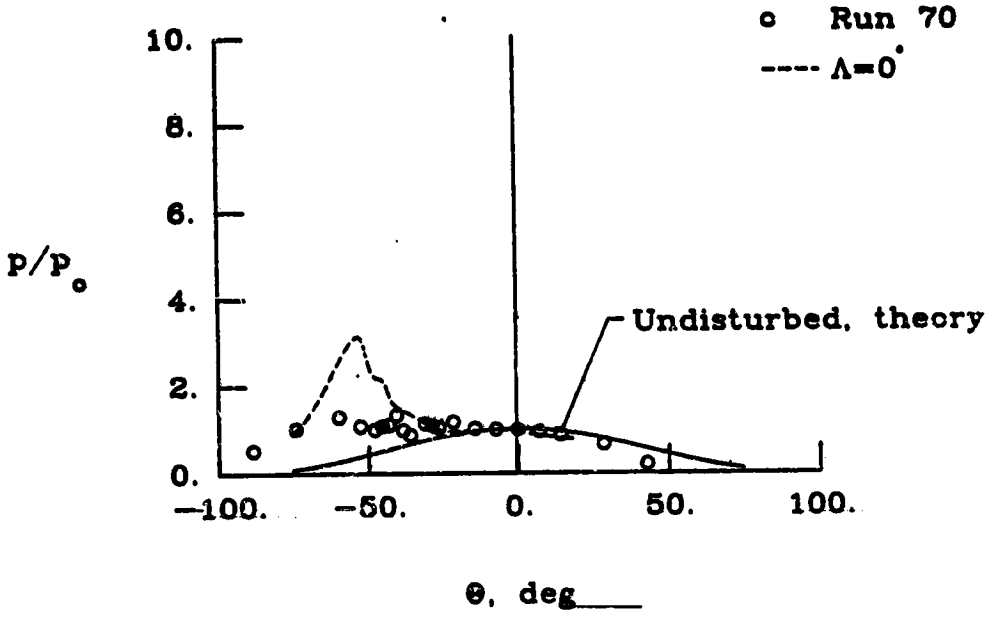

a) Pressure distribution

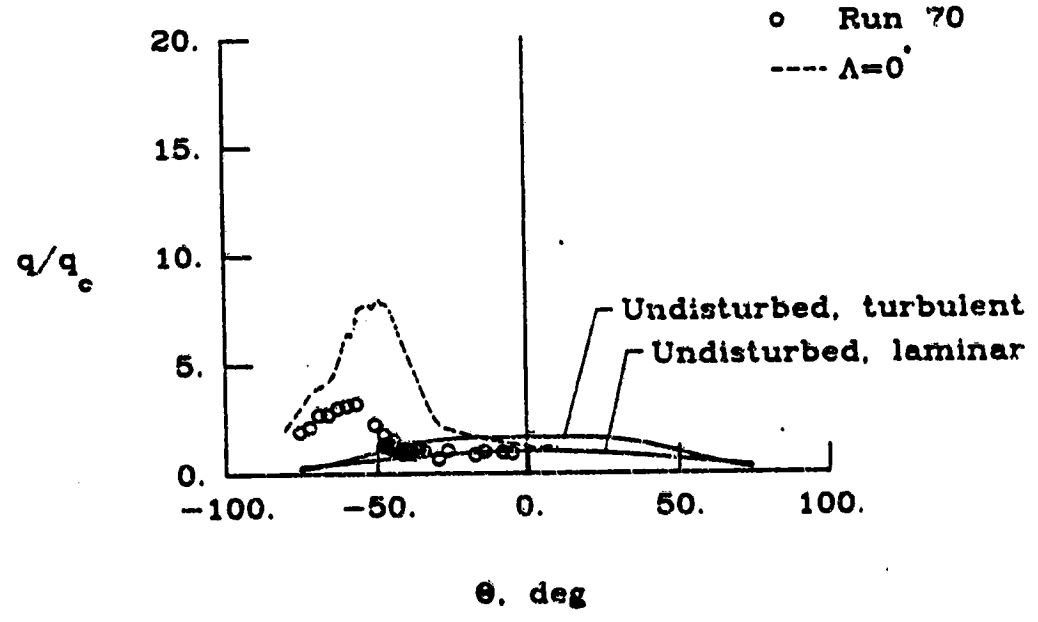

b) Heat transfer rate distribution

Fig. 26. Experimental results for 15° swept interference flowfield (run 70, $Re_1 = 1.471 \times 10^6$ 1/ft) compared with unswept results (run 26).

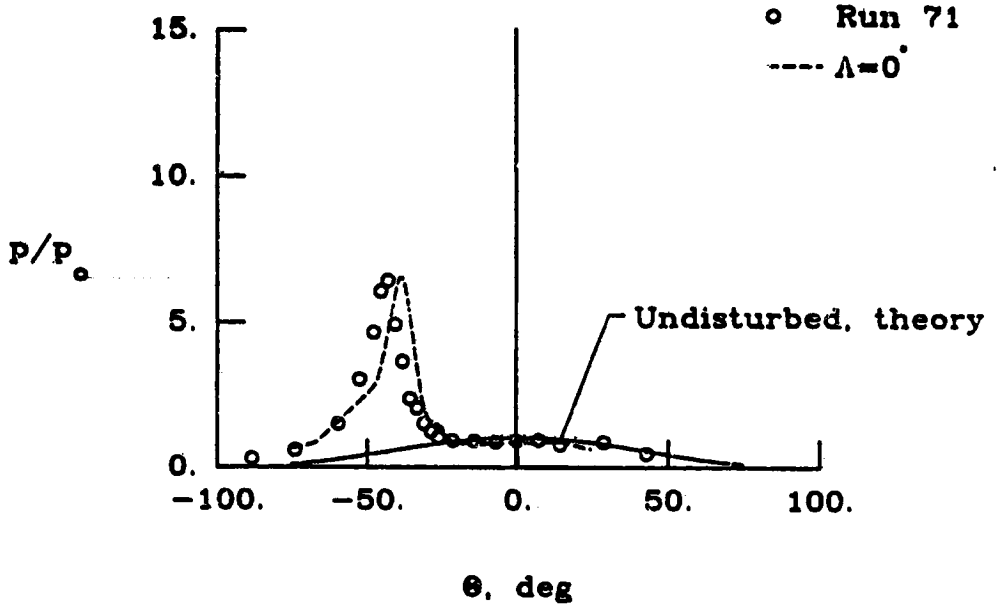

a) Pressure distribution

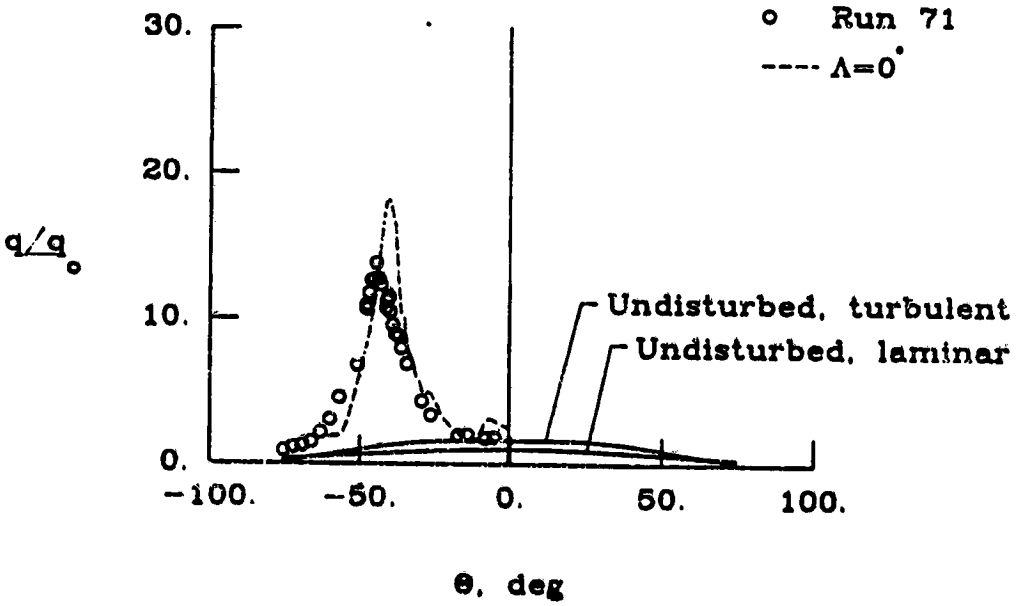

b) Heat transfer rate distribution

Fig. 27. Experimental results for 15° swept interference flowfield (run 71, $Re_1 = 1.376 \times 10^6$ $^1/_{ft}$) compared with unswept results (run 61).

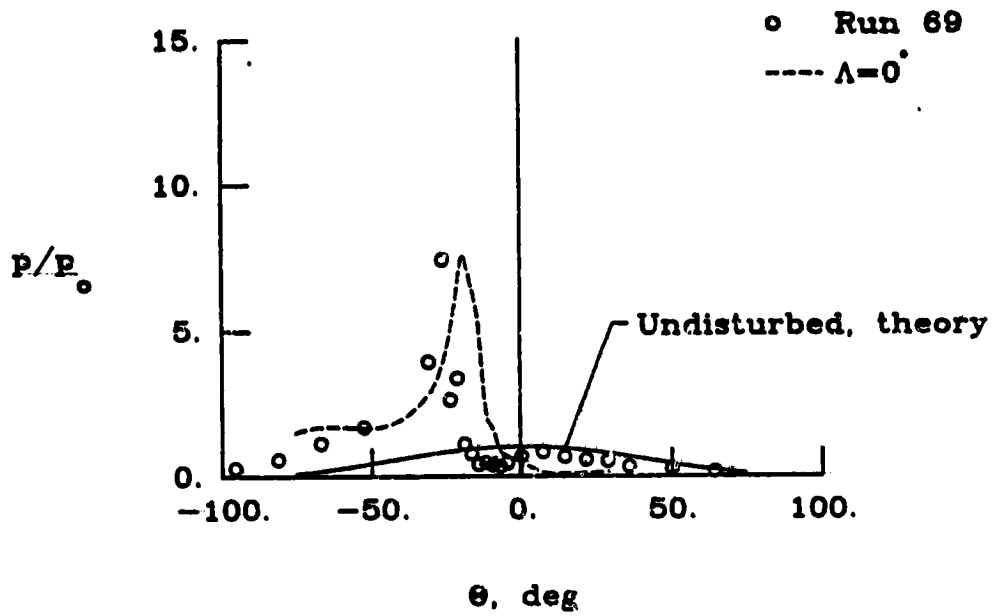

a) Pressure distribution

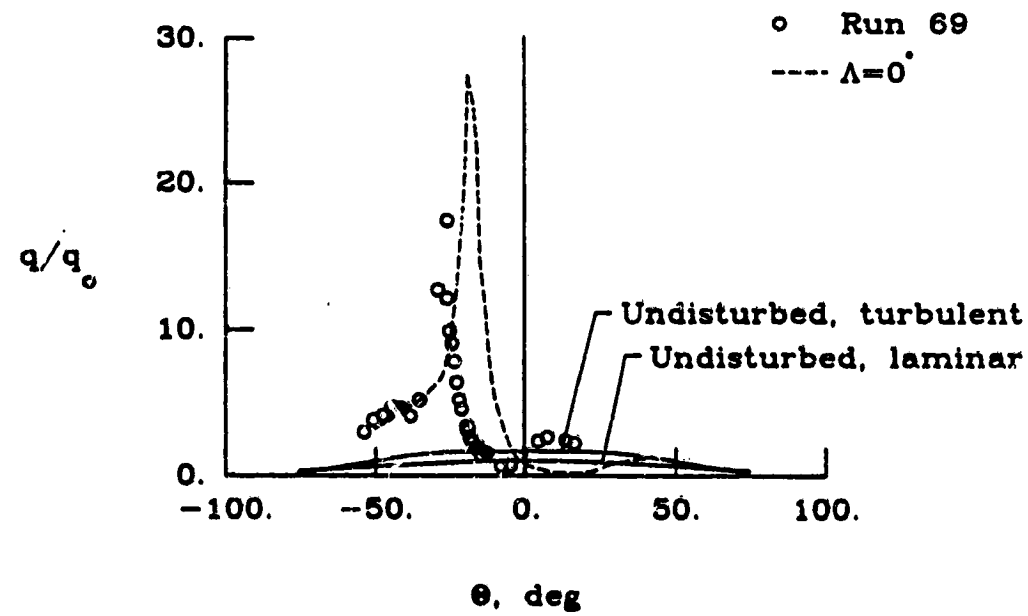

b) Heat transfer rate distribution

Fig. 28. Experimental results for 15° swept interference flowfield (run 69, $Re_1 = 1.501 \times 10^6$ $^1/_{ft}$) compared with unswept results (run 21).

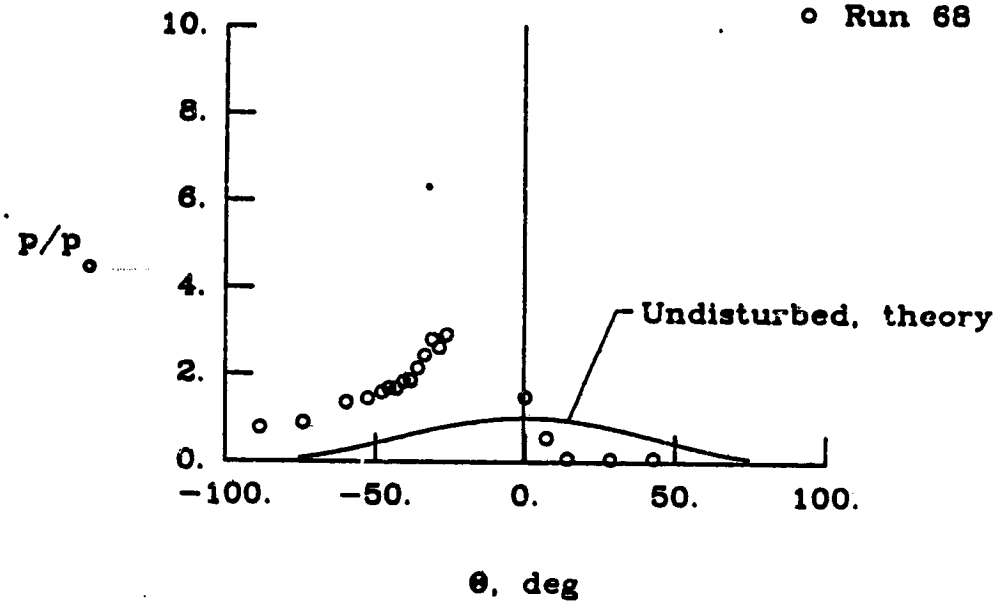

a) Pressure distribution

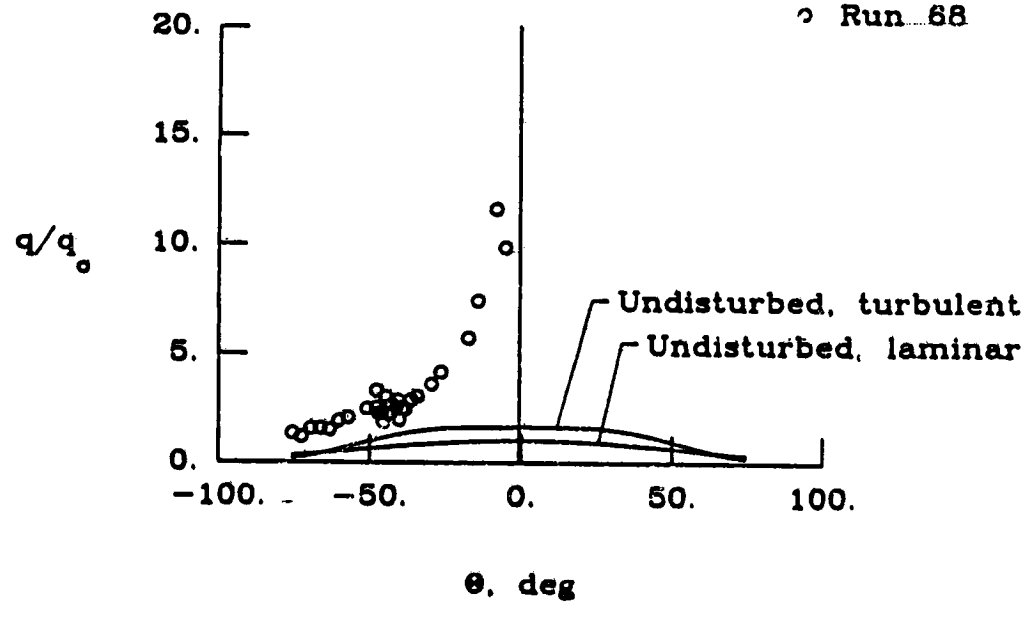

b) Heat transfer rate distribution

Fig. 29. Experimental results for 15° swept interference flowfield (run 68, $Re_1 = 1.469 \times 10^6$ $^1/_{ft}$).

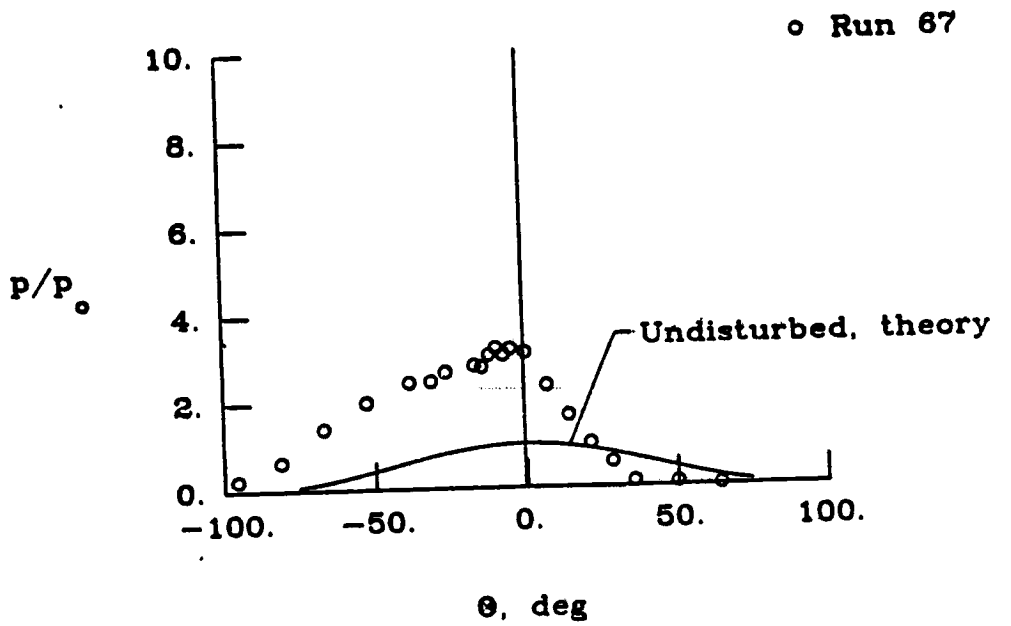

a) Pressure distribution

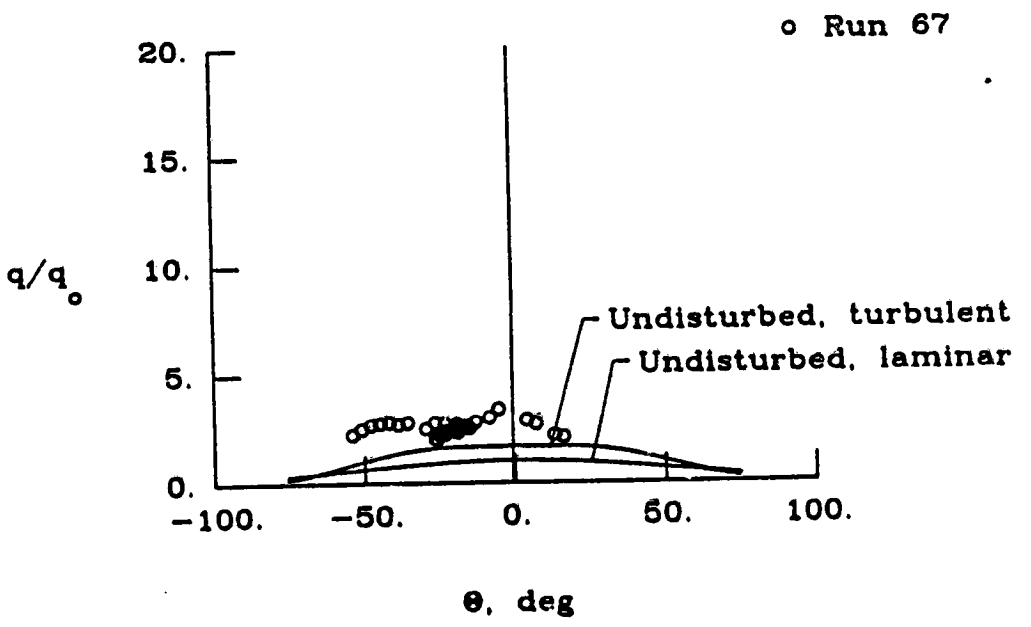

b) Heat transfer rate distribution

Fig. 30. Experimental results for 15° swept interference flowfield (run 67, $Re_1 = 1.484 \times 10^6$ $^1/_{ft}$).

C-2

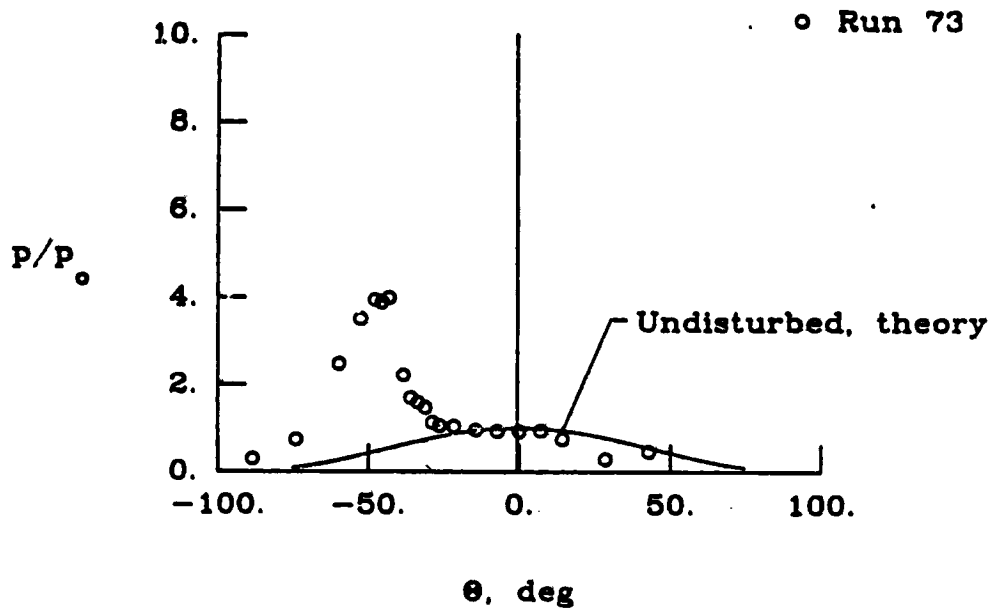

a) Pressure distribution

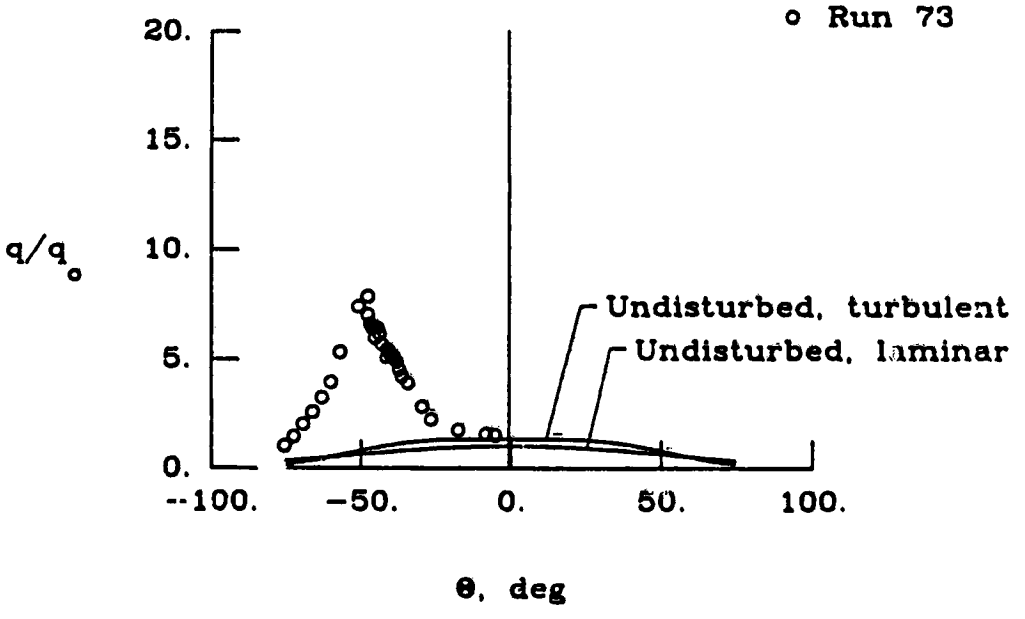

b) Heat transfer rate distribution

Fig. 31. Experimental results for 15° swept interference flowfield (run 73, $Re_1 = 0.712 \times 10^6$ $^1/_{ft}$).

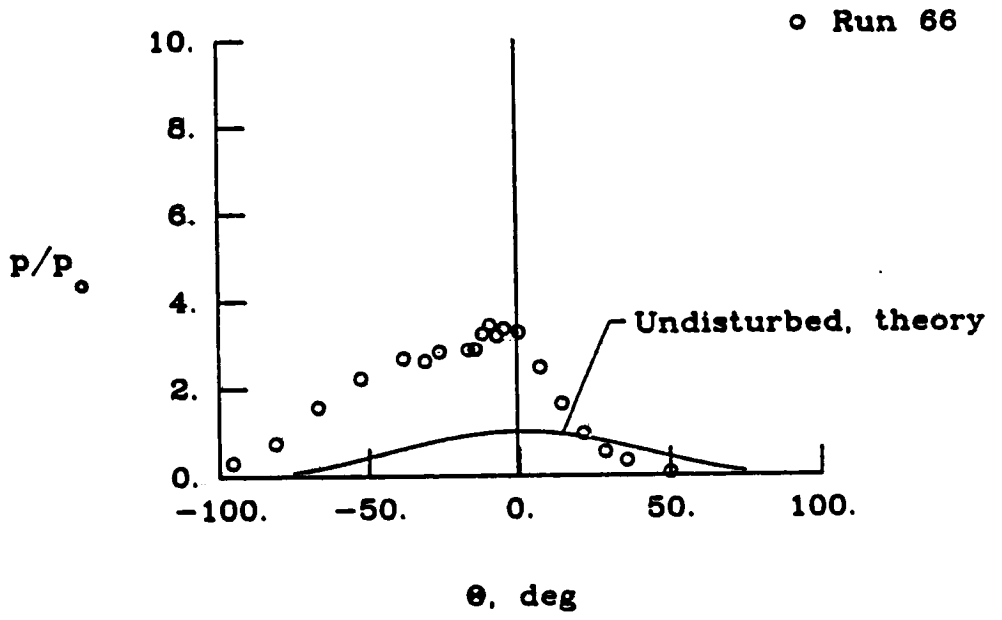

a) Pressure distribution

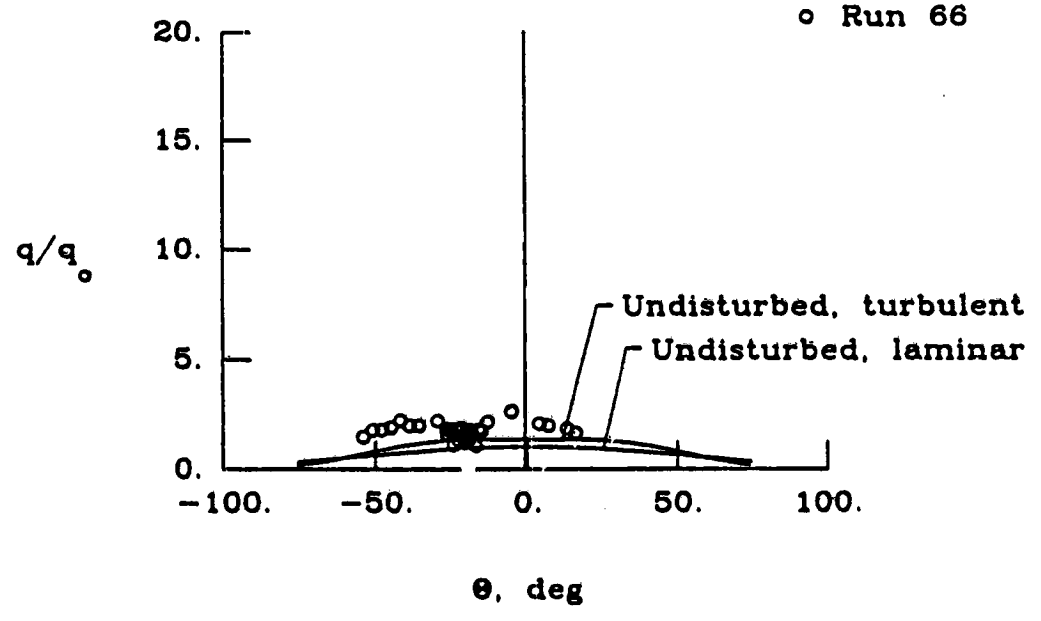

b) Heat transfer rate distribution

Fig. 32. Experimental results for 15° swept interference flowfield (run 66, $Re_1 = 0.702 \times 10^6$ 1/ft).

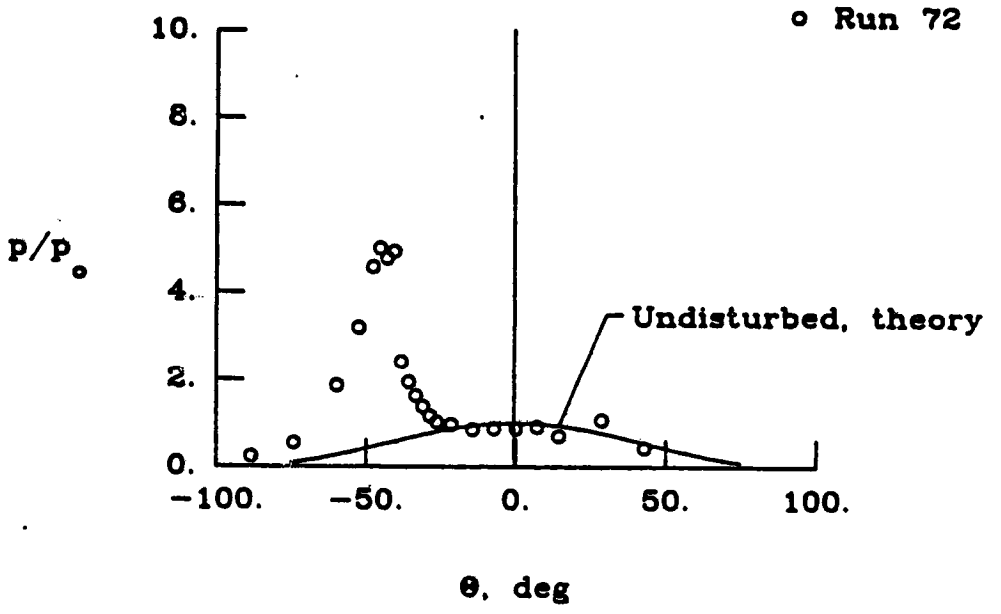

a) Pressure distribution

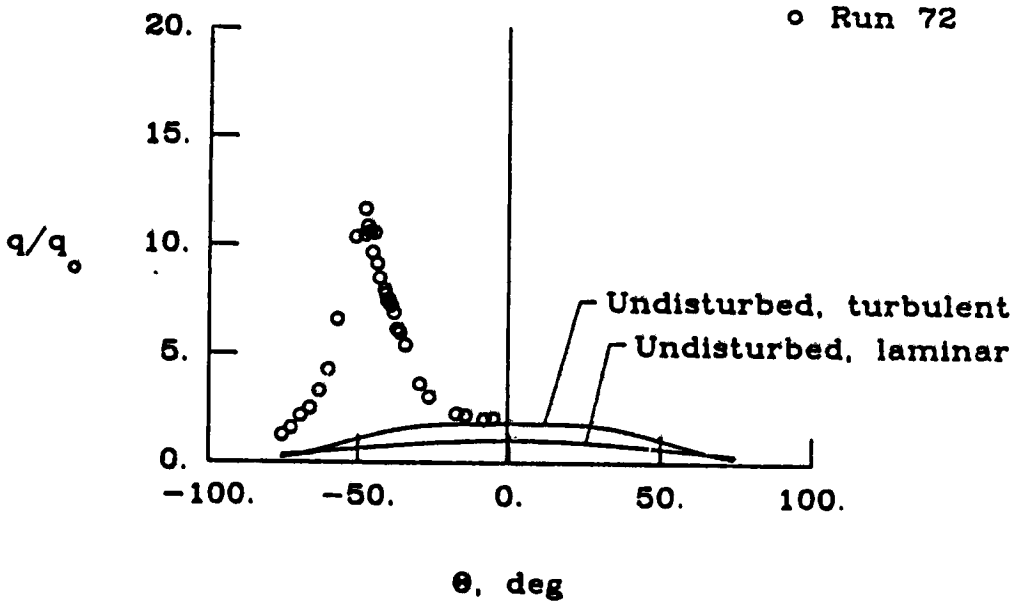

b) Heat transfer rate distribution

Fig. 33. Experimental results for 15° swept interference flowfield (run 72, $Re_1 = 1.874 \times 10^6$ $^1/_{ft}$).

Table 4 Calculated Y_{inv} for 15° and 30° swept model tests

Run	Λ deg	Y_{inv} in	Re_1 1/ft x10-6
70	15	-0.49	1.471
71	15	-0.17	1.376
69	15	0.11	1.501
68	15	0.30	1.469
67	15	0.68	1.484
73	15	-0.14	0.712
66	15	0.71	0.702
72	15	-0.18	1.874
77	30	-0.19	1.528
98	30	0.40	1.467
75	30	0.41	1.480
78	30	0.62	1.484
76	30	0.77	1.454
80	30	0.43	0.715
79	30	0.41	1.830

As the cylinder was moved downward, the peak pressure and heat transfer rate increased as shown in Figs. 27 and 28. A comparison of the surface distributions with the 0° swept, Type IV shock wave interference distributions (shown on the figures) shows similar pressure and heat transfer distributions on the cylinder surface. Therefore, it is concluded that Figs. 27 and 28 show the surface effects from a Type IV shock wave interference for the 15° swept model tests. Note that the 0° and 15° swept peak pressures are nearly at the same level because the supersonic jet flow stagnates through a strong shock wave. However, the peak heat transfer rate is reduced with sweep probably because the spanwise velocity component along the forward face of the swept cylinder did not allow the supersonic jet to impinge normal to the surface.

Results shown in Fig. 29 were at the next cylinder position and are probably from a supersonic jet grazing the cylinder surface near the transition between a Type IV and Type V shock wave interference. The lowest relative cylinder position at the nominal test condition was for run 67 shown in Fig. 30, and is probably from a Type V shock wave interference.

Predictions which were included for the 0° swept interference tests are not given in this section because the EASI code is for a two-dimensional interaction, but correlations with the 0° swept data will be presented in the next chapter. Although no visual evidence of the interference pattern was available, a comparison of the data shown in Figs. 27 and 28 with Edney's postulated trends [3] and the 0° swept data show they are from a Type IV interference. Also, the results shown in Figs 26-30 span the gap that includes the Type IV shock wave interference results.

4.4 30° Swept Interference Results

Experimental pressure and heat transfer rate distributions for the 30° model tests with shock wave interference flowfield are shown in Figs. 34-40. These results are presented in the order shown in Table 4 for increasing Y_{inv} which is the same way that results for the 15° swept model tests were presented in the section 4.3. The experimental results include the undisturbed theoretical pressure and heat transfer rate distributions [24].

Surface pressure and heat transfer rate distributions for the tests at the nominal condition are shown in Figs. 34-38. The cylinder was at the upper relative location during run 77. Experimental results from this run are compared with the 0° swept, Type III results as shown in Fig. 34. The comparison shows that the surface distributions are similar; however, the 30° swept results are at a lower level. Therefore, the experimental distributions for run 77 were probably from Type III shock wave interference.

The pressure and heat transfer rate distributions shown in Figs. 35-37 are compared with the 0° swept, Type IV results. The 30° swept results have sharp, well defined peaks with secondary expansion and compressions on either side of the peaks similar to the results for the 0° swept, Type IV results. The distributions are also similar to the Type IV distributions postulated by Edney [3] and shown in Fig. 9. Therefore, the distributions given in Figs. 35-37 are believed to show the surface effects from Type IV supersonic jet impingement for the 30° swept model tests. Note that the peak pressure levels are near the 0° swept results, but the heat transfer rate peaks are reduced. For the lower cylinder location, the pressure distributions shown in Fig. 38(a) can be caused by either a grazing Type IV or a Type V shock wave interference. Therefore, the pressure and heat transfer rate distributions for

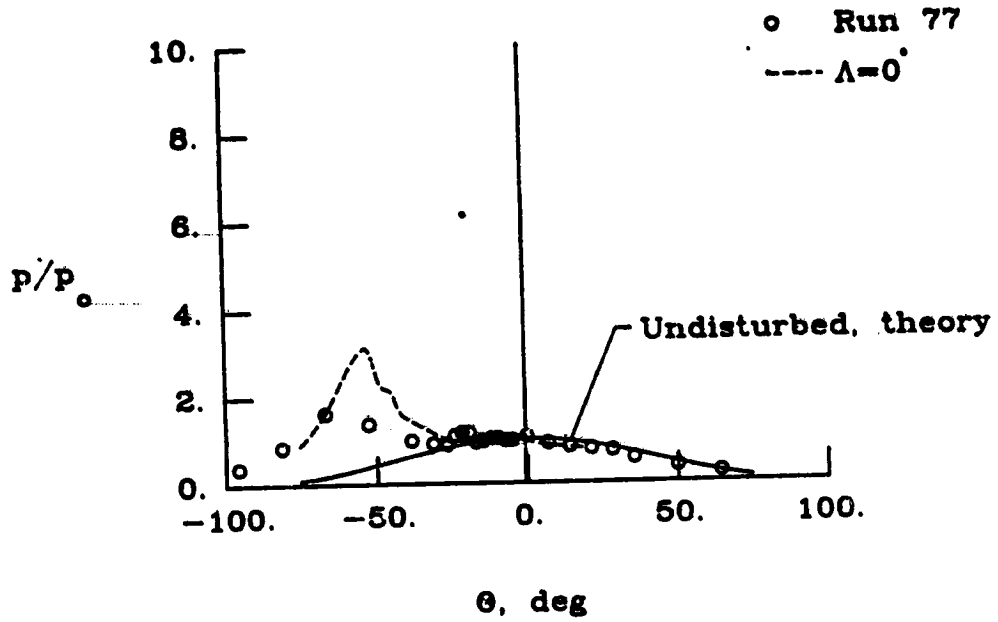

a) Pressure distribution

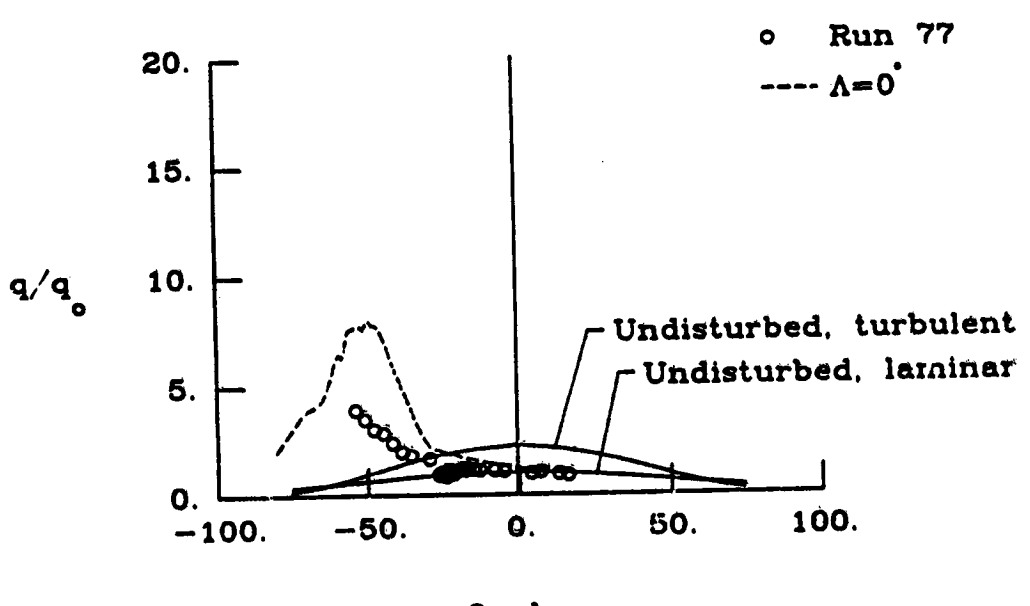

b) Heat transfer rate distribution

Fig. 34. Experimental results for 30° swept interference flowfield (run 77, $Re_1 = 1.528 \times 10^6$ $^1/_{ft}$) compared with unswept results (run 26).

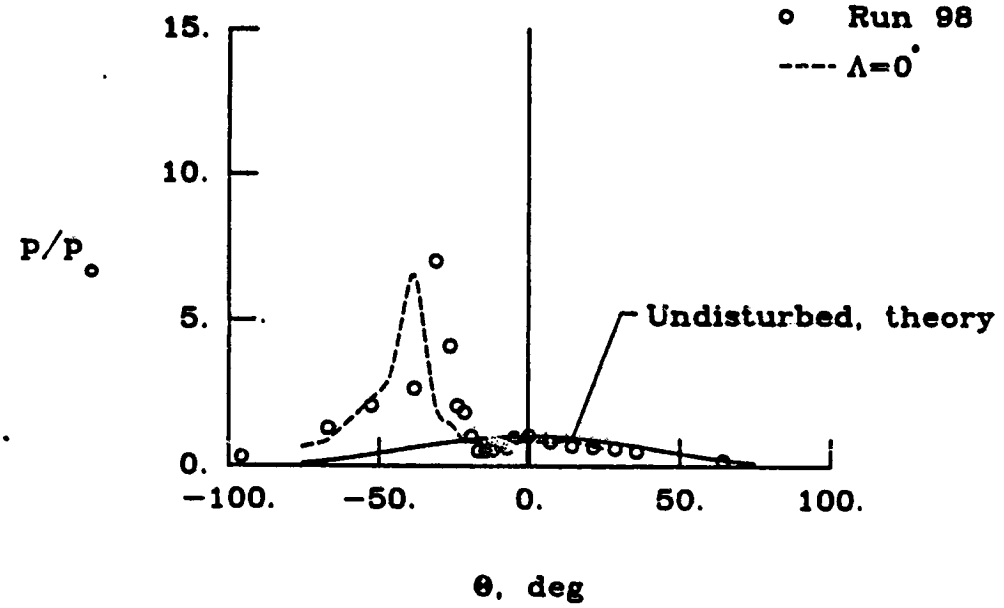

a) Pressure distribution

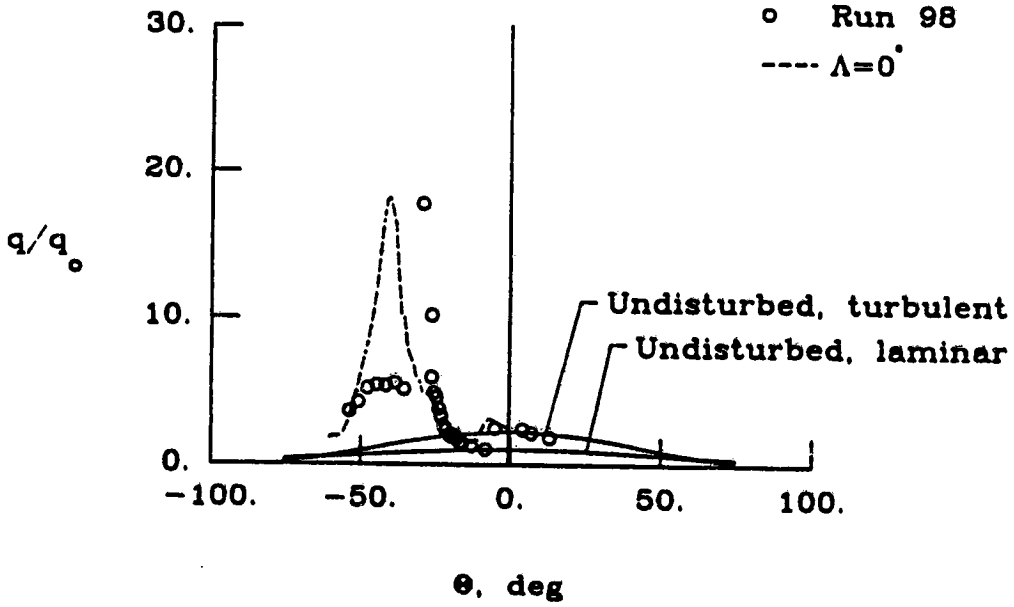

b) Heat transfer rate distribution

Fig. 35. Experimental results for 30° swept interference flowfield (run 98, $Re_1 = 1.467 \times 10^6\ ^1/_{ft}$) compared with unswept results (run 61).

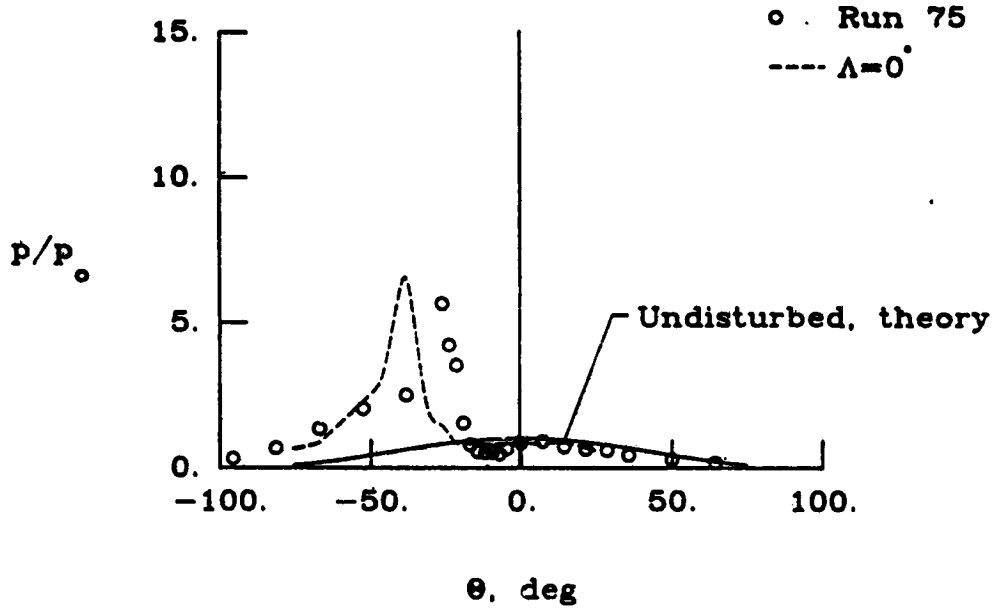

a) Pressure distribution

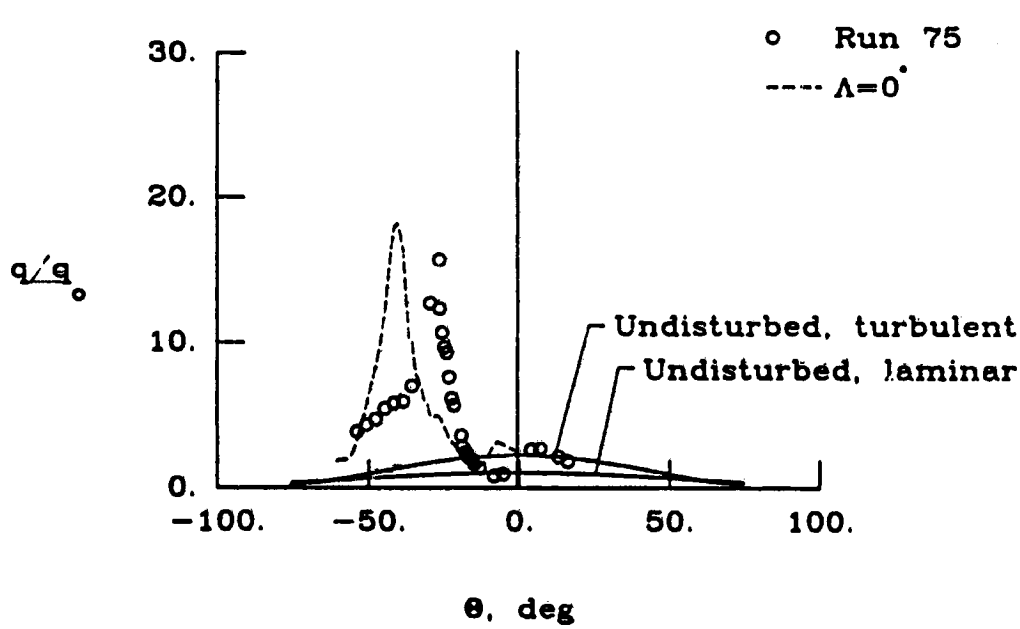

b) Heat transfer rate distribution

Fig. 36. Experimental results for 30° swept interference flowfield (run 75, Re_1 = 1.480 x 10^6 $^1/_{ft}$) compared with unswept results (run 61).

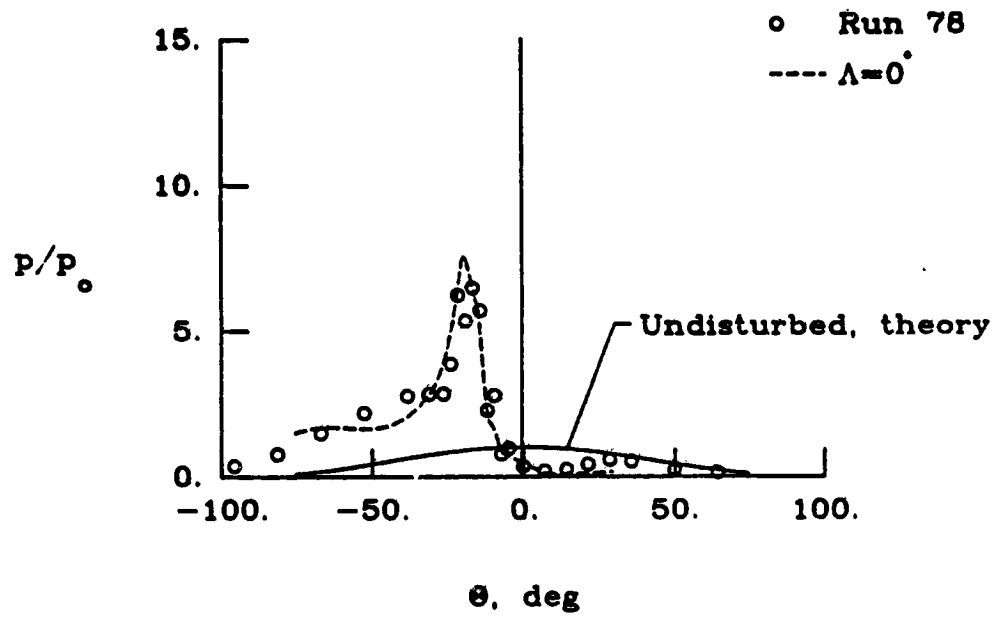

a) Pressure distribution

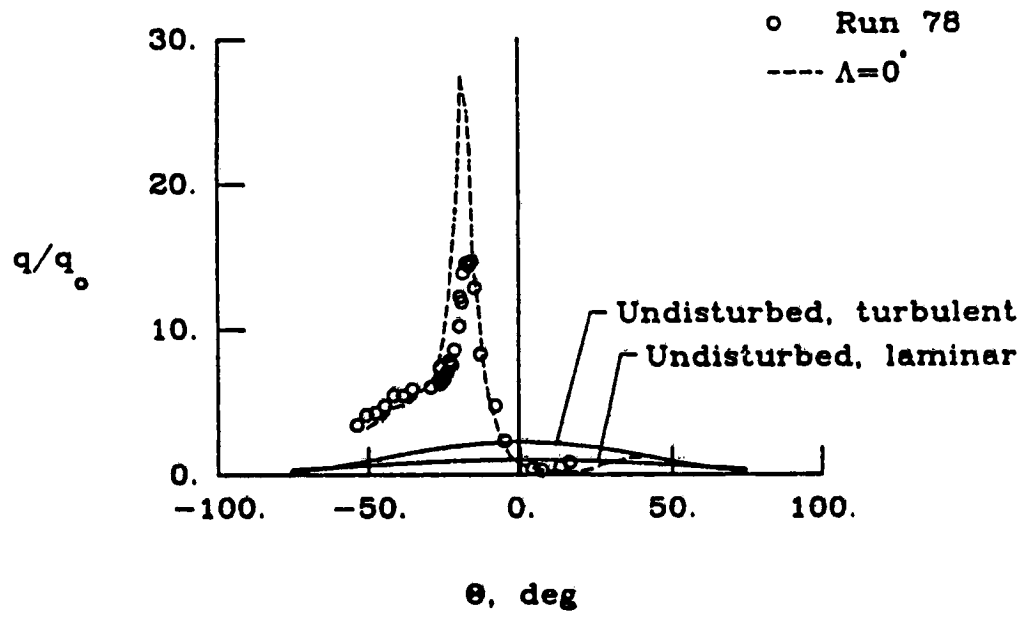

b) Heat transfer rate distribution

Fig. 37. Experimental results for 30° swept interference flowfield (run 78, $Re_1 = 1.484 \times 10^6$ $^1/_{ft}$) compared with unswept results (run 21).

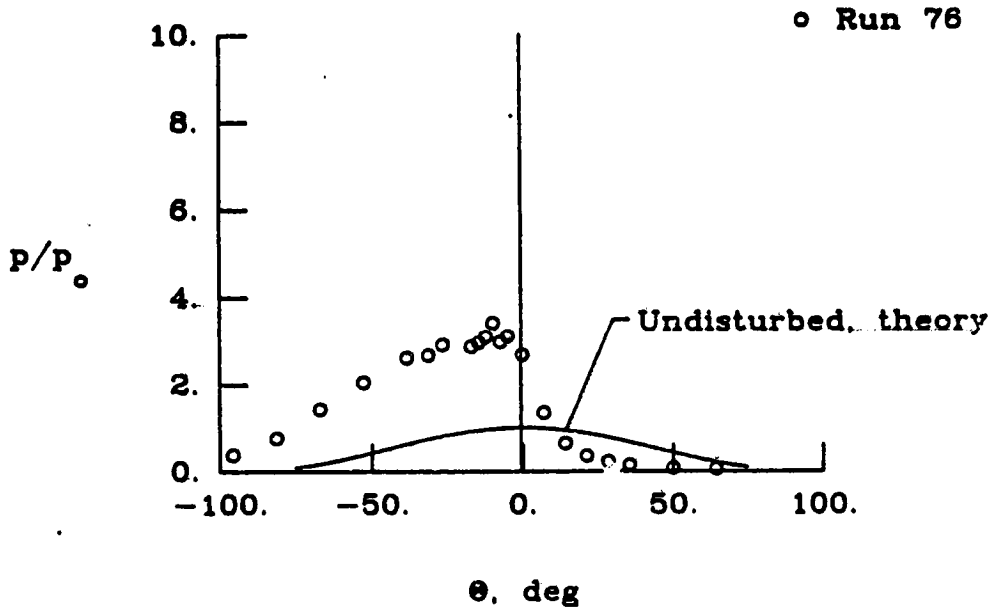

a) Pressure distribution

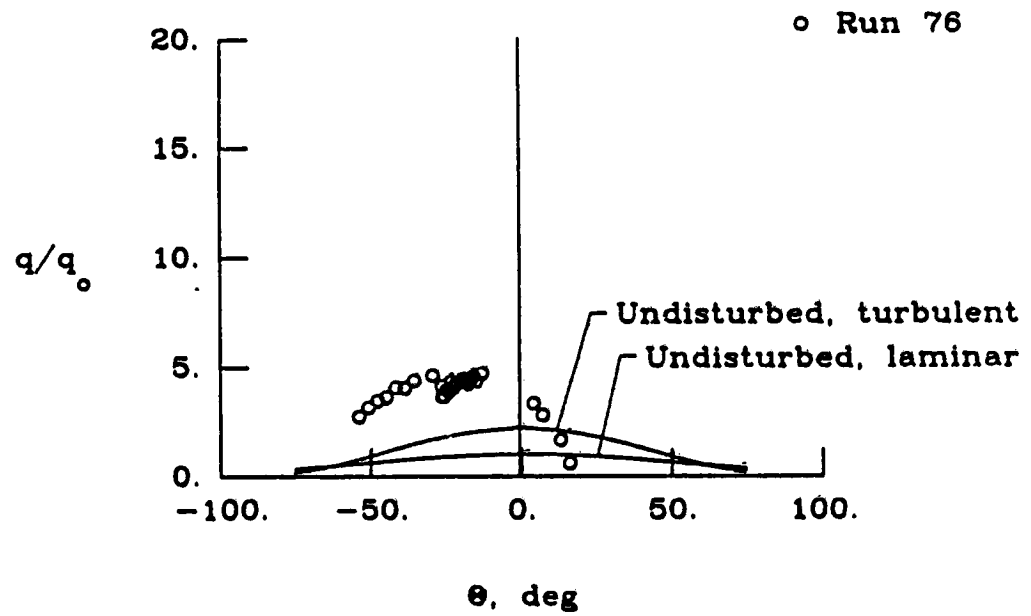

b) Heat transfer rate distribution

Fig. 38. Experimental results for 30° swept interference flowfield (run 76, $Re_1 = 1.454 \times 10^6$ 1/ft).

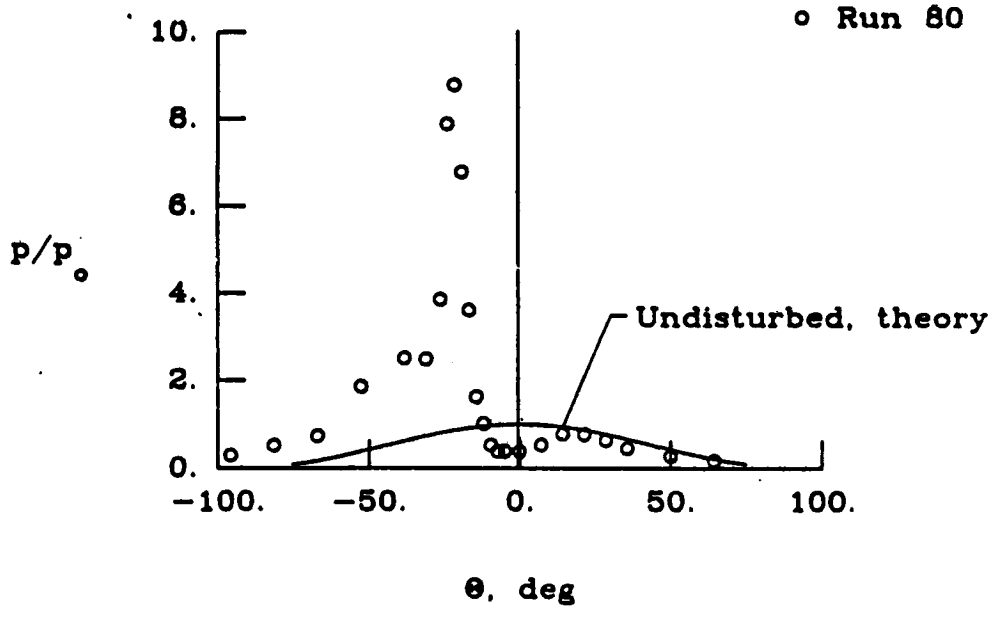

a) Pressure distribution

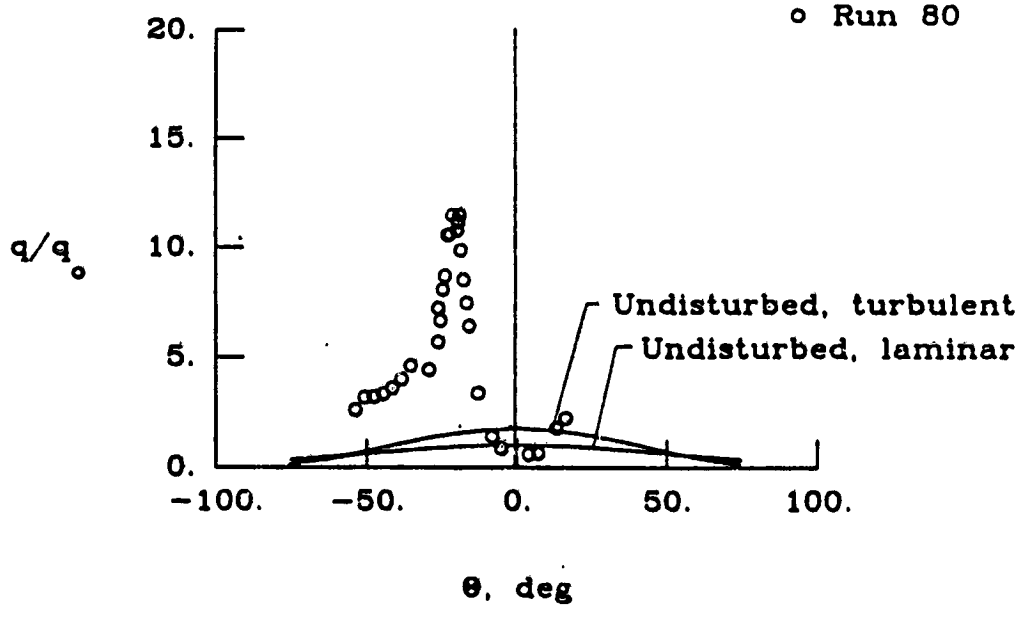

b) Heat transfer rate distribution

Fig. 39. Experimental results for 30° swept interference flowfield (run 80, $Re_1 = 0.715 \times 10^6$ $^1/_{ft}$).

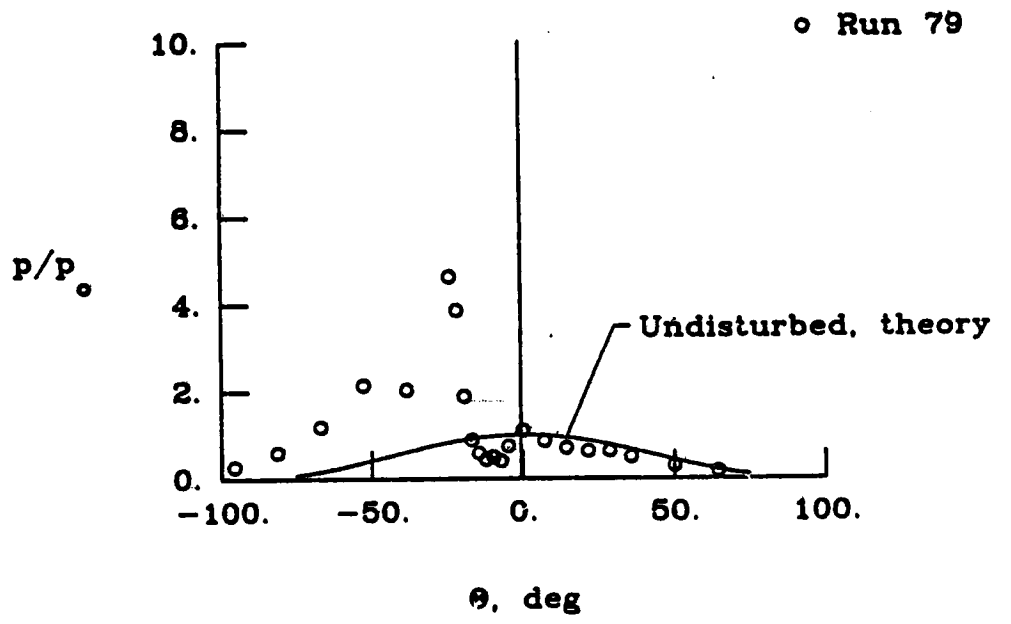

a) Pressure distribution

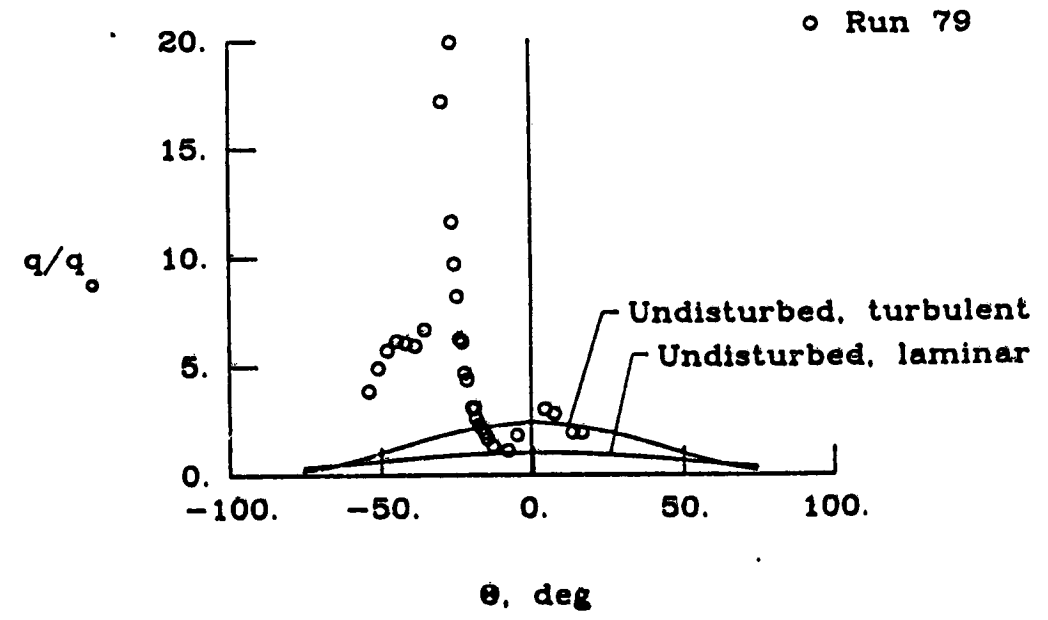

b) Heat transfer rate distribution

Fig. 40. Experimental results for 30° swept interference flowfield (run 79, $Re_1 = 1.830 \times 10^6$ $^1/_{ft}$).

the 30° swept model at the nominal condition cover the range between Type III and Type V shock wave interference.

Chapter 5

CORRELATION OF PEAK PRESSURE AND HEAT TRANSFER RATE

5.1 Peak Pressures and Heat Transfer Rates From Tests at Nominal Conditions

Peak pressures and heat transfer rates from the tests at the nominal conditions with a shock wave interference flowfield are plotted as a locus of peaks in Fig. 41 for the 0°, 15°, and 30° sweep angles. These peaks were taken from the experimental data presented in sections 4.2, 4.3, and 4.4 and tabulated in Appendix B. Peak pressure and heat transfer rate vary depending on the interference type and the associated interaction at the surface. The various interference patterns were obtained by translating the instrumented cylinder with respect to the trailing edge of the incident shock generator. The positions of the cylinder for the various interference tests are given in Table 2.

The pressure and heat transfer rate peaks shown in Figs. 41(a) and 41(b), respectively, show variations in the experimental results because the limited amount of data presented on the figures do not fully describe the locus of peaks. However, a great amount of effort was expended to obtain these limited results. Time and money constraints in the test program did not allow a large number of tests to produce a statistically significant number of tests

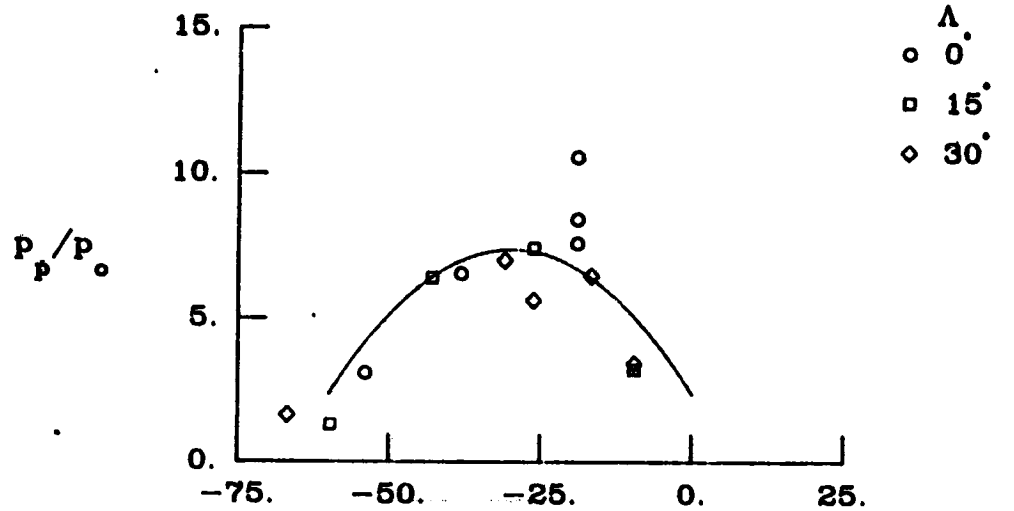

a) Peak pressure

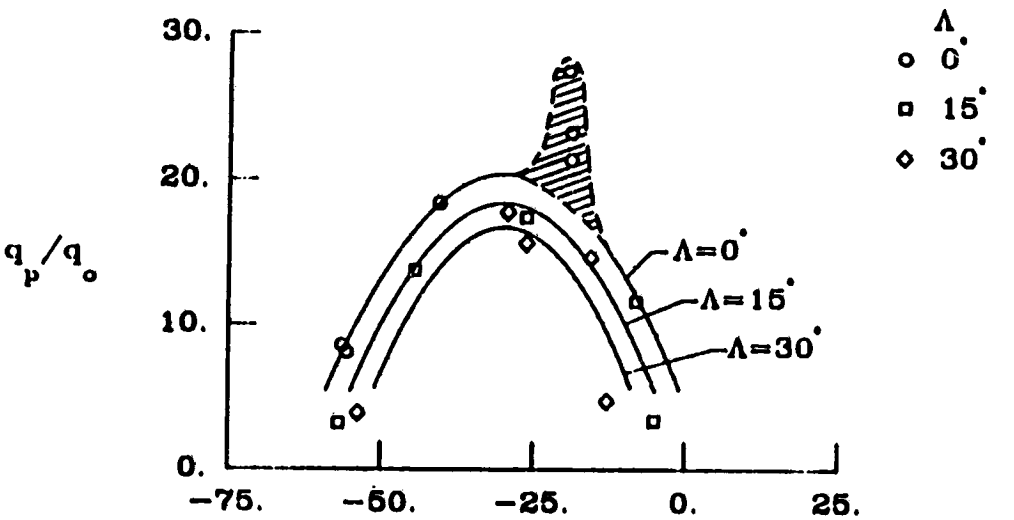

b) Peak heat transfer rate

Fig. 41. Locus of peak pressure and heat transfer rate on the swept shock wave interference model.

which would have described the "actual" locus of peaks from the various types of shock wave interference patterns in detail. However, these limited data do represent a good effort to map out the peak pressures and heat transfer rates produced by the swept shock wave interference model.

An attempt was made to define the locus of peaks with a parabolic least squares curve fit of the data. When individual curves were fit to the pressure data at the three sweep angles, the curves tended to collapse together. Therefore, a single curve was fit through all of the experimental pressure peaks and is shown in Fig. 41(a). Most of the peak pressures shown in the figure follow the trend of the parabolic curve with the exception of three 0° swept peak pressure measurements at $\Theta \approx -20°$. The anomaly at $\Theta \approx -20°$ may be caused by experimental data scatter or, a more probable cause may be normal impingement of the 0° swept supersonic jet from region 8 flow which gives the highest pressure rise. (See Fig. 5.)

The curve fit for the heat transfer rate peaks showed a good correlation at the three sweep angles. Hence, least squares parabolic curves are included with the experimental peak heat transfer rates in Fig. 41(b). The curves show that the peak heat transfer rates decreased as the sweep angle increased. The 0° swept peak heat transfer rates at $\Theta \approx -20°$ were not fit to the curve labeled as $\Lambda = 0°$. These data show that an intense heating level occurred over a narrow region on the cylinder surface which would bias the curve fit upward. The region is shown as a hatched area in the figure. Heat transfer rate in this narrow region is probably caused by normal impingement of the supersonic jet on the surface. The peak heating drops substantially as the jet impingement zone on the surface changes about ± 5° from the normal impingement region. Heating is reduced from an amplification of nearly 30 to an amplification of about 20 times the undisturbed stagnation point level. The

15° and 30° swept results do not show this peak heating region probably because normal impingement of the supersonic jet does not occur on a swept leading edge surface.

Type IV shock wave interference heating is most severe for the 0° swept case at $\Theta \approx 20°$. Supersonic jet impingement also occurs for $\Theta > -15°$, but the jet is turned upward and impinges at low angles or just grazes the surface resulting in lower values. The values for $\Theta < -50°$ are most likely for a Type III (shear layer-boundary layer) or Type II (shock-boundary layer) interference. The parabolic curve fits in Fig. 41(b) show that peak heat transfer rates decreased as the sweep angle increased. However, with increased sweep, the peak pressures did not show the same decrease as the heating because the inviscid features of the shock wave interference pattern at sweep may be similar to those of the unswept case. Hence, the peak pressures are not as sensitive to sweep as the peak heating.

This section presented and discussed the experimental peaks for the various shock wave interference patterns observed at the nominal test condition. The next section presents a discussion of the peak pressures and heat transfer rates for the Type IV supersonic jet impingement tests which were identified in Chapter 4. These peaks were also shown in Fig. 41 at $\Theta \approx -25°$.

5.2 Effect of Sweep on Peak Pressure and Peak Heat Transfer Rate for the Type IV Supersonic Jet Impingement

For undisturbed flow past a swept cylinder, the stagnation pressure varies as $\cos^2\Lambda$ and the stagnation heat transfer rate varies as $\cos^{1.1}\Lambda$ [24]. Therefore, it is postulated that the peak experimental pressure and heat

transfer rate from Type IV supersonic jet impingement will vary with sweep in a similar manner as given by the following relationships:

$$\frac{p_p}{p_o}(\Lambda) = \frac{p_p}{p_o}\Big|_{\Lambda=0°} \cos^2 \Lambda \tag{8}$$

$$\frac{q_p}{q_o}(\Lambda) = \frac{q_p}{q_o}\Big|_{\Lambda=0°} \cos^{1.1} \Lambda \tag{9}$$

Calculations of the inviscid 0° swept Type IV shock wave interference flowfield and resulting peak pressure and heat transfer rates were accomplished using the EASI computer program and the results were presented in Figs. 23-25. For these calculations the computer program used the equilibrium chemically reacting air model. The maximum calculated heat transfer rate occurred for test run 21 as shown in Fig. 23 because the transmitted shock length, L_{ts}, was the shortest for this run. (See Table 3.)

Using the transmitted shock length from run 21, peak pressure and heat transfer rate for region 7 and 8 flow was calculated by the EASI program using both the calorically perfect and equilibrium chemically reacting air models. These calculated values were used in equations (8) and (9) to define the peak pressure and heat transfer rate curves shown on Figs. 42(a) and 42(b), respectively.

Experimental peak pressure for the Type IV interference at the three sweep angles are taken from Fig. 41(a) and plotted in Fig. 42(a). These data are bounded by the pressure ratio curves obtained from equation (8) for region 7 and region 8. The local pressure in region 7 and region 8 are equal to the pressure in the upper and lower bounding subsonic regions, respectively, on either side of the jet and are independent of the jet width. Hence, the

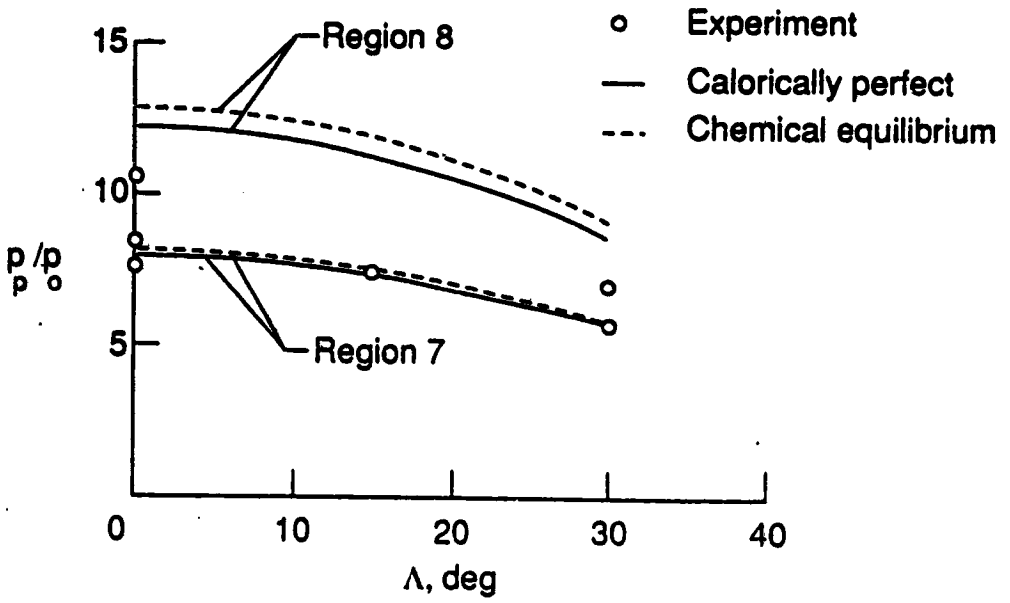

a) Peak pressure

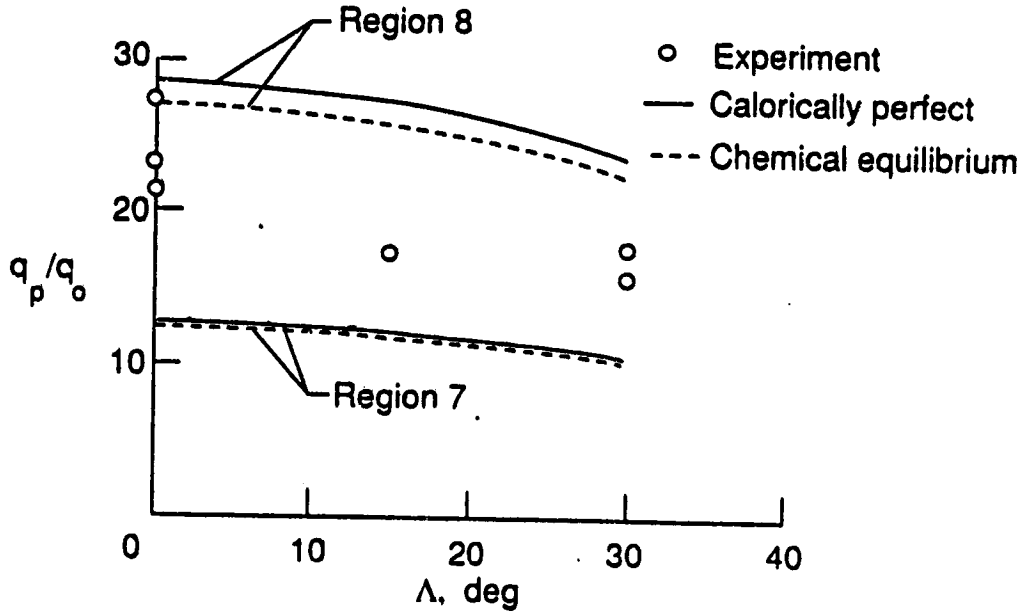

b) Peak heat transfer rate

Fig. 42. Maximum peak pressure and heat transfer rate for Type IV shock wave interference with sweep angle variation.

assumed transmitted shock length has a minimal influence on the lower (region 7) and upper (region 8) bounds because the jet is assumed to terminate through a normal shock at the cylinder surface. Also, these surface pressures are influenced little by jet impingement angle on the surface because the Type IV jet flow is terminated by a strong shock resulting in subsonic flow at the jet impingement point on the surface.

The different bounds for the equilibrium, chemically-reacting gas reflect differences in flow thermodynamic properties and turning angles through the compression waves in the supersonic jet. When the jet flow passes through the weak shock waves, kinetic energy of the air is shared by all internal energy modes of the gas molecules or is going into the energy budget for the chemically reacting products, or both [52]. The vibrational energy modes of the molecules in air become excited at gas temperatures of about 1500°R. Calculations for the present test show gas temperatures of about 2800°R in the jet stagnation region. Therefore, high temperature effects are present for these tests. Note that these effects are significant under these conditions even though the temperature is well below the onset of significant dissociation. (Significant O_2 dissociation occurs around 3600°R [52].)

Similarly, experimental peak heat transfer rates from Fig. 41(b) are plotted in Fig. 42(b) and are bounded by the curves obtained from equation (9). The normalized experimental heat transfer rates lie approximately midway between the curves of region 7 and region 8 and follow the trend expressed by equation (9). Unlike the pressure, the heat transfer rate is influenced strongly by the width of the jet. Jet width controls the velocity gradient along the cylinder in the jet stagnation region. Unfortunately, the jet width is a strong function of the assumed transmitted shock length.

The heat transfer rate bounds defined by region 7 and region 8 (in Fig. 5(a)) for this freestream flow condition are lower for the equilibrium chemically reacting gas. This may be attributed to changes in the wall velocity gradient, thermal layer properties, and compressibility effects. Therefore, high temperature effects on the jet stagnation point heat transfer rate for the present freestream flow condition are significant.

An estimate for the expected range of pressure and heat transfer rate amplification with sweep can be made by using equations (8) and (9), respectively, assuming a transmitted shock length to calculate the 0° swept peak heat transfer rate. In addition, it has been shown that inviscid flow features of the Type IV interference pattern scale directly with the radius of the body [17]. Therefore, for a given set of experimental flow conditions with a Type IV interference, an experimentally obtained two-dimensional transmitted shock length may be scaled with body radius to find an estimate of the expected range of pressure and heat transfer rate with sweep using the method described above. However, as the radius is decreased, the boundary layer becomes a greater percentage of the shock layer, and the scaling effects of the body radius with inviscid flow features may become invalid as the viscous effects dominate the local flow field of the Type IV interference pattern.

Peak pressure and heat transfer rate amplification ratios correlate well as a function of the cosine of the sweep angle as shown in Fig. 42. The reference quantities p_o and q_o can be eliminated from equations (8) and (9) to isolate the effect of sweep on the peak pressure and heat transfer rate and obtain:

$$\frac{p_p}{p_{p|\,\Lambda=0°}} = \cos^4 \Lambda \qquad (10)$$

$$\frac{q_p}{q_{p|\,\Lambda=0°}} = \cos^{2.2}\Lambda \qquad (11)$$

The values for $p_{p|\Lambda=0°}$ and $q_{p|\Lambda=0°}$ were taken from the analysis above as the average calculated stagnation values of region 7 and region 8 at $\Lambda = 0°$. The experimental peak pressure and heat transfer rate were normalized by these values and are shown on Figs. 43(a) and 43(b), respectively. Both the pressure and heat transfer rates normalized in this manner are in good agreement with the cosine function trends. Therefore, normalized peak pressure was reduced about 13 percent and 44 percent, respectively, and normalized peak heat transfer rate was reduced about 7 percent and 27 percent, respectively, at sweep angles of 15° and 30° when compared to the normalized 0° swept values.

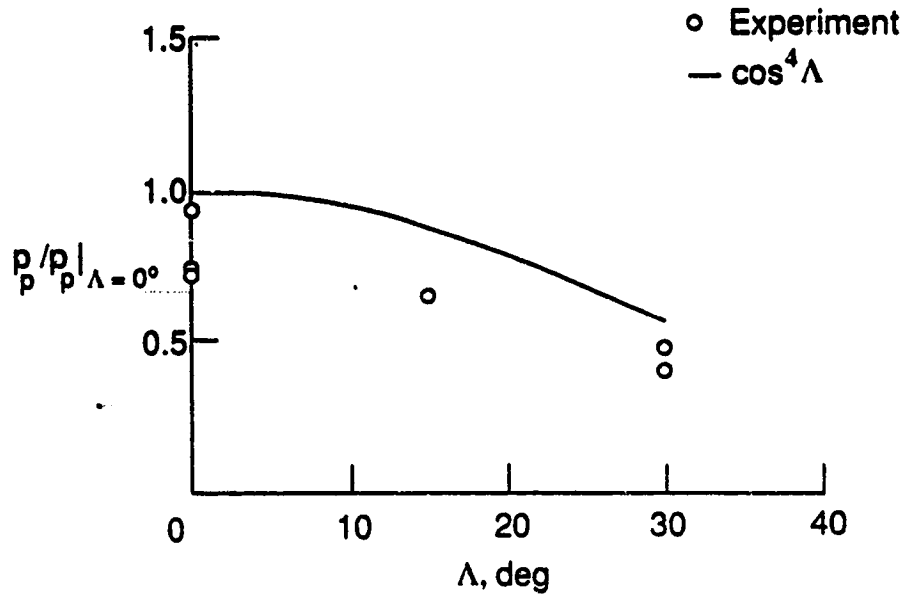

a) Peak pressure

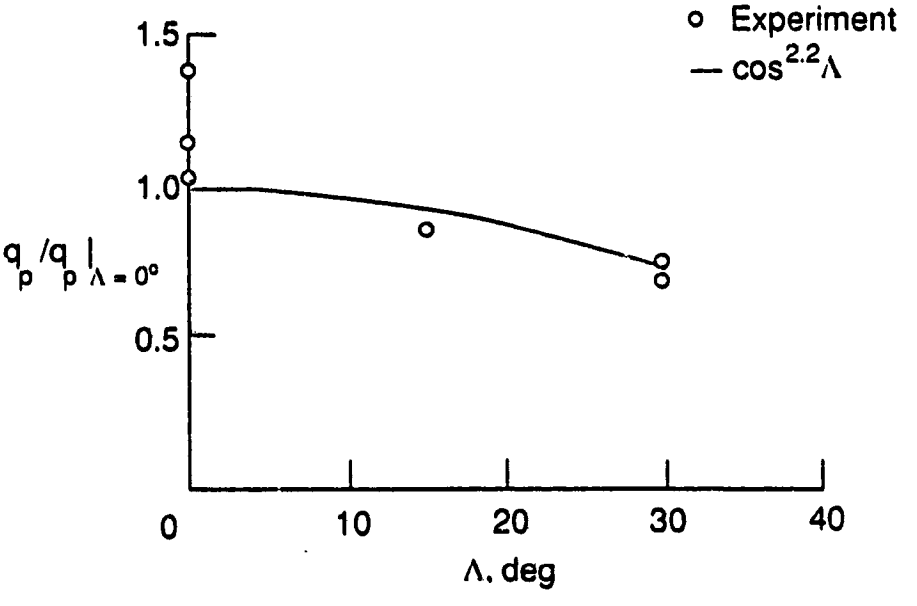

b) Peak heat transfer rate

Fig. 43. Normalized peak pressure and heat transfer rate correlation as a function of the cosine of the sweep angle.

Chapter 6

CONCLUDING REMARKS

6.1 Recapitulation

An experimental study of the effects of leading edge sweep on surface pressure and heat transfer rate for swept shock wave interference has been presented. This study was conducted cooperatively between NASA Langley Research Center and Calspan-University of Buffalo Research Center. Experimental tests were conducted in the Calspan 48-inch Hypersonic Shock Tunnel at a nominal Mach number of 8, nominal Reynolds number of 1.5×10^6 per foot, leading edge and incident shock generator sweep angles of 0°, 15°, and 30°, and incident shock generator angle-of-attack fixed at 12.5°. Detailed surface pressure and heat transfer rate distributions on the cylindrical leading edge of a swept shock wave interference model were measured to determine the region of the maximum surface pressure and heat transfer rates.

6.2 Conclusions

The experimental study shows that pressure and heat transfer rate on the cylindrical leading edge of the shock wave interference model were reduced as the sweep was increased over the range of tested parameters. Peak surface pressure was about 10 times the undisturbed flow, stagnation point

pressure for the 0° sweep test; and peak heat transfer rate was about 30 times the stagnation point heating. Peak pressure and heat transfer rate normalized by the undisturbed stagnation line values vary with the cosine of the sweep angle, Λ. This variation is in the same manner as the undisturbed stagnation pressure and heat transfer rate. When the peak pressure and heat transfer rates are normalized by the peak values at 0° sweep angle, pressure varies as $\cos^4\Lambda$ and heat transfer rate varies as $\cos^{2.2}\Lambda$. A comparison of the 15° swept results with the 0° swept results shows that peak pressure was reduced about 13 percent and peak heat transfer rate was reduced about 7 percent. A comparison of the 30° swept results shows that peak pressure was reduced about 27 percent and peak heat transfer rate was reduced about 44 percent when compared to the 0° swept results.

6.3 Recommendations

The present study has defined the effects of sweep on the pressure and heat transfer rates for a swept shock wave interference model at the nominal test conditions. However, these data are limited in that they are for a single Mach number, single test condition, and single incident shock deflection angle. To define the effects of a swept shock interference more completely, the following recommendations for future research are suggested:

(1) At the nominal test condition, more shock wave interference tests are needed to fully define the locus of peak pressure and heat transfer rate at 0°, 15°, and 30° sweep angle.

(2) More tests at the off nominal Mach 8 conditions are needed to show the effect of Reynolds number variation, especially at lower Reynolds numbers where shear layers are laminar.

(3) The test facility should have the capability of schlieren line of sight along the cylinder axis at sweep angles of 15° and 30° to visualize the swept shock wave interference patterns.

(4) Freestream conditions should include higher Mach number and higher enthalpy flow simulate the true environment of high Mach number flight conditions and show the high temperature effects of dissociation.

(5) Tests on a smaller diameter leading edge are needed to access various effects which are unclear at this time. For example, effects in the jet stagnation point such as Reynolds number scaling based on diameter, viscous dominated shock layer, non-equilibrium flow, and non-continuum flow may be determined.

(6) Future tests should study the effects of incident shock impingement on a compound swept and diagonal leading edge which may represent a more realistic shock wave interference on the scramjet cowl.

(7) Flight testing of a swept cowl leading edge model on flight test vehicles such as the Hypersonic Flight and Instrumentation Research Experiments (HYFIRE) project will show effects of high Mach number flight. HYFIRE is expected to reach Mach 16 flight conditions using ground launched missiles.

(8) Development of a three-dimensional pressure-deflection-sweep diagram, similar to the two-dimensional heart-diagram, may yield a more complete understanding of the physics of various swept shock wave interference patterns.

(9) Three-dimensional computational fluid dynamics computer programs can be validated using the results from this study.

Finally, it is hoped that these experiments have contributed to a better understanding of shock wave interference heating phenomena at hypersonic speeds.

REFERENCES

1. Watts, Joe D.: "Flight Experience with Shock Impingement and Interference Heating on the X-15-2 Research Airplane," NASA TM X-1669, October 1968.

2. Burcham, Frank W., Jr. and Nugent, Jack: "Local Flow Field Around a Pylon-Mounted Dummy Ramjet Engine on the X-15-2 Airplane for Mach Numbers From 2.0 to 6.7," NASA TN D-5638, February 1970.

3. Edney, Barry: "Anomalous Heat Transfer and Pressure Distributions on Blunt Bodies at Hypersonic Speeds in the Presence of an Impinging Shock," FFA Report 115, The Aeronautical Research Institute of Sweden, February 1968.

4. Thornton, Earl A. and Dechaumphai, Promote: "A Taylor-Galerkin Finite Element Algorithm for Transient Nonlinear Thermal-Structural Analysis," AIAA Paper 86-0911 CP, May 1986.

5. Edney, Barry E.: "Shock Interference Heating and the Space Shuttle," NASA TM X-52876, Vol I, July 15-17, 1970, pp. 338-389.

6. Edney, B. E.; Bramlette, T. T.; Ives, J.; Hains, F. D.; and Keyes, J. W.: "Theoretical & Experimental Studies of Shock Interference Heating," Report No. 9500-920-195, Bell Aerospace Company, October 1970.

7. Anon.: "Investigation of Shock Wave Impingement and Interaction During Space Shuttle Flight Maneuvers," LMSC/HREC D162772, Technical Brief, Lockheed Missiles & Space Company, February 8, 1971.

8. Wieting, Allan R.; Thareja, Rajiv R.; Stewart, James R. and Morgan, Ken: "Inviscid Analysis of Shock Wave Interference on a Cylindrical Leading Edge," Third National Aero-Space Plane Technology Symposium, June 2-4, 1987, Paper Number 87.

9. Wieting, Allan R.: "Experimental Study of Shock Wave Interference Heating on a Cylindrical Leading Edge," Ph. D. Dissertation, Old Dominion University, Norfolk, Virginia, May 1987. (Also available as NASA TM 100484, May 1987.)

10. Wieting, Allan R. and Holden, Michael S.: "Experimental Study of Shock Wave Interference Heating on a Cylindrical Leading Edge at Mach 6 and 8," AIAA Paper 87-1511, June 1987.

11. Holden, Michael S.; Wieting, Alan R.; and Glass, Christopher: "Experimental Study of Shock Wave Interference Heating on a Cylindrical Leading Edge," Third National Aero-Space Plane Technology Symposium, June 2-4, 1987.

12. Holden, M. S.; Wieting, A. R.; Moselle, J. R.; and Glass, C.: "Studies of Aerothermal Loads Generated in Regions of Shock/Shock Interaction in Hypersonic Flow," AIAA Paper 88-0477, January 1988.

13. Morgan, K.; Peraire, J.; Thareja, R. R.; and Stewart, J. R.: "An Adaptive Finite Element Scheme for Euler and Navier-Stokes Equations," AIAA Paper 87-1172-CP, June 1987.

14. Thareja, R. R.; Stewart, J. R.; Hassan, O.; Morgan, K.; and Peraire, J.: "A Point Implicit Unstructured Grid Solver for the Euler and Navier-Stokes Equations," AIAA Paper 88-0036, January 1988.

15. Klopfer, G. H. and Yee, H. C.: "Viscous Hypersonic Shock-On-Shock Interaction on Blunt Cowl Lips," AIAA Paper 88-0233, January 1988.

16. Stewart, James R.; Thareja, Rajiv R.; Wieting, Allan R.; and Morgan, Ken: "Application of Finite Element and Remeshing Technique to Shock Interference on a Cylindrical Leading Edge," AIAA Paper 88-0368, January 1988.

17. Wieting, Allan R.; Thareja, Rajiv R.; Stewart, James R. and Morgan, Ken: "Viscous Hypersonic Unstructured Grid Computation of Shock-on-Shock Interaction on Blunt Cowl Lips," Fourth National Aero-Space Plane Technology Symposium, February 16-19, 1988, Paper Number 66.

18. Dechaumphai, Pramote; Thornton, Earl A.; and Wieting Allan R.: "Flow-Thermal-Structural Study of Aerodynamically Heated Leading Edges," AIAA Paper 88-2245-CP, April 1988. (Also available as NASA TM 100579, April 1988.)

19. Thareja, Rajiv R.; Morgan, Ken; Peraire, Jaime; and Peiro, Joaquin: "A Three-Dimensional Upwind Finite Element Point Implicit Unstructured Grid Euler Solver," AIAA Paper 89-0658, January 1989.

20. Hassan, O.; Morgan, K.; and Peraire, J.: "An Adaptive Implicit/Explicit Finite Element Scheme for Compressible Viscous High Speed Flows," AIAA Paper 89-0363, January 1989.

21. Beckwith, Ivan E.: "Theoretical Investigation of Laminar Heat Transfer on Yawed Infinite Cylinders in Supersonic Flow and a Comparison with Experimental Data," NACA RM L55F09, August 1955.

22. Beckwith, Ivan E.: "Similar Solutions for the Compressible Boundary Layer on a Yawed Cylinder With Transpiration Cooling," NASA TR R-42, 1959.

23. Reshotko, Eli: "Heat Transfer to a Yawed Infinite Cylinder in Compressible Flow," Heat Transfer and Fluid Mechanics Institute Preprints of Papers, held at Stanford University, June 21-23, 1956, pp. 205-220.

24. Beckwith, Ivan E.; and Gallagher, James J.: "Local Heat Transfer and Recovery Temperatures on a Yawed Cylinder at a Mach Number of 4.15 and High Reynolds Numbers," NASA TR R-104, 1961.

25. Gollnick, A. F., Jr.: "Heat-Transfer and Pressure Distributions on a Blunt Swept Leading Edge Including the Effects of Upstream Vorticity," NWC-TP-4479, Naval Weapons Center, China Lake, California, January 1968.

26. Glass, Christopher E.; Holden, Michael S.; and Wieting, Allan R.: "Effect of Leading Edge Sweep on Shock-Shock Interference at Mach 8," AIAA Paper 89-0271, January 1989.

27. Ryan, B. M.: "Summary of the Aerothermodynamic Interference Literature," Technical Note 4061-160, Naval Weapons Center, China Lake, California, April 1969.

28. Korkegi, Robert H.: "Survey of Viscous Interactions Associated with High Mach Number Flight," *AIAA Journal*, Vol. 9, No. 5, May 1971, pp. 771-784.

29. Newlander, Robert A.: "Effect of Shock Impingement on the Distribution of Heat-Transfer Coefficients on a Right Circular Cylinder at Mach Numbers of 2.65, 3.51, and 4.44," NASA TN D-642, January 1961.

30. Beckwith, Ivan E.: "Experimental Investigation of Heat Transfer and Pressures on a Swept Cylinder in the Vicinity of Its Intersection with a Wedge and Flat Plate at Mach Number 4.15 and High Reynolds Numbers," NASA TN D-2020, July 1964.

31. Jones, Robert A.: "Heat-Transfer and Pressure Investigation of a Fin-Plate Interference Model at a Mach Number of 6," NASA TN D-2028, July 1964.

32. Knox, E. C.: "Measurements of Shock-Impingement Effects on the Heat-Transfer and Pressure Distributions on a Hemicylinder Model at Mach Number 19," AEDC-TR-65-245, November 1965.

33. Bushnell, Dennis M.: "Interference Heating on a Swept Cylinder in Region of Intersection with a Wedge at Mach Number 8," NASA TN D-3094, December 1965.

34. Gulbran, C. E.; Redeker, E.; Miller, D. S.; and Strack, S. L.: "Heating in Regions of Interfering Flow Fields, Part II: Leading Edge Shock Impingement," AFFDL-TR-65-49, Part II, The Boeing Company, January 1967.

35. Hiers, Robert S. and Loubsky, William J.: "Effects of Shock-Wave Impingement on the Heat Transfer on a Cylindrical Leading Edge," NASA TN D-3859, February 1967.

36. Bushnell, Dennis M.: "Effects of Shock Impingement and Other Factors on Leading-Edge Heat Transfer," NASA TN D-4543, April 1968.

37. Craig, Roger R. and Ortwerth, Paul J.: "Experimental Study of Shock Impingement on a Blunt Leading Edge with Application to Hypersonic Inlet Design," AFAPL Report TR-71-10, April 1971.

38. Keyes, J. Wayne and Morris, Dana J.: "Correlations of Peak Heating in Shock Interference Regions at Hypersonic Speeds," *Journal of Spacecraft and Rockets*, Engineering Notes, Vol. 9, No. 8, August 1972, pp. 621-623.

39. Birch, Stanley F. and Keyes, J. Wayne: "Transition In Compressible Free Shear Layers," *Journal of Spacecraft and Rockets*, Engineering Notes, Vol. 9, No. 8, August 1972, pp. 623-624.

40. Hains, Frank D. and Keyes, J. Wayne: "Shock Interference Heating in Hypersonic Flows," *AIAA Journal*, Vol. 10, No. 11, November 1972, pp. 1441-1447.

41. Keyes, J. Wayne and Hains, Frank D.: "Analytical and Experimental Studies of Shock Interference Heating in Hypersonic Flows," NASA TN D-7139, May 1973.

42. Morris, Dana J. and Keyes, J. Wayne: "Computer Programs for Predicting Supersonic and Hypersonic Interference Flow Fields and Heating," NASA TM X-2725, May 1973.

43. Crawford, Davis H.: "A Graphical Method for the Investigation of Shock Interference Phenomena," *AIAA Journal*, Technical Notes, Vol. 11, No. 11, November 1973, pp. 1590-1592.

44. Bramlette, T. Taz: "Simple Technique for Predicting Type III and Type IV Shock Interference," *AIAA Journal*, Technical Notes, Vol. 12, No. 8, August 1974, pp. 1151-1152.

45. Tannehill, J. C.; Holst, T. L.; and Rakich, J. V.: "Numerical Computation of Two-Dimensional Viscous Blunt Body Flows With an Impinging Shock," *AIAA Journal*, Vol. 14, No. 2, February 1976, pp. 204-211.

46. Tannehill, J. C.; Holst, T. L.; Rakich, J. V.; and Keyes, J. W.: "Comparison of a Two-Dimensional Shock Impingement With Experiment," *AIAA Journal*, Technical Notes, Vol. 14, No. 4, April 1976, pp. 539-541.

47. Keyes, J. Wayne: NASA Langley Research Center, Private Communications, March 1989.

48. Anderson, John D., Jr.: *MODERN COMPRESSIBLE FLOW With Historical Perspective*, McGraw-Hill Book Co., New York, 1982.

49. Schlichting, Hermann: *Boundary-Layer Theory*, Seventh Edition, McGraw-Hill Book Co., New York, 1979.

50. Shapiro, Ascher H.: *The Dynamics and Thermodynamics of COMPRESSIBLE FLUID FLOW, Vols. I and II*, The Ronald Press Co., New York, 1954.

51. Cox, R. N. and Crabtree, L. F.: *Elements of Hypersonic Aerodynamics*, Academic Press, Inc., New York, 1965.

52. Anderson, John D., Jr.: *Hypersonic and High Temperature Gas Dynamics*, McGraw-Hill Book Co., New York, 1989.

53. Markarian, C. Franklyn: "Heat Transfer in Shock Wave-Boundary Layer Interaction Regions," NWC TP 4485, Naval Weapons Center, China Lake, California, November 1968.

54. Back, L. H. and Cuffel, R. F.: "Changes in Heat Transfer from Turbulent Boundary Layers Interacting with Shock Waves and Expansion Waves," *AIAA Journal*, Technical Notes, Vol. 8, No.10, October 1970, pp. 1871-1873.

55. Holden, M. S.: "Shock Wave-Turbulent Boundary Layer Interaction in Hypersonic Flow," AIAA Paper 72-74, January 1972.

56. Johnson, Charles B. and Kaufman, Louis G., II: "Interference Heating From Interactions of Shock Waves With Turbulent Boundary Layers at Mach 6," NASA TN D-7649, September 1974.

57. Kaufman, Louis G., II and Johnson, Charles B.: "Weak Incident Shock Interactions With Mach 8 Laminar Boundary Layers," NASA TN D-7835, December 1974.

58. Holden, M. S.: "A Study of Flow Separation in Regions of Shock Wave-Boundary Layer Interaction in Hypersonic Flow," AIAA Paper 78-1169, July 1978.

59. Bushnell, Dennis M. and Weinstein, Leonard M.: "Correlation of Peak Heating for Reattachment of Separated Flows," *Journal of Spacecraft and Rockets*, Engineering Notes, Vol. 5, No. 9, September 1968, pp. 1111-1112.

60. Fay, J. A. and Riddell, F. R.: "Theory of Stagnation Point Heat Transfer in Dissociated Air," *Journal of the Aeronautical Sciences*, Vol. 25, No. 2, February 1958.

61. Van Dyke, Milton D. and Gordon, Helen D.: "Supersonic Flow Past a Family of Blunt Axisymmetric Bodies," NASA TR R-1, 1959.

62. Hayes, Wallace D. and Probstein, Ronald F.: *Hypersonic Flow Theory, Vol. I - Inviscid Flows*, Second Edition, Academic Press, New York, 1966.

63. Anon.: "Hypersonic Shock Tunnel Description and Capabilities," Calspan Corporation, June 1986.

64. Dunn, M. G.; Rae, W. J.; and Holt, J. L.: "Measurement and Analyses of Heat Flux Data in a Turbine Stage: Part I-Description of Experimental Apparatus and Data Analysis," *Journal of Engineering for Gas Turbines and Power*, Vol. 106, January 1984, pp. 229-233.

65. Miller, Charles G., III: "Comparison of Thin-Film Resistance Heat-Transfer Gages With Thin-Skin Transient Calorimeter Gages in Conventional Hypersonic Wind Tunnels," NASA TM 83197, December 1981.

66. Carnahan, Brice; Luther, H. A.; and Wilkes, James O.: *Applied Numerical Methods*, John Wiley & Sons, Inc., New York, 1969.

67. Carslaw, H. S. and Jaeger, J. C.: *Conduction of Heat in Solids*, Second Edition, Oxford University Press, London, 1959.

68. Prabhu, Ramadas K. and Erickson, Wayne D.: "A Rapid Method for the Computation of Equilibrium Chemical Composition of Air to 15 000 K," NASA TP 2792, March 1988.

69. Lamb, Milton and Stallings, Robert L., Jr.: "Heat-Transfer Distributions on a 0.013-Scale Shuttle Solid Rocket Booster at Mach 3.70 and Angles of Attack From 0° to 180°," NASA TM X-3417, November 1976.

Appendix A

METHOD OF HEAT TRANSFER RATE CALCULATION

Heat transfer rates on the swept shock wave interference model were determined from the temperature-time histories of the thin-film constant current platinum thermometers. Since the platinum film was fused to the (pyrex 7740) substrate, it was assumed that the film behaved as a perfect conductor. Using this assumption, the measured temperature-time histories of the gauges equated to the surface temperature of the pyrex substrate. Furthermore, Wieting has shown previously [9] that the pyrex behaves as a one-dimensional semi-infinite solid whose backside temperature remains constant during the 15 millisecond shock tunnel test.

The Calspan heat transfer data reduction method is called the "Rae-Taulbee method" and is based on the solution for one-dimensional heat transfer with variable thermal properties. Carslaw and Jaeger [67] express the equation as:

$$\rho c_p \frac{\partial T}{\partial t} = \frac{\partial}{\partial x}\left(k \frac{\partial T}{\partial x}\right) \qquad \text{(A1)}$$

This nonlinear equation is transformed to a linear heat conduction equation by the Kirchoff transformation [67] given by:

$$\phi(x,t) = \int_{T_{ref}}^{T} \frac{k}{k_{ref}}\, dT \qquad \text{(A2)}$$

Applying equation (A2) to (A1) and using the definition of thermal diffusivity, $\alpha=k/\rho c_p$, equation (A1) is written as:

$$\frac{\partial \phi}{\partial t} = \alpha(\phi) \frac{\partial^2 \phi}{\partial x^2} \qquad \text{(A3)}$$

Likewise, Fourier's law of heat conduction,

$$q = -k \frac{\partial T}{\partial x} \qquad \text{(A4)}$$

is transformed using equation (A2) to give:

$$q = -k_{ref} \frac{\partial \phi}{\partial x} \qquad \text{(A5)}$$

The solution of equation (A3) by an appropriate numerical technique to find $\phi(x,t)$ will yield the surface heat transfer rate by applying equation (A5) at the pyrex surface.

The thermophysical properties of the pyrex 7740 used in the Calspan experiments have been measured over a range of temperatures and are given by Miller [65] as:

$$k = 1.51458 \times 10^{-2} - 5.90677 \times 10^{-5} T + 1.81645 \times 10^{-7} T^2 \quad \text{W/cm-K} \qquad \text{(A6a)}$$

$$c_p = -8.54140 \times 10^{-2} + 4.28391 \times 10^{-3} T - 5.74819 \times 10^{-6} T^2 + 3.10468 \times 10^{-9} T^3 \quad \text{W-sec/g-K} \qquad \text{(A6b)}$$

with

$$\rho = 2.227\ g/cm^3 = \text{constant} \tag{A6c}$$

over the range of temperature (in degrees K) 297 K < T < 600 K. Thermal diffusivity, $\alpha=\alpha(\phi)$, can be obtained at the appropriate temperature T(x,t) corresponding to $\phi=\phi(x,t)$ using equations (A2) and (A6).

The basis for the heat transfer data reduction technique is given in the discussion above. Specific details of the formulation used in the data reduction computer program are discussed next.

The numerical solution of equation (A3) is performed in a stretched coordinate system using a finite difference scheme. The stretched coordinate system is useful because variation of temperature in the pyrex occurs over a uniform range for all times and regridding in the finite difference scheme is not necessary [64]. The stretched coordinate system is given as:

$$\eta = \frac{x}{2\sqrt{\alpha_{ref} t}} \tag{A7a}$$

$$t = \tau \tag{A7b}$$

and therefore

$$\phi = \phi\,[\eta(x,t),\tau(t)] \tag{A8}$$

in the stretched coordinate system. Equation (A3) is transformed into the stretched coordinate system given by equation (A7) and takes the form:

$$\frac{\alpha}{\alpha_{ref}} \frac{\partial^2 \phi}{\partial \eta^2} + 2\eta \frac{\partial \phi}{\partial \eta} = 4\tau \frac{\partial \phi}{\partial \tau} \qquad \text{(A9)}$$

A Crank-Nicolson finite difference formulation of the partial differential equation given by equation (A9) was employed. The boundary condition at the upper surface is given as:

$$\phi(\eta = 0, \tau) = \int_{T_{ref}}^{T(x=0,t)} dT \qquad \text{(A10a)}$$

and at the rear surface the boundary condition is:

$$\phi(\eta = 5, \tau) = 0 \qquad \text{(A10b)}$$

The initial condition is given by:

$$\phi(\eta, \tau = 0) = 0 \qquad \text{(A10c)}$$

The Crank-Nicolson formulation of equation (A9) yields:

$$\left[\frac{\alpha}{\alpha_{ref}} + \eta\Delta\eta\right]\phi_{i+1}^{j+1} + \left[-\frac{8\Delta\eta^2\tau}{\Delta\tau} - 2\frac{\alpha}{\alpha_{ref}}\right]\phi_i^{j+1} + \left[\frac{\alpha}{\alpha_{ref}} - \eta\Delta\eta\right]\phi_{i-1}^{j+1}$$

$$= -\frac{\alpha}{\alpha_{ref}}\left[\phi_{i-1}^{j} - 2\phi_i^{j} + \phi_{i+1}^{j}\right] - \eta\Delta\eta\left[\phi_{i-1}^{j} + \phi_{i+1}^{j}\right] - \frac{8\Delta\eta^2\tau}{\Delta\tau}\phi_i^{j} \qquad \text{(A11)}$$

where the subscripts refer to space and the superscripts refer to time.

Equation (A11) is in the form:

$$A_i^j \phi_{i+1}^{j+1} + B_i^j \phi_i^{j+1} + C_i^j \phi_{i-1}^{j+1} = D_i^j \qquad \text{(A12)}$$

where the left-hand side involves values of ϕ at time j+1, and the right-hand side involves ϕ at time j. The matrix of coefficients A, B, C, and D are a tridiagonial system of equations, and Thomas' algorithm [66] is used to solve this system of equations. The solution takes the form:

$$\phi_i^{j+1} = G_i^{j+1} + H_i^{j+1}\phi_{i+1}^{j+1} \qquad \text{(A13)}$$

where

$$G_i^{j+1} = \frac{D_i^j - C_i^j G_{i-1}^{j+1}}{B_i^j + C_i^j H_{i-1}^{j+1}} \qquad \text{(A14a)}$$

and

$$H_i^{j+1} = \frac{-A_i^j}{B_i^j - C_i^j H_{i-1}^{j+1}} \qquad \text{(A14b)}$$

Given the boundary condition at the upper surface, i = 1, which is known from the temperature-time history of the platinum thermometer, and the solution at time step j, ϕ at time step j+1 is solved using equation (A14).

The procedure advances in time as follows: At the surface where i = 1 and at time step j+1,

$$\phi_1^{j+1} = G_1^{j+1} + H_1^{j+1} \phi_2^{j+1} \qquad \text{(A15)}$$

from equation (A13). Equation (A15) is always satisfied if

$$G_1^{j+1} = \phi_1^{j+1} \qquad \text{(A16a)}$$

and

$$H_1^{j+1} = O \qquad \text{(A16b)}$$

The solution for G_{j+1} and H_{j+1} are advanced in space from i = 2, 3, 4, ..., I. Then ϕ^{j+1} is solved in the opposite spatial direction, i. e., i = I, I-1, I-2, ..., 3, 2, 1. The solution at the backside is known from the constant temperature wall condition, equation (A10b), ϕ_I=0 for all time steps j.

The heat transfer rate at the surface is obtained using equation (A5) which is approximated by:

$$q = -k_{ref} \frac{1}{2\sqrt{\alpha_{ref}\tau}} \left[\frac{-3\phi_1^j + 4\phi_2^j - \phi_3^j}{2\Delta\eta} \right] \qquad \text{(A17)}$$

Also, this solution procedure required an initial temperature profile for ϕ after the first time step, j=1. This was accomplished using an analytic solution to the transient heat conduction equation with constant properties and a constant heat flux at the front surface. That solution is given by Carslaw and Jaeger [67] and is repeated here for completeness.

$$T(x,1) = \frac{2q}{k} \left[\left(\frac{\alpha t}{\pi}\right)^{1/2} e^{-\left(\frac{x2}{4\alpha t}\right)} - \frac{x}{2} \operatorname{erfc}\left(\frac{x}{2\sqrt{\alpha t}} \right) \right] \qquad \text{(A18a)}$$

where the surface heat flux was given as:

$$q = \frac{k\left[T(1,1) - T_{ref}\right]}{2\left(\frac{\alpha t}{\pi}\right)^{1/2}} \qquad \text{(A18b)}$$

Appendix B

SURFACE HEAT TRANSFER RATE AND PRESSURE TABULATION

Experimental data presented in this study are tabulated in this appendix. The heat transfer rates and pressures are normalized by the values given as q_o and p_o, respectively, which are the calculated stagnation line values. The angular position Θ is the circumferential location on the instrumented cylinder where the measurement was taken. These Θ values are tabulated in columns 2 and 7 in the tables for the heat transfer rate and pressure data, respectively. The most negative Θ value is the lowest gauge position on the bottom of the cylinder, and the most positive Θ is the most upper location. The measurements which correspond to $\Theta = 0°$ are at the stagnation line with respect to the freestream flow direction. Heat transfer rates are presented in columns 4 and 5 and correspond to the Θ values in column 2. The heat transfer rate values given in column 4, q_{hw}/q_o, are the hot wall values which correspond to the adjacent surface temperatures given in column 3; and the values given in column 5, q/q_o, have been adjusted to a cold wall temperature of 530°R. The experimental pressures presented in this study are given in column 8 and correspond to the Θ values which are given in column 7 in the tables.

Experimental Data for Run 21

Heat Transfer Rate $q_o = 41.907$ Btu/ft²-sec					Pressure $p_o = 10.757$ psia		
gauge	Θ deg	Tw °R	q_{hw}/q_o	q/q_o	gauge	Θ deg	p/p_o
53	-53.77	648.0	2.71	2.86	1	-95.49	0.42
54	-50.72	657.7	2.94	3.11	5	-66.85	1.67
55	-47.66	669.9	3.29	3.51	10	-31.04	2.75
56	-44.61	676.8	3.56	3.81	12	-21.49	6.33
57	-41.55	697.8	4.18	4.52	17	-19.10	7.61
58	-38.50	709.4	4.35	4.73	13	-16.71	6.61
59	-35.44	715.9	4.62	5.04	18	-14.32	5.44
61	-29.33	751.5	5.71	6.33	14	-11.94	2.41
62	-26.27	816.7	8.20	9.40	19	-9.55	1.71
1	-26.27	797.5	6.76	7.67	15	-7.16	0.93
2	-25.47	816.7	7.51	8.61	20	-4.77	0.69
3	-24.67	833.9	8.16	9.43	22	7.16	0.11
4	-23.87	872.8	9.31	10.98	23	14.32	0.06
5	-23.07	900.9	10.24	12.25	24	21.49	0.09
6	-22.28	925.4	11.79	14.30	25	28.65	0.13
7	-21.49	915.4	10.43	12.58	26	35.81	0.23
9	-19.88	1013.0	17.23	21.91	28	50.13	0.24
71	-19.58	1060.0	20.94	27.36			
10	-19.08	1030.0	18.54	23.81			
69	-17.67	1051.0	19.85	25.80			
68	-16.71	1045.0	19.01	24.62			
67	-15.76	1011.0	16.18	20.56			
66	-14.80	928.7	11.06	13.43			
65	-13.85	926.7	10.48	12.71			
64	-12.89	889.3	8.93	10.62			
63	-11.94	855.8	7.04	8.23			
24	-8.12	720.2	3.62	3.95			
25	-5.06	638.3	1.98	2.09			
28	4.11	558.6	0.46	0.46			
29	7.16	553.9	0.28	0.29			
30	10.22	546.3	0.17	0.17			
31	13.27	543.6	0.17	0.17			
32	16.33	544.7	0.12	0.12			
34	16.33	540.0	0.12	0.12			
36	22.93	546.4	0.29	0.29			
37	26.15	551.6	0.53	0.53			
38	29.37	558.7	0.79	0.80			
39	32.59	562.5	0.86	0.88			
40	35.81	569.7	1.05	1.07			
41	39.03	572.6	1.12	1.15			
42	42.25	574.9	1.12	1.14			

Experimental Data for Run 25

Heat Transfer Rate
q_o = 41.532
Btu/ft²-sec

Pressure
p_o = 10.580
psia

gauge	Θ deg	T_w °R	q_{hw}/q_o	q/q_o	gauge	Θ deg	p/p_o
53	-86.36	585.8	1.15	1.18			
55	-80.25	617.4	2.04	2.12			
56	-77.20	637.4	2.39	2.51			
57	-74.14	656.4	2.96	3.13			
58	-71.08	673.8	3.39	3.61			
59	-68.03	694.9	4.08	4.40			
61	-61.92	755.7	5.15	5.71			
62	-58.86	784.8	6.21	6.98			
1	-58.86	775.5	6.29	7.05			
3	-57.26	781.5	6.26	7.02			
4	-56.46	824.1	7.50	8.60			
5	-55.66	809.1	6.94	7.90			
6	-54.87	817.6	7.36	8.42			
7	-54.08	794.2	6.26	7.07			
9	-52.47	804.6	7.04	7.99			
10	-51.67	788.3	6.43	7.24			
69	-50.26	798.4	6.46	7.31			
68	-49.30	801.8	6.42	7.28			
67	-48.35	824.6	7.18	8.23			
66	-47.39	776.6	5.70	6.38			
65	-46.44	772.1	5.75	6.42			
64	-45.48	767.5	5.53	6.17			
24	-40.71	740.5	4.13	4.54			
25	-37.65	700.5	3.36	3.63			
28	-28.48	631.2	1.94	2.03			
29	-25.43	629.8	1.91	1.99			
31	-19.32	621.5	1.60	1.67			
34	-16.26	619.1	1.47	1.52			
36	-9.66	615.4	1.43	1.48			
37	-6.44	618.6	1.45	1.51			
38	-3.22	613.4	1.39	1.44			
39	0.00	615.3	1.43	1.48			
40	3.22	600.6	1.14	1.18			
41	6.44	612.1	1.54	1.59			
42	9.66	610.9	1.37	1.42			

Experimental Data for Run 26

Heat Transfer Rate $q_o = 42.653$ Btu/ft²-sec					Pressure $p_o = 10.556$ psia		
gauge	Θ deg	T_w °R	q_{hw}/q_o	q/q_o	gauge	Θ deg	p/p_o
53	-86.36	582.1	1.13	1.15	5	-99.43	0.24
54	-83.31	597.1	1.49	1.53	10	-63.63	1.98
55	-80.25	609.0	1.89	1.95	12	-54.08	3.10
56	-77.20	628.1	2.43	2.53	17	-51.69	3.03
57	-74.14	647.6	2.96	3.11	13	-49.30	2.42
58	-71.08	664.7	3.48	3.68	18	-46.91	2.16
59	-68.03	676.0	3.73	3.97	14	-44.53	2.08
61	-61.92	722.4	4.81	5.23	19	-42.14	1.68
62	-58.86	761.3	6.40	7.09	20	-37.36	1.40
1	-58.86	742.5	5.85	6.43	22	-25.43	0.96
2	-58.06	741.8	5.73	6.29	23	-18.27	0.94
3	-57.26	750.9	5.71	6.29	24	-11.10	0.95
4	-56.46	766.7	6.65	7.39	25	-3.94	0.97
5	-55.66	780.9	7.26	8.12	26	3.22	0.89
6	-54.87	778.2	6.80	7.60	28	17.54	0.76
7	-54.08	766.8	6.45	7.17			
9	-52.47	778.2	6.96	7.78			
10	-51.67	776.8	6.82	7.61			
69	-50.26	778.9	6.90	7.70			
68	-49.30	784.9	7.13	7.99			
67	-48.35	785.4	6.97	7.81			
66	-47.39	772.2	6.41	7.14			
65	-46.44	772.9	6.94	7.73			
64	-45.48	769.7	6.77	7.54			
24	-40.71	728.4	5.35	5.84			
25	-37.65	710.7	4.41	4.77			
28	-28.48	620.9	2.05	2.13			
29	-25.43	615.8	1.91	1.98			
31	-19.32	605.9	1.67	1.73			
34	-16.26	602.7	1.59	1.64			
36	-9.66	596.5	1.38	1.42			
37	-6.44	595.5	1.33	1.37			
38	-3.22	589.6	1.26	1.29			
39	0.00	588.2	1.19	1.22			
40	3.22	584.9	1.09	1.11			
41	6.44	588.6	1.14	1.16			
42	9.66	587.1	1.12	1.15			

Experimental Data for Run 31

Heat Transfer Rate $q_o = 42.747$ Btu/ft2-sec					Pressure $p_o = 10.636$ psia		
gauge	Θ deg	T_w °R	q_{hw}/q_o	q/q_o	gauge	Θ deg	p/p_o
53	-39.45	566.7	0.85	0.86	1	-81.17	0.11
54	-36.39	571.3	0.96	0.97	5	-52.52	0.40
55	-33.34	572.2	0.97	0.99	9	-23.87	0.82
56	-30.28	574.1	1.01	1.03	10	-16.71	0.85
57	-27.23	577.6	1.11	1.13	12	-7.16	0.91
58	-24.17	579.9	1.15	1.18	17	-4.77	0.91
59	-21.12	579.3	1.14	1.16	13	-2.39	0.93
61	-15.00	589.4	1.38	1.42	18	0.00	0.94
62	-11.95	587.9	1.38	1.41	14	2.39	0.90
1	-11.95	584.0	1.28	1.31	19	4.77	0.96
2	-11.15	586.8	1.37	1.40	15	7.16	0.94
3	-10.35	584.1	1.32	1.35	20	9.55	0.94
5	-8.75	586.3	1.36	1.39	22	21.49	0.84
9	-5.56	586.0	1.36	1.39	23	28.65	0.73
10	-4.76	587.0	1.39	1.42	24	35.81	0.63
68	-2.39	592.3	1.53	1.57	25	42.97	0.55
67	-1.43	591.6	1.45	1.49	26	50.13	0.42
66	-0.48	587.3	1.38	1.42	28	64.46	0.23
65	0.48	588.6	1.43	1.46			
64	1.43	587.8	1.43	1.46			
24	6.21	587.5	1.40	1.43			
29	21.49	582.8	1.26	1.28			
31	27.60	577.4	1.12	1.14			
34	30.65	575.2	1.06	1.08			
36	37.26	570.8	0.94	0.95			
37	40.47	570.2	0.99	1.00			
38	43.69	564.7	0.79	0.80			
39	46.91	562.5	0.72	0.73			
40	50.13	562.1	0.71	0.72			
41	53.35	557.9	0.61	0.61			
42	56.57	556.6	0.57	0.57			

Experimental Data for Run 59

Heat Transfer Rate
$q_o = 40.837$ Btu/ft^2-sec

gauge	Θ deg	T_w °R	q_{hw}/q_o	q/q_o
53	-53.77	644.6	2.87	3.02
54	-50.72	656.7	3.15	3.33
55	-47.66	673.8	3.61	3.85
56	-44.61	672.4	3.56	3.78
57	-41.55	688.3	3.95	4.24
58	-38.50	691.7	4.34	4.66
59	-35.44	713.9	5.06	5.49
61	-29.33	729.2	5.32	5.81
62	-26.27	793.8	8.33	9.40
1	-26.27	787.3	7.86	8.84
2	-25.47	802.5	8.55	9.68
3	-24.67	841.3	10.58	12.22
4	-23.87	866.7	11.86	13.88
5	-23.07	920.8	15.24	18.34
6	-22.28	921.7	14.76	17.77
7	-21.49	897.5	12.58	14.95
9	-19.88	950.5	18.01	22.02
71	-19.58	970.6	18.05	22.30
10	-19.08	982.7	18.61	23.15
70	-18.62	953.0	15.50	18.98
69	-17.67	939.8	13.50	16.41
68	-16.71	922.5	11.36	13.68
67	-15.76	910.7	9.79	11.72
66	-14.80	879.5	7.55	8.90
64	-12.89	836.8	4.96	5.71
24	-8.12	710.5	1.95	2.11
25	-5.06	645.5	1.22	1.28
28	4.11	560.3	0.30	0.30
29	7.16	557.1	0.20	0.20
31	13.27	553.1	0.20	0.20
32	16.33	556.6	0.40	0.41

Pressure
$p_o = 10.004$ psia

gauge	Θ deg	p/p_o
1	-95.49	0.43
3	-81.17	0.96
5	-66.85	1.61
7	-52.52	2.17
9	-38.20	2.58
10	-31.04	2.53
11	-26.26	3.19
16	-23.87	6.01
12	-21.49	8.75
17	-19.10	10.58
13	-16.71	4.98
18	-14.32	3.12
14	-11.94	1.78
19	-9.55	1.33
15	-7.16	0.71
20	-4.77	0.53
21	0.00	0.23
22	7.16	0.09
23	14.32	0.13
24	21.49	0.24
25	28.65	0.44
26	35.81	0.49
28	50.13	0.30

Experimental Data for Run 60

Heat Transfer Rate $q_o = 39.986$ Btu/ft²-sec					Pressure $p_o = 9.902$ psia		
gauge	Θ deg	T_w °R	q_{hw}/q_o	q/q_o	gauge	Θ deg	p/p_o
53	-53.77	638.2	2.42	2.54	1	-95.49	0.44
54	-50.72	650.1	2.90	3.06	3	-81.17	0.90
55	-47.66	660.1	3.19	3.38	5	-66.85	1.58
56	-44.61	668.4	3.44	3.67	7	-52.52	2.19
57	-41.55	672.9	3.78	4.03	10	-31.04	2.51
59	-35.44	702.3	4.03	4.36	11	-26.26	3.00
61	-29.33	724.2	5.22	5.71	16	-23.87	4.17
62	-26.27	779.4	6.91	7.76	12	-21.49	7.46
1	-26.27	746.5	6.29	6.96	17	-19.10	8.44
2	-25.47	752.2	6.88	7.62	13	-16.71	4.58
3	-24.67	774.6	7.78	8.72	18	-14.32	4.90
4	-23.87	799.0	8.88	10.07	14	-11.94	4.80
5	-23.07	836.7	10.78	12.47	19	-9.55	3.58
6	-22.28	831.9	11.39	13.14	15	-7.16	2.04
7	-21.49	840.3	11.96	13.85	20	-4.77	1.31
9	-19.88	880.7	14.36	16.99	21	0.00	0.53
71	-19.58	922.7	16.32	19.73	22	7.16	0.16
10	-19.08	934.5	17.52	21.32	23	14.32	0.07
70	-18.62	929.9	15.26	18.53	24	21.49	0.06
69	-17.67	950.4	14.84	18.22	25	28.65	0.14
68	-16.71	967.6	14.24	17.65	28	50.13	0.18
67	-15.76	946.6	12.55	15.38			
66	-14.80	964.4	11.31	13.99			
64	-12.89	963.6	10.27	12.69			
24	-8.12	838.9	6.06	7.02			
25	-5.06	733.7	3.15	3.46			
28	4.11	580.1	0.72	0.74			
29	7.16	566.8	0.49	0.50			
31	13.27	552.1	0.27	0.27			
32	16.33	547.8	0.18	0.18			

Experimental Data for Run 61

Heat Transfer Rate $q_o = 39.825$ Btu/ft²-sec					Pressure $p_o = 9.901$ psia		
gauge	Θ deg	T_w °R	q_{hw}/q_o	q/q_o	gauge	Θ deg	p/p_o
53	-68.10	592.5	1.23	1.26	1	-109.82	0.08
54	-65.04	590.9	1.07	1.10	3	-95.49	0.21
55	-61.99	613.0	1.35	1.40	5	-81.17	0.51
56	-58.93	628.1	1.81	1.89	7	-66.85	0.84
57	-55.87	653.3	1.90	2.00	9	-52.52	2.22
59	-49.76	748.4	5.54	6.13	10	-45.36	3.26
61	-43.65	867.9	11.22	13.18	11	-40.58	5.84
62	-40.60	883.2	15.38	18.21	16	-38.20	6.57
1	-40.60	885.7	15.55	18.43	12	-35.81	5.50
2	-39.79	867.1	15.34	18.01	17	-33.42	3.71
3	-39.00	861.0	14.80	17.32	13	-31.04	2.16
4	-38.20	842.5	14.33	16.61	18	-28.65	1.58
5	-37.40	837.8	12.54	14.50	14	-26.26	1.45
6	-36.60	783.5	9.77	10.99	19	-23.87	1.19
7	-35.81	780.8	9.01	10.12	15	-21.49	0.85
9	-34.21	749.4	7.79	8.61	20	-19.10	0.79
71	-33.90	737.4	7.01	7.71	21	-14.32	0.79
10	-33.40	750.5	7.30	8.07	22	-7.16	0.79
70	-32.95	725.9	6.65	7.27	23	0.00	0.82
69	-31.99	715.4	6.29	6.84	24	7.16	0.80
68	-31.04	702.0	5.52	5.97	25	14.32	0.84
67	-30.08	681.6	5.34	5.72	26	21.49	0.67
66	-29.13	684.7	4.66	4.99	28	35.81	0.48
64	-27.22	671.5	4.61	4.90			
24	-22.44	632.0	3.12	3.26			
25	-19.39	621.1	2.45	2.55			
28	-10.22	607.9	1.85	1.92			
29	-7.16	626.8	2.95	3.08			
31	-1.05	607.3	2.43	2.51			
32	2.01	602.7	2.11	2.17			

Experimental Data for Run 66

	Heat Transfer Rate $q_o = 30.216$ Btu/ft²-sec				Pressure $p_o = 4.968$ psia		
gauge	Θ deg	T_w °R	q_{hw}/q_o	q/q_o	gauge	Θ deg	p/p_o
53	-53.77	585.4	1.43	1.45	1	-95.49	0.30
54	-50.72	593.5	1.72	1.76	3	-81.17	0.75
55	-47.66	601.1	1.74	1.78	5	-66.85	1.56
56	-44.61	600.8	1.84	1.88	7	-52.52	2.22
57	-41.55	600.5	2.14	2.20	9	-38.20	2.67
58	-38.50	598.9	1.92	1.97	10	-31.04	2.60
59	-35.44	602.2	1.92	1.97	11	-26.26	2.81
61	-29.33	605.8	2.13	2.19	13	-16.71	2.85
62	-26.27	597.8	1.74	1.78	18	-14.32	2.87
1	-26.27	587.4	1.55	1.58	14	-11.94	3.23
2	-25.47	591.1	1.77	1.81	19	-9.55	3.43
3	-24.67	595.2	1.74	1.78	15	-7.16	3.19
4	-23.87	583.2	1.07	1.09	20	-4.77	3.35
5	-23.07	598.8	1.73	1.78	21	0.00	3.26
6	-22.28	587.4	1.27	1.30	22	7.16	2.45
7	-21.49	593.4	1.83	1.87	23	14.32	1.63
9	-19.88	589.5	1.36	1.38	24	21.49	0.96
71	-19.58	597.6	1.64	1.68	25	28.65	0.54
10	-19.08	587.3	1.28	1.30	26	35.81	0.34
70	-18.62	594.1	1.73	1.77	28	50.13	0.06
69	-17.67	593.4	1.47	1.50			
68	-16.71	579.4	1.03	1.05			
67	-15.76	596.7	1.74	1.79			
66	-14.80	595.4	1.68	1.72			
64	-12.89	605.6	2.08	2.14			
25	-5.06	609.0	2.55	2.62			
28	4.11	601.3	2.00	2.05			
29	7.16	600.7	1.92	1.97			
31	13.27	595.3	1.77	1.81			
32	16.33	590.6	1.59	1.62			

Experimental Data for Run 67

Heat Transfer Rate
$q_o = 41.492$ Btu/ft2-sec

gauge	Θ deg	T_w °R	q_{hw}/q_o	q/q_o
53	-53.77	613.9	2.15	2.23
54	-50.72	624.7	2.37	2.47
55	-47.66	629.8	2.56	2.67
56	-44.61	631.8	2.62	2.73
57	-41.55	633.7	2.66	2.78
58	-38.50	630.0	2.58	2.69
59	-35.44	635.0	2.65	2.78
61	-29.33	625.8	2.40	2.50
62	-26.27	631.7	2.63	2.75
1	-26.27	609.5	1.94	2.01
2	-25.47	608.7	1.91	1.97
3	-24.67	614.1	2.10	2.18
4	-23.87	614.5	2.24	2.33
5	-23.07	624.0	2.61	2.72
6	-22.28	615.2	2.16	2.24
7	-21.49	617.1	2.31	2.40
71	-19.58	618.2	2.40	2.49
10	-19.08	627.0	2.59	2.70
70	-18.62	617.0	2.22	2.30
69	-17.67	621.5	2.46	2.56
68	-16.71	619.2	2.39	2.49
67	-15.76	624.9	2.51	2.61
66	-14.80	622.7	2.40	2.50
64	-12.89	630.2	2.67	2.78
24	-8.12	629.6	2.87	2.99
25	-5.06	640.9	3.21	3.37
28	4.11	628.6	2.75	2.87
29	7.16	625.3	2.60	2.70
31	13.27	610.9	2.10	2.17
32	16.33	607.5	2.00	2.07

Pressure
$p_o = 9.934$ psia

gauge	Θ deg	p/p_o
1	-95.49	0.23
3	-81.17	0.64
5	-66.85	1.40
7	-52.52	1.99
9	-38.20	2.43
10	-31.04	2.45
11	-26.26	2.66
13	-16.71	2.80
18	-14.32	2.76
14	-11.94	3.04
19	-9.55	3.19
15	-7.16	3.04
20	-4.77	3.17
21	0.00	3.09
22	7.16	2.33
23	14.32	1.64
24	21.49	1.00
25	28.65	0.56
26	35.81	0.11
28	50.13	0.08
30	64.46	0.02

Experimental Data for Run 68

	Heat Transfer Rate $q_o = 37.503$ Btu/ft²-sec					Pressure $p_o = 9.130$ psia	
gauge	Θ deg	T_w °R	q_{hw}/q_o	q/q_o	gauge	Θ deg	p/p_o
53	-75.26	569.9	1.32	1.34	1	-116.98	0.12
54	-72.20	571.2	1.15	1.17	3	-102.65	0.34
55	-69.15	579.4	1.52	1.56	5	-88.33	0.77
56	-66.09	580.5	1.53	1.56	7	-74.01	0.89
57	-63.04	582.0	1.46	1.50	9	-59.68	1.35
58	-59.98	589.3	1.86	1.91	10	-52.52	1.44
59	-56.93	597.0	2.00	2.06	11	-47.75	1.59
61	-50.81	606.5	2.39	2.47	16	-45.36	1.68
62	-47.76	621.1	3.17	3.30	12	-42.97	1.66
1	-47.76	600.0	2.44	2.52	17	-40.58	1.82
2	-46.96	599.4	2.15	2.21	13	-38.20	1.85
3	-46.16	598.5	2.19	2.26	18	-35.81	2.13
4	-45.36	594.8	1.79	1.85	14	-33.42	2.44
5	-44.56	618.3	2.89	3.00	19	-31.04	2.81
6	-43.76	605.7	2.13	2.21	15	-28.65	2.62
7	-42.97	609.3	2.56	2.65	20	-26.26	2.91
71	-41.06	609.3	2.47	2.56	24	0.00	1.48
10	-40.57	620.3	2.74	2.86	25	7.16	0.55
70	-40.11	605.0	1.88	1.94	26	14.32	0.08
69	-39.15	608.6	2.35	2.44	28	28.65	0.06
68	-38.20	608.3	2.34	2.42	30	42.97	0.08
66	-36.29	619.8	2.75	2.87			
64	-34.38	623.8	2.90	3.03			
24	-29.60	630.8	3.43	3.59			
25	-26.55	647.6	3.93	4.15			
28	-17.38	671.1	5.33	5.69			
29	-14.32	692.5	6.84	7.38			
31	-8.21	768.4	10.34	11.60			
32	-5.16	759.1	8.80	9.82			

Experimental Data for Run 69

Heat Transfer Rate $q_o = 40.636$ Btu/ft²-sec					Pressure $p_o = 9.841$ psia		
gauge	Θ deg	T_w °R	q_{hw}/q_o	q/q_o	gauge	Θ deg	p/p_o
53	-53.77	622.7	2.87	2.98	1	-95.49	0.27
54	-50.72	642.2	3.62	3.80	3	-81.17	0.56
55	-47.66	646.7	3.91	4.11	5	-66.85	1.11
56	-44.61	654.2	4.44	4.69	7	-52.52	1.67
57	-41.55	654.4	4.37	4.61	10	-31.04	3.90
58	-38.50	654.3	3.86	4.08	11	-26.26	7.42
59	-35.44	694.0	4.81	5.17	16	-23.87	2.62
61	-29.33	813.6	11.13	12.68	12	-21.49	3.34
62	-26.27	823.7	15.20	17.40	17	-19.10	1.09
1	-26.27	756.9	10.93	12.11	13	-16.71	0.76
2	-25.47	724.6	9.06	9.88	18	-14.32	0.39
3	-24.67	714.1	8.31	9.02	14	-11.94	0.45
4	-23.87	687.6	7.28	7.81	19	-9.55	0.36
5	-23.07	671.9	6.00	6.38	15	-7.16	0.31
6	-22.28	643.8	4.92	5.17	20	-4.77	0.43
7	-21.49	637.0	4.34	4.54	21	0.00	0.66
9	-19.88	615.8	3.22	3.34	22	7.16	0.81
71	-19.58	609.4	2.97	3.07	23	14.32	0.65
10	-19.08	613.7	3.08	3.19	24	21.49	0.55
70	-18.62	601.0	2.44	2.52	25	28.65	0.49
69	-17.67	594.9	2.20	2.26	26	35.81	0.32
68	-16.71	587.0	1.83	1.87	28	50.13	0.24
67	-15.76	589.0	1.84	1.89	30	64.46	0.14
66	-14.80	576.7	1.32	1.34			
64	-12.89	583.1	1.48	1.51			
24	-8.12	564.7	0.62	0.63			
25	-5.06	573.1	0.66	0.67			
28	4.11	600.0	2.28	2.35			
29	7.16	603.1	2.53	2.61			
31	13.27	597.1	2.31	2.38			
32	16.33	593.1	2.12	2.17			

Experimental Data for Run 70

Heat Transfer Rate
$q_o = 40.169$ Btu/ft²-sec

gauge	Θ deg	T_w °R	q_{hw}/q_o	q/q_o
53	-75.26	601.1	1.85	1.91
54	-72.20	607.7	2.04	2.11
55	-69.15	617.9	2.58	2.68
56	-66.09	625.6	2.57	2.68
57	-63.04	629.1	2.86	2.98
58	-59.98	626.6	2.98	3.10
59	-56.93	625.5	3.06	3.19
61	-50.81	608.1	2.16	2.23
62	-47.76	593.9	1.73	1.77
1	-47.76	578.5	1.24	1.27
2	-46.96	576.3	1.19	1.21
3	-46.16	578.2	1.33	1.35
4	-45.36	574.4	1.10	1.11
5	-44.56	579.9	1.47	1.50
6	-43.76	575.7	0.99	1.01
7	-42.97	571.4	1.04	1.05
9	-41.37	569.8	0.86	0.87
71	-41.06	574.5	0.96	0.97
10	-40.57	572.5	1.09	1.11
70	-40.11	572.2	0.88	0.90
69	-39.15	572.8	0.97	0.99
68	-38.20	571.8	1.03	1.05
67	-37.24	571.1	0.85	0.87
66	-36.29	575.1	1.06	1.08
64	-34.38	574.3	1.00	1.02
24	-29.60	565.0	0.65	0.66
25	-26.55	574.5	1.01	1.03
28	-17.38	569.0	0.81	0.82
29	-14.32	572.1	0.96	0.98
31	-8.21	571.1	0.92	0.94
32	-5.16	570.4	0.89	0.90

Pressure
$p_o = 9.636$ psia

gauge	Θ deg	p/p_o
1	-116.98	0.07
3	-102.65	0.19
5	-88.33	0.51
7	-74.01	1.01
9	-59.68	1.28
10	-52.52	1.07
11	-47.75	0.99
16	-45.36	1.06
12	-42.97	1.09
17	-40.58	1.31
13	-38.20	0.98
18	-35.81	0.86
19	-31.04	1.12
15	-28.65	1.08
20	-26.26	1.03
21	-21.49	1.16
22	-14.32	1.01
23	-7.16	0.99
24	0.00	0.98
25	7.16	0.93
26	14.32	0.86
28	28.65	0.65
30	42.97	0.19

Experimental Data for Run 71

Heat Transfer Rate
$q_o = 37.812$ Btu/ft^2-sec

Pressure
$p_o = 8.834$ psia

gauge	Θ deg	T_w °R	q_{hw}/q_o	q/q_o	gauge	Θ deg	p/p_o
53	-75.26	574.3	0.89	0.90	1	-116.98	0.04
54	-72.20	585.0	1.10	1.12	3	-102.65	0.11
55	-69.15	597.8	1.20	1.24	5	-88.33	0.29
56	-66.09	610.7	1.43	1.47	7	-74.01	0.58
57	-63.04	630.6	2.04	2.13	9	-59.68	1.48
58	-59.98	652.3	2.88	3.04	10	-52.52	3.01
59	-56.93	692.5	4.24	4.55	11	-47.75	4.64
61	-50.81	743.3	6.16	6.78	16	-45.36	6.05
62	-47.76	774.2	9.52	10.64	12	-42.97	6.41
1	-47.76	772.1	9.77	10.91	17	-40.58	4.92
2	-46.96	774.8	10.49	11.73	13	-38.20	3.62
3	-46.16	781.2	11.23	12.59	18	-35.81	2.35
4	-45.36	780.9	11.30	12.67	14	-33.42	2.03
5	-44.56	788.5	12.24	13.77	19	-31.04	1.50
6	-43.76	769.9	11.41	12.72	15	-28.65	1.22
7	-42.97	763.9	11.06	12.29	20	-26.26	1.01
9	-41.37	741.3	9.72	10.69	21	-21.49	0.89
71	-41.06	743.4	10.19	11.22	22	-14.32	0.88
10	-40.57	750.3	10.39	11.47	23	-7.16	0.85
70	-40.11	733.4	9.53	10.44	24	0.00	0.88
69	-39.15	722.9	8.76	9.54	25	7.16	0.92
68	-38.20	714.2	8.20	8.89	26	14.32	0.76
67	-37.24	713.2	8.11	8.79	28	28.65	0.84
66	-36.29	703.2	7.37	7.95	30	42.97	0.45
64	-34.38	687.0	6.43	6.89			
24	-29.60	638.5	4.13	4.32			
25	-26.55	626.1	3.24	3.37			
28	-17.38	598.7	1.91	1.96			
29	-14.32	598.4	1.94	1.99			
31	-8.21	593.2	1.71	1.75			
32	-5.16	594.6	1.79	1.84			

Experimental Data for Run 72

Heat Transfer Rate $q_o = 47.949$ Btu/ft²-sec					Pressure $p_o = 12.749$ psia		
gauge	Θ deg	T_w °R	q_{hw}/q_o	q/q_o	gauge	Θ deg	p/p_o
53	-75.26	594.8	1.21	1.24	1	-116.98	0.03
54	-72.20	612.4	1.51	1.57	3	-102.65	0.09
55	-69.15	634.7	2.05	2.14	5	-88.33	0.24
56	-66.09	651.5	2.37	2.49	7	-74.01	0.54
57	-63.04	676.5	3.09	3.29	9	-59.68	1.86
58	-59.98	699.4	3.96	4.26	10	-52.52	3.18
59	-56.93	747.8	5.98	6.57	11	-47.75	4.58
61	-50.81	802.9	9.19	10.37	16	-45.36	5.01
62	-47.76	808.8	10.31	11.66	12	-42.97	4.77
1	-47.76	804.5	9.26	10.45	17	-40.58	4.93
2	-46.96	802.9	9.63	10.87	13	-38.20	2.40
3	-46.16	800.9	9.40	10.59	18	-35.81	1.94
4	-45.36	795.8	8.58	9.65	14	-33.42	1.62
5	-44.56	810.5	9.32	10.55	19	-31.04	1.38
6	-43.76	781.8	8.17	9.13	15	-28.65	1.16
7	-42.97	773.2	7.61	8.47	20	-26.26	1.02
9	-41.37	748.8	7.21	7.93	21	-21.49	0.97
71	-41.06	752.3	7.02	7.73	22	-14.32	0.85
10	-40.57	750.7	6.74	7.41	23	-7.16	0.88
70	-40.11	743.4	6.81	7.47	24	0.00	0.87
69	-39.15	735.9	6.58	7.20	25	7.16	0.91
68	-38.20	731.4	6.30	6.87	26	14.32	0.70
67	-37.24	719.0	5.63	6.10	28	28.65	1.07
66	-36.29	709.3	5.52	5.96	30	42.97	0.42
64	-34.38	694.4	5.03	5.39			
24	-29.60	651.1	3.42	3.60			
25	-26.55	636.2	2.87	3.00			
28	-17.38	614.7	2.15	2.22			
29	-14.32	610.7	2.08	2.14			
31	-8.21	606.9	1.90	1.96			
32	-5.16	606.1	1.96	2.02			

Experimental Data for Run 73

Heat Transfer Rate $q_o = 27.539$ Btu/ft²-sec					Pressure $p_o = 4.662$ psia		
gauge	Θ deg	T_w °R	q_{hw}/q_o	q/q_o	gauge	Θ deg	p/p_o
53	-75.26	564.6	1.00	1.01	1	-116.98	0.03
54	-72.20	572.3	1.41	1.44	3	-102.65	0.11
55	-69.15	583.7	1.97	2.01	5	-88.33	0.29
56	-66.09	593.8	2.50	2.56	7	-74.01	0.74
57	-63.04	607.9	3.12	3.22	9	-59.68	2.48
58	-59.98	616.0	3.79	3.93	10	-52.52	3.51
59	-56.93	640.1	5.06	5.30	11	-47.75	3.94
61	-50.81	669.2	6.96	7.40	16	-45.36	3.89
62	-47.76	674.9	7.36	7.85	12	-42.97	3.98
1	-47.76	670.3	6.61	7.03	13	-38.20	2.22
2	-46.96	662.3	6.23	6.60	18	-35.81	1.69
3	-46.16	663.6	6.01	6.38	14	-33.42	1.59
4	-45.36	660.1	5.63	5.96	19	-31.04	1.47
5	-44.56	667.2	6.05	6.42	15	-28.65	1.13
6	-43.76	659.6	5.77	6.11	20	-26.26	1.06
7	-42.97	654.9	5.35	5.65	21	-21.49	1.04
9	-41.37	644.6	4.83	5.08	22	-14.32	0.95
71	-41.06	649.8	5.15	5.42	23	-7.16	0.93
10	-40.57	648.5	5.04	5.31	24	0.00	0.91
70	-40.11	646.0	4.93	5.19	25	7.16	0.94
69	-39.15	642.4	4.84	5.08	26	14.32	0.74
68	-38.20	640.0	4.64	4.87	28	28.65	0.29
67	-37.24	635.7	4.31	4.51	30	42.97	0.45
66	-36.29	628.5	4.02	4.19			
64	-34.38	622.0	3.75	3.90			
24	-29.60	601.3	2.73	2.81			
25	-26.55	588.6	2.17	2.22			
28	-17.38	574.4	1.71	1.74			
31	-8.21	571.1	1.53	1.56			
32	-5.16	570.5	1.48	1.50			

Experimental Data for Run 74

Heat Transfer Rate q_o = 38.603 Btu/ft²-sec					Pressure p_o = 9.203 psia		
gauge	Θ deg	T_w °R	q_{hw}/q_e	q/q_o	gauge	Θ deg	p/p_o
54	-72.20	547.3	0.29	0.29	1	-116.98	0.01
55	-69.15	549.2	0.32	0.32	3	-102.65	0.03
56	-66.09	551.5	0.36	0.37	5	-88.33	0.07
57	-63.04	553.4	0.41	0.41	7	-74.01	0.16
58	-59.98	554.8	0.47	0.47	9	-59.68	0.31
59	-56.93	558.5	0.53	0.54	10	-52.52	0.36
61	-50.81	560.5	0.58	0.59	11	-47.75	0.44
62	-47.76	558.9	0.56	0.57	16	-45.36	0.58
1	-47.76	558.0	0.50	0.50	12	-42.97	0.61
2	-46.96	558.9	0.54	0.54	17	-40.58	0.66
3	-46.16	558.6	0.52	0.53	13	-38.20	0.57
4	-45.36	559.8	0.60	0.60	18	-35.81	0.63
5	-44.56	561.9	0.61	0.62	14	-33.42	0.68
6	-43.76	560.8	0.57	0.58	19	-31.04	0.82
7	-42.97	560.6	0.60	0.61	15	-28.65	0.77
9	-41.37	560.9	0.58	0.59	20	-26.26	0.87
71	-41.06	565.9	0.70	0.71	21	-21.49	0.95
10	-40.57	564.9	0.71	0.72	22	-14.32	0.92
70	-40.11	565.1	0.69	0.70	23	-7.16	0.96
69	-39.15	565.6	0.68	0.69	24	0.00	0.99
68	-38.20	566.3	0.72	0.73	25	7.16	1.09
67	-37.24	568.3	0.74	0.75	26	14.32	0.93
66	-36.29	568.6	0.76	0.77			
64	-34.38	570.0	0.78	0.79			
24	-29.60	569.4	0.80	0.81			
25	-26.55	572.6	0.83	0.84			
28	-17.38	573.7	0.91	0.92			
29	-14.32	576.4	0.94	0.96			
31	-8.21	577.6	0.97	0.99			
32	-5.16	579.0	0.96	0.98			

Experimental Data for Run 75

Heat Transfer Rate q_o = 35.897 Btu/ft²-sec					Pressure p_o = 7.816 psia		
gauge	Θ deg	T_w °R	q_{hw}/q_o	q/q_o	gauge	Θ deg	p/p_o
53	-53.77	647.3	3.65	3.84	1	-95.49	0.31
54	-50.72	662.8	4.06	4.30	3	-81.17	0.66
55	-47.66	671.8	4.39	4.68	5	-66.85	1.32
56	-44.61	683.3	5.06	5.42	7	-52.52	2.01
57	-41.55	690.8	5.38	5.79	9	-38.20	2.48
58	-38.50	694.8	5.50	5.92	11	-26.26	5.63
59	-35.44	722.1	6.39	6.98	16	-23.87	4.20
61	-29.33	813.9	11.06	12.65	12	-21.49	3.50
62	-26.27	838.6	13.51	15.65	17	-19.10	1.52
1	-26.27	790.2	10.89	12.30	13	-16.71	0.78
2	-25.47	775.7	9.50	10.65	18	-14.32	0.54
3	-24.67	767.1	8.63	9.63	14	-11.94	0.50
4	-23.87	757.2	8.32	9.24	19	-9.55	0.51
5	-23.07	742.4	6.86	7.56	15	-7.16	0.46
6	-22.28	719.4	5.62	6.13	20	-4.77	0.64
7	-21.49	708.8	5.20	5.63	21	0.00	0.82
10	-19.08	660.5	3.37	3.57	22	7.16	0.89
70	-18.62	642.2	2.66	2.79	23	14.32	0.71
69	-17.67	629.8	2.27	2.37	24	21.49	0.62
68	-16.71	617.9	1.99	2.07	25	28.65	0.58
67	-15.76	610.3	1.87	1.94	26	35.81	0.41
66	-14.80	599.2	1.54	1.59	28	50.13	0.26
64	-12.89	588.7	1.27	1.30	30	64.46	0.15
24	-8.12	566.5	0.76	0.77			
25	-5.06	576.8	0.87	0.89			
28	4.11	603.7	2.50	2.58			
29	7.16	606.4	2.55	2.63			
31	13.27	600.4	2.01	2.07			
32	16.33	595.0	1.73	1.77			

Experimental Data for Run 76

Heat Transfer Rate $q_o = 35.467$ Btu/ft²-sec					Pressure $p_o = 7.664$ psia		
gauge	Θ deg	T_w °R	q_{hw}/q_o	q/q_o	gauge	Θ deg	p/p_o
53	-53.77	625.4	2.63	2.74	1	-95.49	0.38
54	-50.72	634.7	3.01	3.15	3	-81.17	0.76
55	-47.66	642.8	3.29	3.46	5	-66.85	1.43
56	-44.61	649.7	3.44	3.63	7	-52.52	2.04
57	-41.55	656.3	3.85	4.07	9	-38.20	2.60
58	-38.50	658.2	3.82	4.04	10	-31.04	2.66
59	-35.44	666.1	4.12	4.38	11	-26.26	2.90
61	-29.33	672.8	4.33	4.62	13	-16.71	2.86
62	-26.27	658.9	3.90	4.13	18	-14.32	2.95
1	-26.27	647.5	3.47	3.66	14	-11.94	3.08
2	-25.47	646.4	3.48	3.67	19	-9.55	3.41
3	-24.67	651.4	3.73	3.94	15	-7.16	2.97
4	-23.87	651.2	3.66	3.87	20	-4.77	3.10
5	-23.07	666.7	4.08	4.34	21	0.00	2.67
6	-22.28	656.5	3.84	4.06	22	7.16	1.34
7	-21.49	661.4	3.99	4.24	23	14.32	0.64
71	-19.58	663.0	4.08	4.34	24	21.49	0.35
10	-19.08	665.7	4.20	4.46	25	28.65	0.21
70	-18.62	660.5	4.08	4.33	26	35.81	0.14
69	-17.67	662.5	3.96	4.21	28	50.13	0.07
68	-16.71	664.3	4.15	4.41	30	64.46	0.05
67	-15.76	670.0	4.28	4.56			
66	-14.80	665.4	4.09	4.35			
64	-12.89	672.2	4.42	4.72			
28	4.11	628.6	3.20	3.34			
29	7.16	619.1	2.69	2.80			
31	13.27	583.5	1.62	1.66			
32	16.33	561.7	0.58	0.59			

Experimental Data for Run 77

Heat Transfer Rate $q_o = 35.129$ Btu/ft²-sec					Pressure $p_o = 7.837$ psia		
gauge	θ deg	T_w °R	q_{hw}/q_o	q/q_o	gauge	θ deg	p/p_o
53	-53.77	628.4	3.72	3.90	1	-95.49	0.37
54	-50.72	619.5	3.32	3.47	3	-81.17	0.84
55	-47.66	604.8	2.90	3.00	5	-66.85	1.61
56	-44.61	604.6	2.72	2.81	7	-52.52	1.37
57	-41.55	588.5	2.31	2.37	9	-38.20	0.98
58	-38.50	583.6	1.90	1.95	10	-31.04	0.90
59	-35.44	584.5	1.74	1.78	11	-26.26	0.87
61	-29.33	573.1	1.59	1.62	16	-23.87	1.08
62	-26.27	558.7	0.90	0.91	12	-21.49	1.16
1	-26.27	556.3	0.87	0.88	17	-19.10	1.15
2	-25.47	557.2	0.98	0.99	13	-16.71	0.92
3	-24.67	557.4	0.96	0.97	18	-14.32	0.95
4	-23.87	557.8	0.79	0.80	14	-11.94	1.01
5	-23.07	566.1	1.09	1.11	19	-9.55	1.02
6	-22.28	559.8	0.92	0.94	15	-7.16	0.97
7	-21.49	560.6	0.89	0.90	20	-4.77	0.97
9	-19.88	563.2	1.04	1.06	21	0.00	1.06
71	-19.58	566.4	1.11	1.12	22	7.16	0.90
10	-19.08	564.7	1.15	1.16	23	14.32	0.81
70	-18.62	564.4	1.14	1.16	24	21.49	0.76
69	-17.67	565.5	1.06	1.07	25	28.65	0.72
68	-16.71	565.9	1.17	1.19	26	35.81	0.55
66	-14.80	567.2	1.09	1.11	28	50.13	0.34
64	-12.89	566.4	1.06	1.08	30	64.46	0.20
24	-8.12	563.2	1.08	1.10			
25	-5.06	567.2	1.05	1.07			
28	4.11	562.9	0.95	0.96			
29	7.16	562.6	1.00	1.02			
31	13.27	561.1	0.91	0.92			
32	16.33	559.8	0.85	0.86			

Experimental Data for Run 78

Heat Transfer Rate $q_o = 35.483$ Btu/ft²-sec					Pressure $p_o = 7.763$ psia		
gauge	Θ deg	T_w °R	q_{hw}/q_o	q/q_o	gauge	Θ deg	p/p_o
53	-53.77	684.9	3.18	3.41	1	-95.49	0.36
54	-50.72	706.7	3.78	4.11	3	-81.17	0.75
55	-47.66	716.7	3.88	4.23	5	-66.85	1.47
56	-44.61	726.0	4.29	4.70	7	-52.52	2.17
57	-41.55	741.9	4.93	5.45	9	-38.20	2.76
58	-38.50	744.1	4.90	5.43	10	-31.04	2.81
59	-35.44	759.2	5.25	5.86	11	-26.26	2.82
61	-29.33	767.3	5.35	6.00	16	-23.87	3.84
62	-26.27	785.3	6.50	7.35	12	-21.49	6.22
1	-26.27	751.7	5.62	6.24	17	-19.10	5.35
2	-25.47	754.7	5.74	6.38	13	-16.71	6.47
3	-24.67	763.2	5.94	6.63	18	-14.32	5.70
4	-23.87	772.7	6.27	7.04	14	-11.94	2.27
5	-23.07	791.8	6.85	7.76	19	-9.55	2.77
6	-22.28	778.4	6.69	7.54	15	-7.16	0.76
7	-21.49	792.8	7.54	8.55	20	-4.77	0.95
9	-19.88	816.1	8.88	10.19	21	0.00	0.33
71	-19.58	845.2	10.46	12.20	22	7.16	0.17
10	-19.08	841.6	10.18	11.85	23	14.32	0.23
70	-18.62	866.8	11.73	13.83	24	21.49	0.41
69	-17.67	879.9	12.20	14.49	25	28.65	0.57
68	-16.71	888.0	12.02	14.33	26	35.81	0.50
67	-15.76	902.6	12.17	14.64	28	50.13	0.21
66	-14.80	887.8	10.75	12.82	30	64.46	0.11
64	-12.89	858.2	7.06	8.28			
24	-8.12	800.5	4.16	4.74			
25	-5.06	742.1	2.09	2.31			
28	4.11	597.7	0.38	0.39			
29	7.16	575.9	0.27	0.27			
31	13.27	561.8	0.47	0.48			
32	16.33	564.9	0.80	0.81			

Experimental Data for Run 79

Heat Transfer Rate $q_o = 41.587$ Btu/ft²-sec					Pressure $p_o = 9.934$ psia		
gauge	Θ deg	T_w °R	q_{hw}/q_o	q/q_o	gauge	Θ deg	p/p_o
53	-53.77	654.8	3.65	3.85	1	-95.49	0.27
54	-50.72	674.3	4.60	4.91	3	-81.17	0.60
55	-47.66	690.1	5.32	5.71	5	-66.85	1.18
56	-44.61	701.7	5.68	6.14	7	-52.52	2.13
57	-41.55	717.1	5.55	6.04	9	-38.20	2.03
58	-38.50	713.7	5.45	5.93	16	-23.87	4.63
59	-35.44	729.3	6.08	6.66	12	-21.49	3.86
61	-29.33	838.9	14.82	17.13	17	-19.10	1.88
62	-26.27	903.7	16.62	19.87	13	-16.71	0.88
1	-26.27	849.2	10.00	11.62	18	-14.32	0.58
2	-25.47	832.0	8.41	9.69	14	-11.94	0.44
3	-24.67	824.1	7.14	8.19	19	-9.55	0.49
4	-23.87	797.0	5.48	6.21	15	-7.16	0.41
5	-23.07	797.4	5.38	6.09	20	-4.77	0.75
6	-22.28	765.2	4.19	4.67	21	0.00	1.10
7	-21.49	754.1	3.94	4.36	22	7.16	0.86
9	-19.88	700.6	2.87	3.10	23	14.32	0.70
71	-19.58	692.0	2.81	3.02	24	21.49	0.63
10	-19.08	693.3	2.87	3.09	25	28.65	0.63
70	-18.62	674.0	2.40	2.56	26	35.81	0.50
69	-17.67	654.3	2.15	2.27	28	50.13	0.29
68	-16.71	640.6	1.99	2.09	30	64.46	0.16
67	-15.76	630.3	1.80	1.88			
66	-14.80	615.5	1.58	1.64			
64	-12.89	601.3	1.26	1.30			
24	-8.12	578.2	1.08	1.11			
25	-5.06	587.0	1.76	1.81			
28	4.11	618.3	2.90	3.01			
29	7.16	622.2	2.67	2.78			
31	13.27	607.3	1.85	1.92			
32	16.33	601.8	1.85	1.91			

Experimental Data for Run 80

Heat Transfer Rate
$q_o = 22.400$
Btu/ft²-sec

Pressure
$p_o = 3.510$
psia

gauge	Θ deg	T_w °R	q_{hw}/q_o	q/q_o	gauge	Θ deg	p/p_o
53	-53.77	598.3	2.53	2.61	1	-95.49	0.29
54	-50.72	610.6	3.07	3.18	3	-81.17	0.51
55	-47.66	611.7	3.09	3.21	5	-66.85	0.73
56	-44.61	616.4	3.20	3.33	7	-52.52	1.85
57	-41.55	624.3	3.43	3.59	9	-38.20	2.50
58	-38.50	629.4	3.82	4.01	10	-31.04	2.47
59	-35.44	638.4	4.37	4.60	11	-26.26	3.85
61	-29.33	651.4	4.17	4.42	16	-23.87	7.87
62	-26.27	709.4	6.60	7.21	12	-21.49	8.77
1	-26.27	692.2	5.24	5.67	17	-19.10	6.77
2	-25.47	700.8	6.12	6.65	13	-16.71	3.61
3	-24.67	715.5	7.36	8.06	18	-14.32	1.62
4	-23.87	716.3	7.92	8.68	14	-11.94	1.01
5	-23.07	724.2	9.58	10.54	19	-9.55	0.52
6	-22.28	715.6	9.67	10.59	15	-7.16	0.38
7	-21.49	714.9	10.46	11.46	20	-4.77	0.38
9	-19.88	689.8	9.96	10.76	21	0.00	0.37
71	-19.58	686.5	10.33	11.15	22	7.16	0.52
10	-19.08	693.0	10.59	11.47	23	14.32	0.78
70	-18.62	671.5	9.21	9.86	24	21.49	0.77
69	-17.67	655.9	8.00	8.49	25	28.65	0.63
68	-16.71	643.3	7.00	7.45	26	35.81	0.45
67	-15.76	630.7	6.10	6.40	28	50.13	0.26
64	-12.89	593.5	3.28	3.38	30	64.46	0.16
24	-8.12	559.3	1.37	1.39			
25	-5.06	555.2	0.85	0.86			
28	4.11	557.2	0.57	0.58			
29	7.16	564.7	0.62	0.63			
31	13.27	578.9	1.74	1.78			
32	16.33	578.5	2.17	2.22			

Experimental Data for Run 81

Heat Transfer Rate q_o = 35.861 Btu/ft²-sec					Pressure p_o = 7.800 psia		
gauge	Θ deg	T_w °R	q_{hw}/q_o	q/q_o	gauge	Θ deg	p/p_o
53	-53.77	551.4	0.47	0.47	1	-95.49	0.05
54	-50.72	555.4	0.60	0.60	3	-81.17	0.09
55	-47.66	555.2	0.61	0.61	5	-66.85	0.22
56	-44.61	558.2	0.70	0.70	7	-52.52	0.37
57	-41.55	562.7	0.86	0.87	9	-38.20	0.58
58	-38.50	568.6	1.02	1.03	10	-31.04	0.61
62	-26.27	572.4	1.17	1.19	11	-26.26	0.72
1	-26.27	564.4	0.97	0.98	16	-23.87	0.91
2	-25.47	565.4	1.02	1.03	12	-21.49	0.98
3	-24.67	565.4	1.01	1.03	17	-19.10	0.95
4	-23.87	566.1	1.04	1.05	13	-16.71	0.80
5	-23.07	566.0	0.99	1.00	18	-14.32	0.85
6	-22.28	566.0	0.99	1.00	14	-11.94	0.88
7	-21.49	565.9	0.97	0.98	19	-9.55	1.02
9	-19.88	566.5	0.97	0.98	15	-7.16	0.95
71	-19.58	576.0	1.38	1.40	20	-4.77	1.02
10	-19.08	569.5	1.11	1.13	21	0.00	1.07
70	-18.62	574.7	1.29	1.31	22	7.16	0.94
69	-17.67	573.3	1.24	1.26	23	14.32	0.92
68	-16.71	572.6	1.20	1.22	24	21.49	0.87
67	-15.76	572.9	1.18	1.20	25	28.65	0.85
66	-14.80	573.8	1.23	1.25	26	35.81	0.65
64	-12.89	575.4	1.25	1.27	28	50.13	0.42
24	-8.12	572.8	1.12	1.14	30	64.46	0.26
28	4.11	572.4	1.07	1.08			
29	7.16	571.5	1.09	1.11			
31	13.27	572.3	1.18	1.20			
32	16.33	572.7	1.22	1.24			

Experimental Data for Run 98

Heat Transfer Rate
$q_o = 34.551$ Btu/ft²-sec

gauge	θ deg	T_w °R	q_{hw}/q_o	q/q_o
53	-53.77	626.9	3.48	3.64
54	-50.72	637.8	4.05	4.26
55	-47.66	650.2	4.93	5.21
56	-44.61	651.4	5.11	5.41
57	-41.55	678.2	4.99	5.36
58	-38.50	707.4	5.10	5.55
59	-35.44	711.2	4.70	5.13
61	-29.33	801.3	15.53	17.74
62	-26.27	702.3	9.36	10.17
1	-26.27	648.1	5.64	5.96
2	-25.47	628.8	4.67	4.89
3	-24.67	625.5	4.38	4.58
4	-23.87	616.3	3.66	3.82
5	-23.07	611.4	3.17	3.29
6	-22.28	595.1	2.57	2.65
7	-21.49	589.2	2.30	2.36
9	-19.88	578.4	1.87	1.92
71	-19.58	583.2	1.98	2.03
10	-19.08	579.4	1.81	1.85
70	-18.62	582.4	1.95	2.00
69	-17.67	578.1	1.70	1.74
68	-16.71	574.0	1.42	1.45
67	-15.76	574.8	1.40	1.42
64	-12.89	572.2	1.21	1.24
24	-8.12	570.0	1.00	1.02
25	-5.06	615.5	2.35	2.45
28	4.11	588.0	2.32	2.38
29	7.16	584.2	2.09	2.14
31	13.27	580.3	1.75	1.79

Pressure
$p_o = 7.552$ psia

gauge	θ deg	p/p_o
1	-95.49	0.29
5	-66.85	1.28
7	-52.52	2.05
9	-38.20	2.63
10	-31.04	7.00
11	-26.26	4.10
16	-23.87	2.04
12	-21.49	1.82
17	-19.10	1.00
13	-16.71	0.51
18	-14.32	0.49
14	-11.94	0.52
19	-9.55	0.72
15	-7.16	0.60
20	-4.77	0.94
21	0.00	1.00
22	7.16	0.81
23	14.32	0.67
24	21.49	0.63
25	28.65	0.58
26	35.81	0.48
30	64.46	0.16